TRANSITION-EDGE SENSOR MICROCALORIMETERS FOR A DIFFUSE SOFT X-RAY SOUNDING ROCKET MISSION

by

Kelsey M. Morgan

A dissertation submitted in partial fulfillment of the
requirements for the degree of

Doctor of Philosophy
(Physics)

at the
University of Wisconsin–Madison
2015

Date of final oral examination: 03/24/2015

The dissertation is approved by the following members of the Final Oral Committee:
Dan McCammon, Professor, Physics
Peter Timbie, Professor, Physics
Robert McDermott, Professor, Physics
Justin Vandenbroucke, Assistant Professor, Physics
Sebastian Heinz, Associate Professor, Astronomy

Abstract

The extent and composition of the soft Diffuse X-ray Background (DXRB) has been the subject of debate since its discovery in the 1960s. Initially assumed to be extragalactic, it was soon realized that most of the emission observed between 0.1-1 keV originated inside the Galaxy and was most likely thermal emission from hot gas. However, when a few high resolution spectral measurements became available in the 1990s and early 2000s it became apparent that standard thermal models were not a good fit to the observations. It has also become apparent that a significant fraction of the diffuse background, particularly in the $1/4$ keV energy range, may actually be produced by charge exchange within the Solar System.

An essential part of understanding the different contributions to the DXRB is obtaining more high spectral resolution data. The large number of closely-spaced emission lines in the $1/4$ keV energy range requires 1-2 eV FWHM energy resolution to resolve individual lines. This thesis details efforts to design a detector array capable of < 2 eV FWHM resolution at 250 eV using a superconducting transition-edge sensor thermometer coupled to a thin gold absorber. I show that 2 eV FWHM energy resolution is possible while still maintaining enough collecting area and efficiency to enable a sounding rocket observation with currently available readout and cryogenic technology. In thin, large area absorbers, position dependent pulse shape can degrade energy resolution. Simulations of thermal diffusion in thin gold layers indicate that broadening due to position dependent pulse shape is expected to be minimal in these devices. Results from test devices are presented, with energy resolution and broadening due to position dependent pulse shape showing good agreement with modeled behavior.

Acknowledgments

It's dangerous to go alone! Fortunately, I never had to. There are more people deserving of thanks than I can name here, so the first thank you goes to all of the colleagues, friends, and family who were a part of the long and winding 6 year road I took to get here.

I thank my advisor, Dan McCammon. Dan, you had me at "rockets," but looking back on it, I truly couldn't have asked for a better opportunity. I'm grateful for your support and guidance, your enthusiasm for your work, and your willingness to always share your extensive knowledge. You told me once years ago that you thought you and I could accomplish a lot together, and I hope I've held up my end of that. It would be an honor to work together in the future.

This project would never have gotten off the ground without the X-ray Calorimeter group at NASA's Goddard Space Flight Center. In particular, I would like to thank Caroline Kilbourne for her support, of both the project and me. And an especially big thank you goes to Megan Eckart for her efforts at every step of the process, from design to testing to analysis. I thank her for being a friend and colleague in the many hours we spent in the lab together. I learned a tremendous amount. I'd also like to thank Jay Chervenak, Ed Wassell, Jennette Matteo, and the Detector Design Lab at GSFC for making all of the devices used in this work. This project was also enabled by a NASA Space Technology Research Fellowship, which facilitated (and funded) my trips to Goddard.

I'd also like to extend a thank you to all of the Wisconsin staff, postdocs, graduate students, and undergraduates that I've gotten the opportunity to work with in our lab over the years. I'll miss you guys. Kari Kripps, I'm glad we got to work together and I wish I'd had time to absorb more of your cleanroom knowledge. And to Xavier Defay, Mitchell Hokin, Dallas Wulf, and Felix Jaeckel, thank you for hard work and companionship during long days, cross country drives, and countless hours applying and removing tape.

I'm lucky to have a terrific support network off-campus, too, without which I'd have never made it through grad school. To the Psych night crew: Rachael, Laura, Ben, Clare, Carrick, and Joe, thanks for the barbecues, movie nights, games, and emergency pie. And a "thank you" doesn't really seem adequate to express my gratitude to my parents for getting me here in the first place. To my dad, John, for always being my #1 fan, whether it was softball or science. And to my mom, Donna, for teaching me that you don't have to be a big man to be a superhero, or, in my considerably more humble case, an astrophysicist.

And finally, Brianne. It would require another thesis to detail the million ways that I depend on your support, friendship, and patience. Thank you. I love you.

Contents

List of Figures

List of Tables

Chapter 1

Introduction

1.1 Observations of the Diffuse X-ray Background

Studying the interstellar medium has shown our Galaxy to be a dynamic and sometimes violent place. X-ray observations have revealed that much of what appeared to be empty space isn't empty after all. Instead, it is filled with gas that has been shock heated to millions of degrees that glows only in soft X-rays. We now know that this Diffuse X-ray Background (DXRB) is critical to our understanding of the interstellar medium and its role in the evolution of galaxies. Our model of the DXRB has been continually evolving thanks to decades of surprise discoveries enabled by clever experiments and a steady drive to improve observational capabilities.

The story begins in 1962 with the launch of a sounding rocket carrying three Geiger counters sensitive to energies of 2-6 keV. The stated purpose of the mission was to observe fluorescent X-rays produced on the lunar surface by X-rays from the Sun, but it made two serendipitous discoveries that proved much more significant. One of these discoveries was the first "X-ray star," later identified as Scorpius X-1, an accreting neutron star in a binary system. The second discovery was a large isotropic flux coming from outside the Solar System (Giacconi et al., 1962). There is little interstellar absorption at these energies, so the isotropic nature of the diffuse flux implied an extragalactic source. It was posited early on that this emission may be produced in the centers of distant Galaxies (Gould & Burbidge, 1963). It would be another four decades before this was observationally verified by deep surveys with the Chandra X-ray satellite, which showed that at least 80% of the X-ray background in the 2-8 keV band must be emitted by distant active galaxies (e.g., Brandt et al. (2001), Cowie et al. (2002), Hickox & Markevitch (2006)).

The Giacconi discovery prompted a flurry of follow-up experiments, confirming the existence of the diffuse flux and showing good agreement with a power law spectrum all the way up to 100 MeV (see, for example, Metzger (1964), Rothenflug et al. (1965), Kraushaar et al. (1965)). In the mid 1960s, before instruments capable of measuring cosmic X-rays with energies below 1 keV were available, it was assumed that Galactic (and possibly intergalactic) absorption would cause the spectrum to fall off at energies below a couple keV, since the cross section for photoelectric absorption is proportional to E^{-3}. When measurements below 1 keV became available, starting with Bowyer et al. (1968), it became apparent that the observed intensity was much greater than what was expected from simple extrapolation of the high energy power law.

Of particular interest were observations at ¼ keV or below. Rocket experiments using proportional counters and atomic absorption edge filters showed that a significant source of emission must exist within the Galaxy. The excess flux (over the extrapolated power law) did not vary with neutral hydrogen column density (N_H) as would be expected for absorption (Bunner et al., 1971), and a search for absorption by the Small Magellanic Cloud showed that the majority of the flux could not be extragalactic in origin (McCammon et al., 1971). All-sky surveys were completed over the next decade. For energies < 284 eV the intensity was found to be anticorrelated with N_H down to angular scales of tens of degrees, limited by the angular resolution of the detectors (McCammon et al. (1983), Marshall & Clark (1984)).

The most likely explanation for the source of the 1/4 keV emission seemed to be diffuse thermal emission from hot gas at temperatures around 10^6 K. In fact, this was not a new idea: in the mid-50s Lyman Spitzer proposed a Galactic corona of 10^6 K as a means of explaining the latitude distribution of interstellar clouds (Spitzer, 1956). Spitzer also pointed out that radiative cooling is very slow at $T > 10^6$ K, and even after accounting for both free-free transitions and inelastic collisions the expected cooling time for coronal gas would be on the order of 10^9 years. However, despite the observed anticorrelation with N_H, modeling the emission as a distant absorbed source, such as a Galactic halo or corona, did not fit the observations. The residual flux in the Galactic plane was about 30% of the maximum intensity observed at high latitude, too high to be consistent with absorption. Additionally, although the calculated cross sections for the B-band (130-188 eV) and C-band (160-284 eV) differ by a factor of two (since $\sigma \propto E^{-3}$), the apparent cross sections assuming an absorption model were nearly identical (McCammon et al., 1983). These discrepancies, coupled with the discovery of a local (within 200 pc) deficiency in HI, led to the suggestion of a displacement model, where hot gas filled the void left in the HI, producing the spatial anticorrelation (Sanders et al. (1977), Tanaka & Bleeker (1977)). This structure was dubbed the Local Hot Bubble and modeled as an irregularly shaped cavity in the local HI about 100 pc in extent and filled with X-ray emitting gas at around 10^6 K.

The structure of the 3/4 keV emission is markedly different. The emission is dominated by a large, bright feature extending about 30° from the Galactic center, and bright arcs correlated with the Loop I radio feature. Several smaller structures revealed by all-sky surveys were proposed to be cavities in the ISM heated by supernova ejecta, much like the Local Hot Bubble. Aside from these bubble-like structures, the emission is largely featureless, showing very little variation between the plane and poles. The extragalactic power law could account for about half of the emission at high latitudes, but would drop to zero in the plane. Stellar contributions could make up for some of the deficit, but would not extend to high enough latitudes to fully compensate for the effects of absorption. A population of objects like the supernova bubbles could be distributed in such a way as to provide the remaining emission, but the detailed balance between these components required to make the result appear latitude-independent seemed contrived and unsatisfactory (McCammon et al., 1983). Spectra obtained by the X-ray Quantum Calorimeter (XQC), a microcalorimeter-based sounding rocket payload capable of ΔE = 5-12 eV FWHM in the soft X-ray, showed that 40-60% of the 3/4 keV flux originated within the Galaxy McCammon et al. (2002). XQC was also able to resolve many individual emission lines, supporting the hypothesis that the local emission was thermal, though it was unlikely to originate in the Local Bubble (Snowden et al., 1993). A hot halo of higher temperature gas (2-3 $\times$ 10^6 K) produced by supernova-blown bubbles provides a compelling explanation, but again better models and more data are needed to solve the problem.

The Local Hot Bubble model for the 1/4 keV background was refined throughout the 1980s, but the next major leap in understanding would be brought about by the X-ray observatory ROSAT, which operated from 1990 to 1999 and produced all-sky maps of the soft diffuse emission from 0.25 - 2 keV with approximately 1° spatial resolution, limited by statistics (see Figure 1.1). Pointed observations with higher statistics could be used to study the diffuse emission on angular scales as small as 12', which revealed shadowing of the 1/4 keV flux by the Draco molecular cloud, known to be at least 600 pc away

(Snowden et al. (1991), Burrows & Mendenhall (1991)). This proved that at least some of the 1/4 keV emission originated at large distances. This was confirmed by an extensive follow-up study using the all-sky survey data which found that, in selected directions, up to 50% of the observed emission originated in a patchy million degree Galactic halo (Snowden et al., 1998). Averaged over the entire sky, the halo component accounts for about 11% of the total observed 1/4 keV flux (Bellm & Vaillancourt, 2005). This seemed to complete the 1/4 keV picture: a Local Bubble that contained hot gas filling the irregularly shaped local HI cavity provided most of the observed 1/4 keV flux, with a patchy halo and the extragalactic AGN spectrum beginning to contribute at high galactic latitude ($|b| > 30°$) where the absorbing column density decreases.

However, even before all the pieces of the puzzle had been put in to place, there were indications that the situation may not be so simple. In 1993 the Diffuse X-ray Spectrometer (DXS), a payload attached to the space shuttle, obtained a spectrum of the 1/4 keV background using a Bragg-crystal spectrometer with 4-14 eV FWHM energy resolution. The observations were low latitude, so most of the observed emission must have originated nearby, presumably in the Local Hot Bubble. Thanks to the good energy resolution, strong emission lines were observed for the first time, supporting the interpretation that the source was thermal. However, the spectrum obtained was not consistent with either collisional equilibrium or non equilibrium ionization models for an astrophysical plasma (Sanders et al., 2001). Though the energy resolution of DXS was far better than any of the previous experiments, it was still unable to resolve most of the closely spaced low energy lines. The failure of the thermal models to fit the blended lines highlighted the uncertainty that remained in both the emission models and the completeness of the astrophysical picture.

In 1996 Lisse et al. observed the comet Hyakutake with ROSAT and made the surpris-

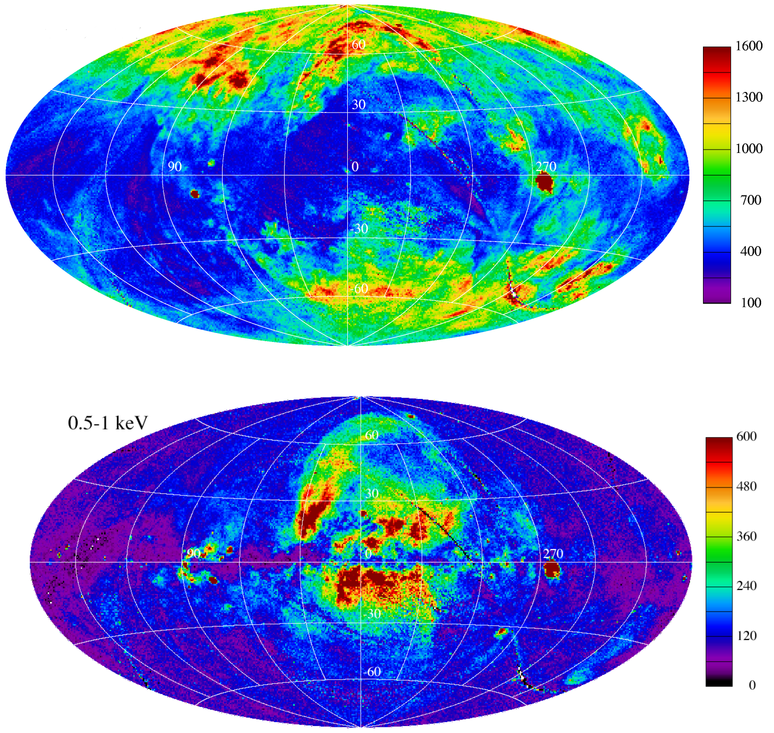

Figure 1.1: Maps of the 1/4 (top) and 3/4 keV (bottom) energy bands from the ROSAT all-sky survey (Snowden et al., 1997). Maps show intensities in units of 10^{-6} counts/second/arcmin^2.

ing discovery that the comet appeared to be a bright source of X-rays. Shortly thereafter Cravens (1997) proposed that a process called Solar Wind Charge Exchange (SWCX) could explain the emission from Hyakutake. In charge exchange interactions an ion that encounters a neutral atom or molecule can capture an electron from the neutral. The electron is captured into the n state of the ion that is closest to the electron's energy level in the neutral. As it decays to the lowest available energy state it will radiate, and for common Solar wind ions this radiation can be at UV or soft X-ray energies. In the comet's case, the Solar wind provides the stream of highly charged ions and the neutrals come from the cometary atmosphere. It was quickly realized that any place the Solar wind encountered a population of neutral atoms could produce charge exchange emission, including Earth's atmosphere and the H and He from the ISM streaming into the heliosphere. In fact, Cox (1998) proposed that charge exchange interaction between the Solar wind and Earth's geocorona could provide an explanation for the day-scale temporal variations that were observed in the ROSAT all-sky survey (dubbed "Long Term Enhancements," or LTEs by Snowden et al. (1994)). Simple models for the SWCX process showed that it was a plausible explanation for the LTEs, and furthermore, that heliospheric SWCX (which would not be significantly time variable) might account for up to half of the observed 1/4 keV X-ray flux (Cravens et al. (2001), Robertson et al. (2001)). Later attempts to model the heliospheric emission indicated that nearly all of the 1/4 keV emission in the Galactic plane might be attributed to SWCX (Koutroumpa et al., 2009).

The discovery of bright SWCX emission raised major questions about the validity of the Local Hot Bubble model. If a non-thermal emission mechanism was contributing a significant fraction of the local emission, then the temperature, spatial extent, pressure, abundances, and ionization state derived for the LHB by considering only thermal sources would be incorrect. Resolving the problem has proven very difficult due to the uncertainty in the charge exchange cross sections, which are difficult to calculate and highly velocity dependent in the range of Solar wind velocities (Dennerl, 2010). The difficulty of the calculations coupled with a lack of laboratory data to check them means that rather than being able to rely on models to identify the SWCX contribution, we will need more astrophysical data. The DXL sounding rocket mission in 2012 measured the heliospheric SWCX contribution directly by using a proportional counter detector to scan across the helium focusing cone, a high-density region where interplanetary He is gravitationally focused downstream of the Sun. The enhanced neutral density in this region should result in enhanced SWCX emission. This observation was compared to the ROSAT data along the same scan path, which was taken when the satellite was not looking through the focusing cone. Using well-determined models for the interplanetary neutral density along both lines of sight, the authors found that SWCX contributes 40% of the observed ROSAT flux in the Galactic plane and about 27% averaged over the entire sky (Galeazzi et al., 2014).

The DXL mission has showed us that both SWCX and the Local Hot Bubble contribute significantly to the 1/4 keV spectrum, and some 40 years after the LHB was first theorized, a comprehensive model of the local ISM seems within reach. But given the failure of global models in fitting the observed unresolved line complexes and the uncertainties introduced by our limited understanding of the charge exchange spectrum, full understanding of the soft DXRB will require high resolution spectroscopy.

1.2 X-ray Instrumentation

The need for higher quality data to understand astrophysical X-ray production has been a steady driver for improvement in instrumentation. The Geiger counters flown by Giacconi that discovered the diffuse background were quickly replaced with proportional counters for lower background and the ability to do limited spectroscopy. Proportional counters are chambers filled with inert gas that is ionized by incident photons. The charge is collected by a high voltage anode wire. Since the number of ion pairs produced is proportional to the incident energy, the charge measured can be used to reconstruct the energy spectrum of incident radiation. However, the energy resolution is limited by the statistical fluctuations in the branching fraction of the deposited energy that goes into ionization (about 1/3). The fluctuations can be expressed as $\sqrt{fWE}$, where W is the ionization energy, E is the incident energy, and f is the Fano factor, a number between 0 and 1 that describes the suppression of Poisson fluctuations due to the finite ionization energy (Fano, 1947). For argon-methane mixtures typically used in these counters, W is about 29 eV and f about 0.2 (Jahoda & Mccammon, 1988). Therefore, the best energy resolution achievable with a proportional counter is typically in the hundreds of eV, and it is difficult to obtain resolving power much higher than 1 ($R = E/\Delta E$) in the soft X-ray. To get some spectral information at low energies, experimenters typically used atomic absorption edge filters, thin windows made of materials like beryllium, boron, and carbon. Despite these limitations, proportional counters were the workhorse of X-ray astronomy from the 1970s through the 1990s, used in sounding rocket surveys and the ROSAT mission due to their durability, ease of use, spatial resolution, high efficiency and large effective area.

In the past 20 years, proportional counters have been largely supplanted by CCDs. Since CCDs are still ionization detectors, they face the same fundamental limit on their energy resolution. However, with a lower Fano factor (f = 0.115, Mendenhall et al. (1996)) and ionization energy ($W = 3.65$ eV Janesick et al. (1988), the energy resolution can be good enough to resolve some astronomically important lines in the 500-1000 eV range (for example, the O VII triplet complex at 570 eV). Individual pixels tend to be tens of microns in size, and megapixel arrays are common. This makes CCD detectors a good match to current state of the art X-ray imaging optics. For example, the ACIS CCD on the Chandra satellite has four 1026 $\times$ 1024 arrays of 24 μm $\times$ 24 μm pixels that subtend 0.492 arcsec at the focal plane with energy resolution of 100-250 eV(Garmire et al., 2003). The XIS CCD camera on the satellite Suzaku is also a megapixel array with energy resolution as good as 50 eV FWHM at 250 V, although the effective area of the instrument drops off sharply at low energies (Bautz et al., 2004). These space-based CCD detectors have been highly successful, but their fundamental energy resolution limit is still too poor to spectrally resolve most of the closely-spaced emission lines that constitute the majority of the diffuse X-ray background below 1 keV.

One way to achieve higher spectral resolution is to use a wavelength dispersive instrument. For example, the Diffuse X-ray Spectrometer (DXS) experiment used Bragg crystals to disperse X-rays onto a position sensitive proportional counter to get resolving power $R = 25 - 40$ (Sanders et al., 2001). Newer instruments, such as the High Energy Transmission Grating (HETG) instrument on Chandra, couple grating spectrometers to CCD arrays for resolving powers of up to 1000 over the 0.4-8 keV energy range (Canizares et al., 2005). However, these instruments have very low efficiency and their resolving power is degraded when observing extended sources. Therefore, they are most effective for looking at bright point sources.

Without any current (or planned) X-ray telescopes capable of delivering the energy resolution and effective area necessary to resolve the local 1/4 keV background, the only way to get this information is with a dedicated instrument. A sounding rocket payload is the natural choice for such an experiment given the lower cost and shorter development time relative to a satellite mission. The spectrum of the 1/4 keV background is made up of dozens of closely packed emission lines from the common heavy elements in a variety of charge states. Figure 1.2 shows a simulation of a 1 MK diffuse plasma in collisional ionization equilibrium, nominally what is expected for the Local Hot Bubble emission. The SWCX contribution will be superimposed on this spectrum, and is expected to contain many of the same emission lines but with different relative strengths. To resolve most of these lines requires energy resolution of 2 eV FWHM or better (see Figure 1.3).

Considering the disadvantages of using a wavelength-dispersive instrument to observe an extended diffuse source, we would like to turn to an energy-dispersive detector. However, building a detector with large effective area and good energy resolution with a broad acceptance angle is not a trivial task. Microcalorimeters are a promising technology for such an instrument. Microcalorimeters are near-equilbrium thermal detectors, and as such

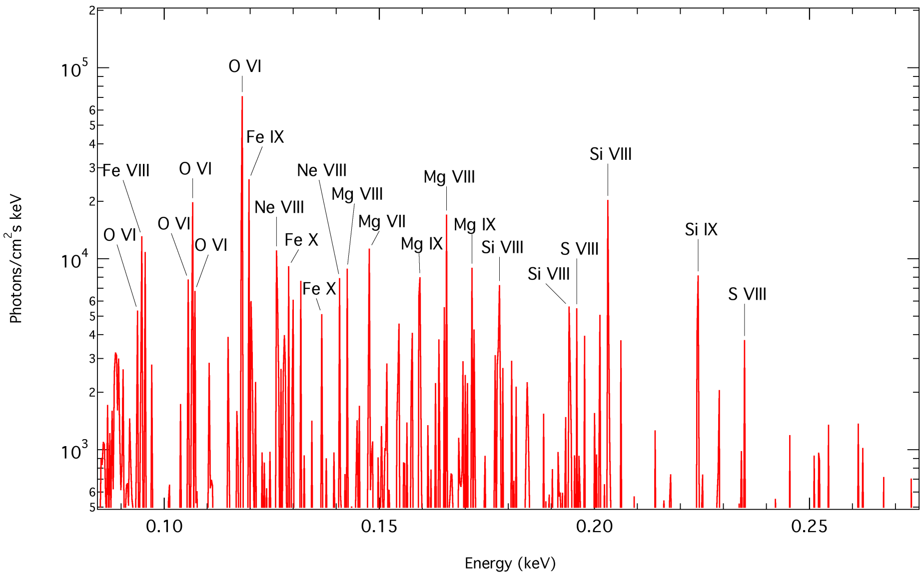

Figure 1.2: Emission spectrum of an optically-thin plasma with solar abundances in collisional ionization equilibrium at 1 × 10^6 K, similar to what is believed to fill the Local Hot Bubble. Calculated using the APEC model in XSPEC (Dorman & Arnaud, 2001; Arnaud, 1996).

are not subject to the statistical fluctuations that limit ionization detectors. The X-ray Quantum Calorimeter (XQC) is a microcalorimeter spectrometer with 1.4 cm^2 detector area, a 1 sr field of view, and 8-10 eV FWHM energy resolution in the 0.05-1 keV energy range. XQC uses implanted silicon thermistors to detect the temperature change that occurs when an X-ray is absorbed in the detector. To measure such small temperature changes, the detectors must be cooled to 50 mK in a compact Adiabatic Demagnetization Refrigerator (ADR) that can be placed on a sounding rocket. Although 2 eV resolution is out of reach for XQC's silicon thermistors, transition-edge sensor (TES) microcalorimeters have been developed with sub-eV energy resolution in the soft X-ray (Bandler et al., 2013).

The Micro-X collaboration is currently developing a sounding rocket payload to operate the first TES microcalorimeter in space. The goal of the instrument is to image a supernova remnant, so the instrument is designed with focusing optics and the detector

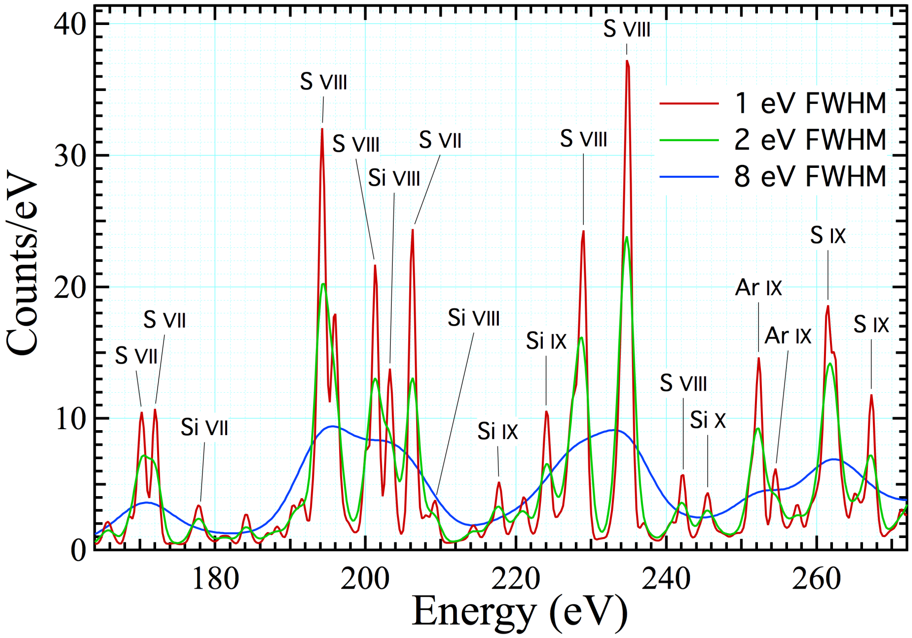

Figure 1.3: Portion of the spectrum from a typical diffuse background measurement with 1 ev, 2 eV, and 8 eV energy resolution. Assumes a 250 s observation, 2 cm^2 total area, 0.25 sr field of view, and depleted abundances for the Local Hot Bubble emission. Calculated using the APEC model in XSPEC (Dorman & Arnaud, 2001; Arnaud, 1996).

array is small, only 0.5 cm^2 Wikus et al. (2009). Micro-X, as designed, does not have the effective area necessary to study the 1/4 keV background. However, by removing the imaging optics and making small modifications to widen the field of view, the Micro-X cryostat could be repurposed for this experiment. This would save years of development work that go into designing and building a full payload. The cryostat's field of view could reasonably be expanded to 1/4 sr, so a minimum of 2 cm^2 of total detector area at near-unity quantum efficiency would be necessary to collect enough counts to make a useful spectrum in the 300-second duration of a typical sounding rocket flight (for comparison, the XQC array flown prior to 2008 was 0.36 cm^2 with a 1 sr FOV). Micro-X is planned to have 256 readout channels, which means that individual pixels must have at least 890 μm × 890 μm of absorbing area. Therefore, to perform this experiment we must produce a transition-edge sensor thermometer coupled to an 890 μm × 890 μm X-ray absorber with near-unity quantum efficiency and at least 2 eV FWHM energy resolution at 250 eV. The rest of this thesis describes the design and prototype testing of this device.

Chapter 2

General theory of microcalorimeters

Detector design is ultimately an optimization problem. The idea is to vary a set of parameters over which we have control (materials, operating conditions, device geometry, etc.) to maximize the resolving power ($R = E/\Delta E$). There are a variety of constraints, which tend to reflect the necessity of keeping the project grounded in reality. For example, the limited number of readout channels sets the minimum surface area per pixel, and the minimum temperature at which the detectors can operate is set by the sort of cryogenic equipment we can reasonably expect to operate on a spacecraft. To optimize our detector, we have to understand how the physical properties of a microcalorimeter determine its energy resolution. Then, we can assess which parameters are most important, how those parameters are related to one another, and how we might tune them to achieve the best ΔE.

In this chapter, I'll give a brief overview of the important equations governing the performance of microcalorimeters. We'll start with basic operating principles, then discuss signal analysis and the fundamental sources of noise that limit our ability to measure signals. This will lead us to write an expression for the energy resolution in terms of these fundamental noise sources and examine its dependence on the physical properties of the detector. To keep this section brief, I'll try to highlight the important results without going through first principles derivations. The derivations for these expressions have been done in great detail by numerous authors beginning with John Mather in 1982, whose work has been expanded upon more recently (and more readably) by McCammon (2005), Irwin & Hilton (2005), Galeazzi & McCammon (2003), and Figueroa-Feliciano (2001).

2.1 Thermal and electrical properties

A microcalorimeter is a near-equilibrium thermal detector. Non-equilibrium devices measure only a fraction of the incident energy as it is deposited into a particular detection channel and are limited by the statistical fluctuations in that branching ratio. Near-equilibrium thermal calorimetry has, in principle, no fundamental limit to energy resolution (of course, real devices have fundamental sources of noise that ultimately limit their accuracy, as will be discussed later in this chapter). As shown in Figure 2.1, in the simplest case a calorimeter is comprised of three components: an absorber that thermalizes the incident energy, a thermometer to measure the temperature increase, and a weak thermal link to a heat sink to cool the absorber back to its equilibrium temperature. The absorber has some heat capacity C, so when a photon with energy E_0 is absorbed, the temperature rise will be proportional to the incident energy, $\Delta T = E_0/C$. The temperature of the absorber will decay back to the bath temperature with a time constant $\tau = C/G$, where G is the thermal conductance of the weak link.

The thermal response of the calorimeter can be described by the following differential equation:

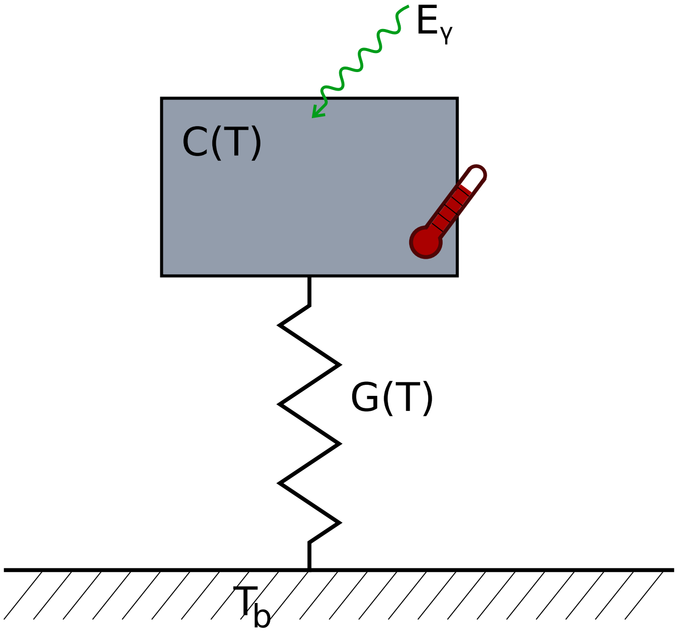

Figure 2.1: A simple calorimeter consists of an absorber with heat capacity C(T) that thermalizes the incident energy E$_\gamma$, a thermometer to measure the temperature increase, and a weak thermal link G(T) to a heat sink to cool the absorber back to its equilibrium temperature.

$$C(T)\frac{dT}{dt} = P_{el} + P_{th} - P_{bath} + P_\gamma \tag{2.1}$$

where P_{el} includes all electrical power dissipated within the thermometer by the readout circuitry, P_{th} accounts for any external thermal power inputs (thermal radiation and vibration), P_γ is the signal power due to absorption of a photon, and P_{bath} is the power that flows from the device to the heat sink through the weak thermal link. For the purposes of this discussion, we will restrict ourselves to the case of a resistive thermometer (or "thermistor"), where the resistance of the sensor is function of temperature. Then, the power P_{el} will include the Joule power dissipation in the thermometer, given by $P_J(T) = I(t)^2R(I,T)$.

The power output to the heat sink P_{bath} depends on the physics of the weak link. First, we define the differential thermal conductance of the weak link, $G \equiv dP_{bath}/dT$, for G and T at the detector end of the link. To keep the equations simple, we can work in a limit where the signal power P_γ is small, so properties like the resistance of the thermometer do not change much during an absorption event. However, the temperature increase produced by Joule heating is not necessarily small, so the operating temperature for the device may be significantly higher than T_0, and we must account for the temperature dependence of the detector's heat capacity and the link thermal conductivity. We assume a power-law temperature dependence for G given by:

$$G(T) = G_0 \left(\frac{T}{T_0} \right)^{n-1} \tag{2.2}$$

where $G_0 \equiv G(T_0)$. The functional form of P_{bath} is then given by:

$$P_{bath} = K(T^n - T_b^n) \tag{2.3}$$

The temperature of the bath is T_b, and the prefactor $K \equiv G/n(T^{n-1})$. The value of n is material dependent and is known fairly accurately over the typical temperature range for microcalorimeter operation (tens to hundreds of mK), with $n = 2$ for metals, 4 for insulators, 5 for electron-phonon coupling in metals, and approximately 6 for electron-phonon coupling in semiconductors (McCammon, 2005). Likewise, we assume a temperature dependence for the heat capacity of $C(T) = C_0(T/T_0)^\gamma$, with $\gamma = 1$ for metals and 3 for dielectrics. The heat capacity and thermal conductivity define the natural thermal time constant of the system, $\tau_0 \equiv C/G$.

In order to build a functional device, the "thermal circuit" consisting of the absorber, thermometer, thermal link, and heat sink, must be coupled to an electrical circuit to read out signals from the thermometer. In the most general terms, the electrical circuit simply consists of a current or voltage bias applied to the thermometer and an amplifier to facilitate measurement of the small changes in resistance that result from the absorption of a photon. The choice of current or voltage bias (controlled by the addition of a load resistor) effects the output signal via what is called electrothermal feedback. When a bias is applied to the thermometer, the power dissipated contributes to the total thermal power input. If the resistance of the thermometer increases with temperature, then for a constant voltage bias ($R_{therm} \gg R_L$), the Joule power $P_J = V^2/R_{therm}$ decreases with increasing temperature. This negative feedback tends to stabilize the device, providing a restoring force that protects again thermal runaway. It also speeds up the pulse fall time, giving the pulses an effective time constant that is shorter than the thermal decay time, $\tau_{eff} < \tau_0 = C/G$. Since the application we will be considering in the following chapters is a TES thermometer for which the resistance increases with temperature, we will restrict ourselves to the voltage-biased case (also referred to as current readout) for the rest of this discussion.

Combining the electrical and thermal circuits (see Fig. 2.2) allows us to convert a change in temperature caused by an absorption event P_γ into a change in bias current running through the thermometer. This is called the responsivity of the thermometer, $S_I(\omega) \equiv dI/dP_\gamma$, defined as the current signal measured by the thermometer for a given thermal power input.

In a TES thermistor, the resistance is a function of current as well as temperature. This is referred to as "thermometer nonlinearity." For small signals, we can expand the thermometer resistance $R(T, I)$ around the steady-state resistance, temperature, and current (R_0, T_0, I_0):

$$R(T, I) \approx R_0 + \frac{\partial R}{\partial T}_{I_0}(T - T_0) + \frac{\partial R}{\partial I}_{T_0}(I - I_0) \tag{2.4}$$

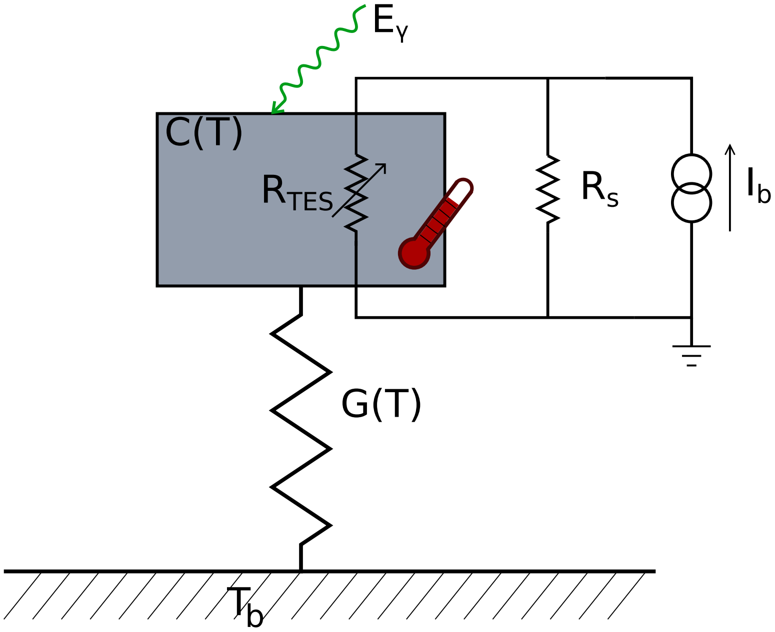

Figure 2.2: A calorimeter with a simple readout circuit. The size of R_S can be varied relative to the thermometer resistance R_{TES} to provide a constant voltage or constant current bias.

This leads us to define the logarithmic temperature sensitivity:

$$\alpha \equiv \left.\frac{\partial log R}{\partial log T}\right|_{I_0} = \left.\frac{T_0}{R_0}\frac{\partial R}{\partial T}\right|_{I_0} \tag{2.5}$$

and current sensitivity:

$$\beta \equiv \left.\frac{\partial log R}{\partial log I}\right|_{T_0} = \left.\frac{I_0}{R_0}\frac{\partial R}{\partial I}\right|_{T_0} \tag{2.6}$$

These can be substituted into the expression for resistance, giving

$$R(T, I) \approx R_0 + \alpha\frac{R_0}{T_0}(T - T_0) + \beta\frac{R_0}{I_0}(I - I_0) \tag{2.7}$$

2.2 Optimizing energy resolution

As previously explained, there is no fundamental limit to the accuracy of an energy measurement made with a thermal equilibrium calorimeter. However, in practice, irreducible sources of noise associated with the thermal system and resistive thermometer determine the resolution of real devices. Therefore, it is important to understand how the properties of the device, such as operating temperature, heat capacity, and sensitivity (α) relate to the theoretical energy resolution.

Achieving the "best energy resolution" is another way of saying that we would like to obtain the best possible estimate of a parameter E_γ, in this case, the energy of the incident photon. Working in the small-signal limit, we start with a measurement of a signal $D(t) = E_\gamma f(t) + i_n(t)$, where $f(t)$ is the invariant pulse shape, and $i_n(t)$ is the noise. The accuracy of our estimate of E_γ will be limited by this noise. This problem can be solved exactly provided the system is linear, which means we make two important assumptions:

1. The signal is linear. That is, $f(t)$ is known and independent of E_γ.
2. The noise is stationary. The spectral shape of $i_n(f)$ is known and does not change with time.

The first assumption will hold as long as the thermometer resistance is a linear function of temperature which is a good approximation over a limited input energy range. We can, however, easily imagine a situation in which neither assumption would be valid. For example, we know resistive thermometers have Johnson noise, we know Johnson noise is a function of resistance, and we know the resistance of our thermometer will change during an absorption event, resulting in both non-stationary noise and a non-linear signal. However, we'll forge ahead for now, assuming these effects will be small enough to ignore (and revisit that assumption in Chapter 3). Accepting these assumptions allows us to use the optimal filter method, outlined by Szymkowiak et al. (1993). A detailed walkthrough of the derivations can be found in McCammon (2005).

The idea is to make an estimate of the pulse height using the average pulse shape and average noise to minimize, in the least square sense, the difference between the noisy pulse and the average pulse. We find that the optimal filter is given by $\hat{s}(f)/i_n^2(f)$, where $\hat{s}(f)$ is the complex conjugate of the Fourier transform of the signal $f(t)$. Multiplying the signal by the optimal filter yields the best estimate of the input signal amplitude. Since constructing the optimal filter is essentially just maximizing the signal to noise ratio $E/\Delta E_{rms}$, we can also write an expression for the theoretical energy resolution (see, for example, Moseley et al. (1984)):

$$< \Delta E_{rms}^2 >= \frac{1}{4\int_0^\infty \frac{|s(f)|^2}{i_n^2(f)} df} \tag{2.8}$$

The pulse shape (without noise) is given by $E_\gamma s(f) = E_\gamma S_I(f) p(f)$, where $S_I(f)$ is the responsivity and the function $p(f)$ is the Fourier transform of $P_\gamma(t)$, and describes the power input to the detector. Now, we can write:

$$< \Delta E_{rms}^2 >= \frac{1}{4\int_0^\infty \frac{|S_I(f)|^2 |p(f)|^2}{i_n^2(f)} df} \tag{2.9}$$

If we assume that when a photon is absorbed the power is deposited in the detector instantaneously, then we can treat the power input as a delta function at $t = 0$, so $p(f) = 1$. Then,

$$< \Delta E_{rms}^2 >= \left(\int_0^\infty \frac{4df}{NEP^2} \right)^{-1} \tag{2.10}$$

where NEP is the noise equivalent power, $NEP(f) \equiv i_n(f)/S_I(f)$, the equivalent input referred power needed to produce a given output noise. Therefore, to calculate the theoretical energy resolution of a detector, we must determine the noise equivalent power for each source of noise, then sum these in quadrature to give the total NEP (assuming the various noise sources are uncorrelated). This result shows that predicting the performance of a device is a matter of identifying and quantifying the responsivity and all of the possible sources of noise in the system.

2.3 Fundamental sources of noise

Thermodynamic fluctuation is an unavoidable effect in any microcalorimeter. This includes statistical fluctuations associated with exchange of energy between the detector and the heat sink, called thermal fluctuation noise (TFN). For a resistive thermometer, we must also consider Johnson noise, the thermodynamic fluctuations associated with electrical resistance. There are two sources of Johnson noise in our system, the thermometer itself and the load resistor. On top of these thermodynamic noise sources, we should consider any amplifier noise produced by the readout.

Thermal fluctuation noise is produced by power flow over the thermal link G (see Eq. 2.2). From statistical mechanics, assuming the power spectrum is independent of frequency, we can derive an expression for the spectral density of this power (Irwin & Hilton, 2005):

$$p_{TFN}^2 = 4k_B T_0^2 G \cdot F_{link}(T_0, T_b) \quad \mathrm{W^2/Hz} \tag{2.11}$$

If the thermometer and the bath are in thermal equilibrium ($T_0 = T_b$), then the function $F_{link} = 1$. However, when there is bias power applied to the detector, the thermometer temperature will be higher than the bath, and the form of F_{link} depends on the detailed physics of the link. There are two important limiting cases to consider. In the radiative limit the mean free path of the carriers is long relative to the length of the link, and the dominant scattering mode is through mirror-like reflections from the boundaries. In this case,

$$p_{TFN}^2 = 2k_B T_b^2 G_b \left[\left(\frac{T_0}{T_b} \right)^{n+1} + 1 \right] \quad \mathrm{W^2/Hz} \tag{2.12}$$

as derived by Boyle & Rodgers (1959). Here T_b is the temperature of the bath, G_b is the thermal conductivity at T_b, and n is the exponential temperature dependence of $G(T)$ (see equation 2.2). Alternatively, if the mean free path is small compared to the length, the scattering is diffusive, and we have:

$$p_{TFN}^2 = 4k_B T_b^2 G_b \left(\frac{n}{2n+1} \right) \left(\frac{t^{2n+1} - 1}{t^n - 1} \right) \quad \mathrm{W^2/Hz} \tag{2.13}$$

for $t \equiv T_0/T_b$, as derived by Mather (1982). For most real-world cases (where the scattering is neither perfectly diffuse nor perfectly specular), the value of $F(T_0, T_b)$ is between 0.5 and 1 (Irwin & Hilton, 2005). The corresponding output noise spectral density $i_n(f)$ is obtained by multiplying p_{TFN} by the responsivity of the detector $S_I(f)$, so remembering our definition for the noise equivalent power, we see that $NEP_{TFN} = p_{TFN}$.

For the thermometer and load resistor, respectively, we use the classical spectral density for a Thevenin-equivalent random current in parallel with a noiseless, temperature dependent resistance (see McCammon (2005)):

$$i_{nJ} = \sqrt{4k_B T_0/R_0}\left(\frac{b}{1+b\beta}\right)\cdot K \quad \mathrm{A}^2/\mathrm{Hz} \tag{2.14}$$

$$i_{nJ-load} = \sqrt{4k_B T_L/R_L}\left(1-\frac{\frac{\alpha P}{GT}}{1+i\omega\tau_0}\right)\frac{b}{1-b\beta}\frac{R_L}{R_0}\cdot K \quad \mathrm{A}^2/\mathrm{Hz} \tag{2.15}$$

where T_L is the temperature of the load resistor (often $T_L = T_b$) and we have defined $K \equiv \frac{\tau_{eff}}{\tau_0}\cdot\frac{1+i\omega\tau_0}{1+i\omega\tau_{eff}}$ and $b \equiv \frac{R_0}{R_0+R_L}$. It's important to point out here that in writing down these expressions, we've made an important assumption: we've ignored the contribution of the current dependence of the resistance in determining the Johnson noise. This simplification was introduced by Mather (1982). We'll accept its validity for now and proceed, but revisit it later in Chapter 3 when discussing additional sources of noise in transition-edge sensors.

The thermal noise from these three sources (the thermal link, the thermometer resistance, and the load resistor) is summed in quadrature to obtain the total NEP. Thus far, we have neglected the amplifier noise. Since TES detectors tend to be low-impedance devices they are a good match to low-noise SQUID current amplifiers, and this has become the de-facto way to read out TES devices. For now, we will leave the SQUID noise out of our expression for the NEP. This is not a bad approximation, since SQUID amplifiers are available with noise that is small compared to the thermal noise in many TES detectors. Since our ultimate goal is to understand the dependence of the NEP (and therefore the energy resolution) on detector parameters (such as heat capacity and thermometer sensitivity), in some sense the amplifier noise can be considered a separate problem.

Summing the contributions from the various noise sources, we can substitute into Equation 2.10 and integrate to obtain the energy resolution. We can write out the full results as follows. Note that the factor of $2\sqrt{2\ln(2)} = 2.355$ is added to convert ΔE_{rms} to ΔE_{FWHM}. In the future, ΔE or "energy resolution" will refer to ΔE_{FWHM}.

$$\Delta E = 2.355\sqrt{\frac{4k_bT_0^2C}{\alpha}\sqrt{\left(\frac{I(R_0+R_L)}{PL}\right)^2\left(L^2T_0GF_{link}+I_0^2(R_0+(L-1)^2R_L)\right)}} \quad (2.16)$$

where we have defined $L \equiv \frac{\alpha P}{GT_0}$. The resolution is often written as $\Delta E = \xi\sqrt{k_bT_0^2C/\alpha}$ to highlight the dependance on T_0^2, C, and α, and the function ξ contains the physics of the weak link (specular or diffuse reflections) and the temperature dependence of its thermal conductivity. From this expression, it is clear that the lower the device temperature, the better, since the energy resolution depends linearly on T_0. Reducing the heat capacity is also important. Therefore, we should choose materials with the smallest heat capacity possible, and operate at the lowest temperature we can reasonably achieve with our cryogenics, since C tends to decrease with temperature. Last, we see that energy resolution is better for larger α. This is not surprising if we recall that α describes the sensitivity of the thermometer, that is, how quickly the resistance changes with temperature. Armed with these expressions for the sensitivity and resolution of a thermistor, we can predict the performance of a detector based on the properties of the materials we choose.

Chapter 3

Transition-edge sensors

3.1 Introduction

A transition-edge sensor (TES) is a superconducting film operated in the transition region between the superconducting and normal states. Because resistance increases with temperature ($\alpha > 0$), TESs are typically voltage-biased to provide negative feedback and maintain stability against thermal runaway. With the substrate cooled to well below the superconducting transition temperature, negative electrothermal feedback can be used to self-bias the film in its transition region. The resistance of the film drops as the temperature is decreased, and consequently the Joule heating (V^2/R) increases. When the power dissipated by Joule heating matches the heat flowing to the substrate via the thermal link, the film reaches a stable equilibrium. When an X-ray is absorbed, the temperature and resistance increase and the Joule heating decreases, so the TES cools back down to its equilibrium temperature more quickly than it would in the absence of feedback.

As shown in chapter 2, for best performance it is desirable to operate microcalorimeters at low temperatures. The lower limit is generally imposed by the available cryogenic systems. For example, helium-3 coolers with sorption pumps can reach temperatures of 0.2-0.3 K, which can be maintained for up to several days, depending on the size of the reservoir. ^{3}He refrigerators are commonly used to cool infrared bolometers (identical in principle to microcalorimeters, but used to read out a constant power instead of individual photon absorption events), such as the SPIRE instrument aboard the Herschel observatory. For high resolution spectroscopy experiments where background levels are typically much smaller, colder temperatures are needed. Dilution refrigerators can achieve base temperatures down to a few millikelvin. However, these systems are large, expensive, and classical systems rely on gravity to work, preventing their use in space missions. Therefore, adiabatic demagnetization refrigerators (ADRs) are frequently used to cool X-ray and gamma ray microcalorimeters, as they can provide base temperatures in the 40-100 mK range.

Given that we would like to operate our TES detectors as cold as possible, and equipped with refrigeration techniques that will enable us to maintain a bath at $\sim$50 mK, we would like to produce superconducting films with transition temperatures around 60-80 mK. At first glance, it appears our options for producing such films are quite limited. In fact, the only elemental superconductors with transition temperatures close to 100 mK are hafnium (0.165 K, Matthias et al. (1963)) and iridium (0.14 K, Hein et al. (1962)); most elements have transition temperatures ranging from 0.5 to a few kelvin.

Fortunately, we can use the proximity effect to create a superconducting/normal metal bilayer with a transition temperature that is lower than the bulk T_c of the superconducting layer. The relative thicknesses of the layers can be changed to produce the desired critical temperature. In principle, it is possible to calculate the suppressed T_c from the two thicknesses. Using the theory developed by Usadel (1970), a generalization of the microscopic equations of the BCS theory of superconductivity, Martinis et al. (2000) find that the new T_c is given by:

$$T_c = T_{c0}\left[\frac{d_s}{d_0}\frac{1}{1.13(1+1/\alpha)}\frac{1}{t}\right]^{\alpha} \tag{3.1}$$

where $\alpha \equiv d_n n_n/d_s n_s$, $d_0 \equiv (\pi/2)k_B T_{c0}\lambda_f^2 n_s$, T_{c0} is the critical temperature of the pure superconductor, d_s and d_n are the thicknesses of the superconductor and normal layers, respectively, and the n_s and n_n represent the the density of states. The parameter λ_f is the Fermi wavelength. Finally, t is a transmission coefficient that describes the interface conductivity. In practice, this parameter is difficult to predict as it depends on the details of the interface layer, which is highly process dependent. Therefore a group will typically make a series of bilayers of varying thicknesses and measure their transition temperatures to experimentally determine t. One can then make bilayers with any desired transition temperature, so long as the fabrication process remains stable.

A variety of materials have been used to fabricate bilayer TESs. It is advantageous to keep the resistance of the TES low, since the rate of heat diffusion can limit the detector response time and Joule heating can cause temperature variation across a device, which reduces the sensitivity (Irwin et al., 1998). Therefore the normal metal layer is often chosen to be a high-conductivity metal, such as Cu, Ag, or Au. Choosing the superconductor is a matter of selecting a material with favorable properties and a convenient bulk transition temperature. Initial attempts used Ir/Au bilayers to achieve critical temperatures as low as 33 mK (Nagel et al., 1994). Shortly thereafter, a group demonstrated that T_c could be suppressed by more than an order of magnitude in aluminum ($T_c = 1.17$ K, Cochran & Mapother (1958)). This simplified fabrication because the aluminum could be evaporated onto a room temperature substrate, followed immediately by the deposition of the normal metal layer (Irwin et al., 1996). However, Al is not chemically stable when combined with any noble metal (Cu, Ag, or Au), and has many intermetallic phases that can form at high temperatures. Molybdenum and titanium have become popular alternatives. Although molybdenum must be evaporated at elevated temperatures, it can also be deposited at room temperature by magnetron sputtering (Irwin & Hilton, 2005).

The X-ray TES group at Goddard Space Flight Center (GSFC), who fabricated all the devices used in this project, make their TES devices with Mo/Au bilayers. Molybdenum is less diffusive than aluminum in bilayers, and both molybdenum and gold are highly corrosion resistant. Molybdenum can form silicides when deposited on silicon, so a diffusion barrier of silicon oxide or silicon nitride is needed. Silicon nitride is often used to provide the weak thermal link between TES devices and the bath (the silicon wafer), so this provides a convenient barrier against silicide formation (Finkbeiner et al., 1999). The GSFC group has shown that devices can be engineered with transition temperatures ranging from 70-600 mK and with transition widths less than 1 mK, corresponding to α as high as 2500 (Chen et al., 1999).

In addition to the advantages afforded by electrothermal feedback and being able to choose the transition temperature, TESs have a number of other features that make them attractive for use as microcalorimeters. For example, the potential for very high α values allows more flexibility to use materials with higher heat capacity. Being able to use normal metals like gold in absorbers can improve thermal conductivity and response times. Additionally, metal absorbers can be electroplated or evaporated directly onto the TES, unlike materials such as HgTe that had been used in the past with silicon thermistors and had to be manually attached to sensors after fabrication (e.g. McCammon et al. (2002)). This simplifies the fabrication process and improves reproducibility and yield.

Transition-edge sensors are low impedance devices; typical normal state resistances are on the order of a few miliohms to a few ohms. They are poorly matched to common high-impedance room temperature amplifiers, such as FETs. In fact, the first TES bolometer was demonstrated in 1941 by Andrews et al., but they were not widely used because it would be another half-century before low-impedance amplifier development caught up in the form of superconducting quantum interference device (SQUID) current amplifiers. Although SQUID amplifiers must be operated at cold temperatures and are sensitive to magnetic fields, they have very low noise (SQUID noise can be small compared to the thermal TES noise) and have the significant advantage that they can be multiplexed. Multiplexing reduces the number of wires to the cold stage of a cryostat, keeping the heat load manageable and enabling readout of arrays of hundreds of pixels, a critical development for low-rate experiments.

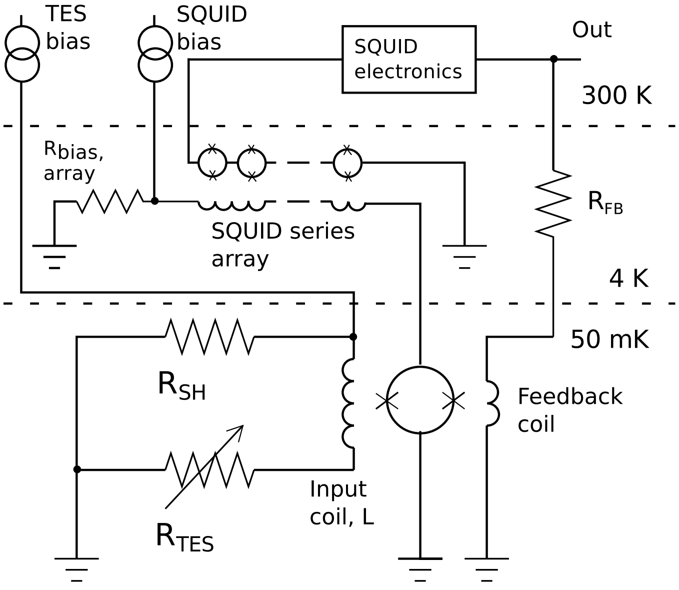

Figure 3.1: Two-stage SQUID readout circuit example. A current source supplies the bias, and when $R_{TES} \gg R_{SH}$ this produces a constant voltage bias across the TES. Changes in the TES resistance with temperature produce changes in the current through it, which are coupled to a SQUID amplifier via an input coil. That first stage SQUID sensor may then be connected to a series array of SQUIDs to provide further signal amplification.

SQUIDs are biased and read out with room temperature electronics. Because the voltage output from a single SQUID is very small, it is necessary to amplify this signal before it is coupled to a room temperature amplifier. This is frequently done using an additional series array of SQUIDs. An example of how such a circuit could be used to read out a TES is shown in Figure 3.1. In this scheme, a current source supplies the bias to the shunt resistance and TES in parallel. In normal operating mode with $R_{TES} \gg R_S H$, this produces a constant voltage across the TES, and negative electrothermal feedback. If, however, the TES is very low in the superconducting transition so that $R_{TES} \leq R_{SH}$, the device is no longer voltage biased, and the sign of the electrothermal feedback changes. The current through the sensor is coupled to a SQUID amplifier via an input coil with inductance L. That SQUID sensor may then be connected to a series array of SQUIDs to provide the necessary amplification for readout with room temperature electronics.

3.2 TES response to X-rays

Earlier, we found that the energy resolution of a thermistor microcalorimeter could be expressed as $\Delta E \propto \sqrt{k_b T_0^2 C/\alpha}$. Judicious choice of materials helps us control the heat capacity (C) of our detector. In the previous section we saw how to control the operating temperature of a TES bilayer to keep T_0 low. Now, we would like to design a TES with large α, that is, a sharp superconducting-to-normal transition. To do this we would like to predict, based on the materials we choose and the geometry of the sensor, how the resistance of the bilayer will change with temperature and current. Unfortunately, an accurate and comprehensive model for the superconducting transition has proven elusive. Instead, several models have been developed that address different aspects of TES behavior, such as the onset of resistance, the relationship between critical current and sensitivity, or response to applied magnetic fields. In this section, we will review several of these models and the areas of parameter space in which they prove most useful.

In chapter 2, we defined the temperature sensitivity $\alpha = (R_0/T_0)(\partial R/\partial T)$ and the current sensitivity $\beta = (R_0/I_0)(\partial R/\partial I)$ for a thermistor. In a TES, the current sensitivity β can have a significant effect on the response of the device. Experimental data has shown that the transition tends to both shift in temperature and broaden as the bias current increases (Lindeman et al., 2008). Rather than a simple resistance versus temperature curve, we can think of the transition as a surface where the resistance is a function of both I and T (see Fig. 3.2). Detailed characterization of the transition surface enables the device to be optimally biased for best energy resolution.

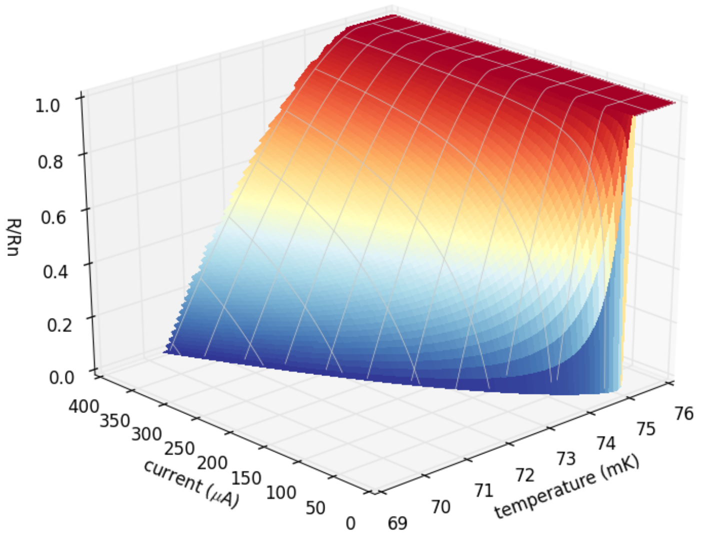

Figure 3.2: Theoretical R(I,T) surface plot for a TES with T_c = 75 mK. Note that the transition both shifts in temperature and broadens as the current increases, a behavior that has been confirmed experimentally. Calculated using the two-fluid model, Equation 3.2.

The two-fluid model for TES resistance, proposed by Irwin et al. (1998), is based on a simplification of the Skocpol-Beasley-Tinkham (SBT) model for the voltage drop across phase-slips in a superconducting filament. In the SBT model, part of the bias current is carried by a local super-current, I_s and the rest of the current is carried by quasiparticles (Skocpol et al., 1974). In a phase-slip region, the bias current exceeds the local critical current I_c, which produces an electrical field. This field accelerates Cooper pairs in the super-current until I_s exceeds I_c, at which point all the current is carried by the normal current and I_s is re-established. The time-averaged super-current can be expressed as a fraction c_I of the critical current $c_I \equiv \bar{I}_s/I_c \approx 0.5$. Skockpol et al. find that the voltage difference needed to drive the normal current through a phase-slip region is given by $V = 2N\rho_\lambda \Lambda_{Q^*}(T)(I - c_I I_c(T))$, where N is the number of phase slip lines, ρ_λ is the normal resistance per unit length, and $\Lambda_{Q^*}(T)$ is the charge-imbalance relaxation length. The two-fluid model (the normal and superconducting currents are the two non-interacting "fluids") makes the simplifying assumption that c_I is constant in time, and neglects the weak temperature dependence of Λ_{Q^*}. Then, Irwin et al. (1998) rearrange the SBT expression for the voltage drop to write:

$$I(T) = c_I I_c(T) + V/(c_R R_n) \tag{3.2}$$

where the term $c_R \equiv 2N\rho_\lambda \Lambda_{Q^*}(T)/R_n$. To proceed, we need an expression for the critical current. We can use the standard Ginzburg-Landau form for the critical current near T_c, given by

$$I_c(T) = I_{c0}\left(1 - \frac{T}{T_c}\right)^{3/2} \tag{3.3}$$

where I_{c0} is the critical current at zero temperature. Now we can use Equation 3.3 along with partial derivatives of Equation 3.2 to derive expressions for α and β:

$$\begin{aligned}\alpha &= \frac{3}{2}c_I c_R \frac{R_n}{R_0}\frac{I_{c0}}{I_0}\frac{T_0}{T_c}\left(1-\frac{T_0}{T_c}\right)^{1/2}\\ \beta &= c_R\frac{R_n}{R_0}-1\end{aligned} \tag{3.4}$$

Bennett et al. (2012) compare the two-fluid model predictions for the current, α, and β to experimental results for a Mo/Cu bilayer TES with α = 200-500 and β = 0.5-2. They find that the two-fluid model is a good fit to measured current-voltage curves for $c_I = 0.5$ and $c_R = 1$. Measurements for α and β from the same device were better fit by $c_I = 0.5$ and $c_R = 0.55$. The model's prediction for the temperature and current dependence of α and β (respectively) was also generally in agreement with the data, although it could not account for the fine structure observed in α and β.

The two-fluid model is simple and easy to use, and is able to reproduce certain behaviors that have been observed in TESs, such as the shifting and broadening of the transition at increased current, and provides some insight into the dependencies of α and β. However, the model completely neglects the geometry of the device, and has no way to account for the effects of the superconducting leads or any added normal metal features (normal metal banks and bars are often added to devices to prevent superconducting shorts, or to suppress noise).

Experiments by the GSFC TES group have shown how important the effects of device geometry and the superconducting leads can be, especially in small devices. They have found that the critical current in a square TES depends exponentially on the side length and on $T^{1/2}$. This behavior can be explained by considering the TES to be a weak link between the superconducting leads (Sadleir et al., 2010). The bilayer is connected at opposite ends by leads with critical temperature much higher than the bilayer T_c. These leads induce superconductivity longitudinally in the bilayer via the proximity effect. That is, the superconducting order parameter ψ in the bilayer is enhanced near the high T_c leads (Sadleir et al., 2011). Sadleir et al. (2010) use Ginzburg-Landau theory to derive that the critical current in the bilayer is described by $I_c \propto e^{-L/\xi}$, where L is the side length of the TES and ξ is the temperature-dependent coherence length. Consequently, the transition temperature of the TES depends on the current, and at constant current it scales with L^{-2}. Sadleir et al. (2010) observed the exponential temperature dependence of I_c and the L^{-2} dependence of T_c in TESs with side lengths ranging from 8 μm up to 290 μm (1450 times the normal-state mean-free path for the bilayer).

One attractive aspect of the modeling the TES as a weak link is that it is possible to incorporate the effects of added normal metal features. In contrast to the behavior near the leads, superconductivity is suppressed in close proximity to normal metal features, known as the lateral inverse proximity effect (Buzdin, 2005). The normal metal reduces the order parameter, which causes the transition to shift to lower temperatures, but with little to no change observed in the width of the transition (Sadleir et al., 2011).

Sadleir et al. (2010) also found that the critical current showed Frauenhofer-like oscillations with applied magnetic field. Similar behavior is observed in Josephson junctions, which further supports the weak link interpretation. The periodicity and width of the oscillations depend on the size and the current density distribution of the junction. Sadleir et al. (2011) observed that in a device with normal metal banks parallel to the direction of current flow, the pattern of oscillations was consistent with the normal metal suppressing the current density in the device near the edges, growing to a maximum in the middle. An important consequence of the critical current varying with applied field is oscillation in the value of α and β (both of which are related to I_c). Smith et al. (2013) measured α and β as a function of both bias point (R/R$_n$) and applied magnetic field. They found that α and β appear to be correlated with one another, and that both parameters showed oscillations with applied field as expected from the weak link model. This result implies that for any device there should be an applied field and bias point where the performance of the TES is optimized.

To model the resistive transition Kozorezov et al. (2011) applied the resistively shunted junction (RSJ) model, originally developed to address the behavior of Josephson junctions and other weak links. In the RSJ model, the TES is represented by a two-element circuit consisting of a Josephson junction carrying the supercurrent and an Ohmic resistance carrying the quasiparticle current. Though it is conceptually similar to the two-fluid model in that it divides the current into normal and superconducting branches, the resistance comes from the interaction of the superconducting leads with the TES, rather than from the TES itself via phase slips. The RSJ model is one-dimensional and assumes that the current-phase relation is sinusoidal and the current density in the device is uniform. Though these assumptions are unlikely to hold in devices with complex geometry like the TES (we saw above how the current density in a TES with normal metal banks is suppressed at the edges), they make the calculations tractable. Smith et al. (2013) use Ohm's law with a correction factor suggested by Ambegaokar & Halperin (1969) to write the resistance of a TES in the RSJ model as:

$$R(T,I,B) = R_n\sqrt{1-\left(\frac{I_c(T,B)}{I}\right)^2} \tag{3.5}$$

This expression is valid in the limit where the Josephson coupling energy is much bigger than the thermal energy, and for $I/I_c > 1$. When $I/I_c < 1$, the device is superconducting. For a junction, the critical current depends on the size of the device, the current density, and the magnetic field. The magnetic field itself can also be treated as a function of current and temperature to account for the effects of self-fielding. Equation 3.5 is differentiated to obtain expressions for α and β. Using this model, Smith et al. are able to qualitatively reproduce the oscillation of I_c, α, and β with applied field, and the changes in α and β with bias point (R/R_n). The model also predicts jumps and discontinuities in α and β with applied field and resistance, again in qualitative agreement with observations in real devices. However, the calculated values of α and β were found to disagree with measurements by about an order of magnitude. This is probably not surprising given that the model is simplified and one-dimensional, and does not include any non-equilibrium superconductivity effects.

Bennett et al. (2013) compared predictions for α and β in the RSJ and two-fluid models to data from TESs with a range of sizes measured over a variety of bias points. Looking at β as a function of bias point, they found that the RSJ model best describes small devices ($L \sim 50\mu$m or less) at bias points in the lower half of the transition, whereas larger devices are better described by the two-fluid model. They argue that this shows that as the bias point and therefore resistance increases, effects within the TES dominate the weak link effect in all but the smallest devices. It is clear that neither picture can be fully correct, since both models include simplified physics and cannot account for properties of the TES known to affect their behavior such as film geometry in the two-fluid model, or non-uniform current density in the RSJ model.

Although the RSJ model and two-fluid models dominate the discussion at the moment, a number of other models have been proposed to explain TES resistance. For example, Fraser (2004) uses Kosterlitz-Thouless-Berezinsky (KTB) theory to model the TES resistance as a consequence of the creation of vortex cores, cylinders of normal material with a radius equal to the Ginzburg-Landau coherence length. This model has the advantage that it can incorporate the effects of an external field, but it is only expected to be valid low in the transition. Lindeman et al. (2006) proposed the percolation model, in which the TES is modeled as a network of resistors that randomly fluctuate between superconducting and normal states. This model can incorporate added normal metal features, and it has been shown to make some correct predictions about TES noise. However, Sadleir et al. (2011) argue that it predicts a change in transition width with the addition of normal metal features that contradicts experimental observations.

Though current models are clearly oversimplified, a great deal of insight has been gained from comparing them to data from real TES devices. The experimental evidence shows that weak link effects are real, and any complete model must account for both this behavior and effects within the TES itself, which become more important as the resistance increases through the transition. Both the RSJ model and the two-fluid model have had success describing observations, such as oscillations in the critical current, and the bias point dependence of α and β. However, the models are thus far more succesful at being descriptive, rather than being able to correctly predict the transition shape and field dependence from geometry alone. For the near future, at least, experimental optimization is still needed to guide device design while the models improve.

3.3 Noise in transition-edge sensors

The conventional model for noise in a thermistor microcalorimeter, outlined in Section 2.3, does a good job describing the noise found in the high impedance sensors made from germanium or doped silicon that dominated the first few decades of thermal microcalorimetry. This model accounts for thermal fluctuation noise (TFN) between the sensor and the thermal bath, Johnson noise in both the sensor and the load resistor, and any amplifier noise added by the readout. Once low-noise SQUID amplifiers became available and amplifier noise no longer dominated the noise spectra of TESs, groups began to observe much higher levels of noise than were predicted by the conventional model. This was deemed "excess noise" and was often found to be several times greater than the Johnson noise at high frequencies, but fell below the TFN for frequencies below the knee in the noise spectrum caused by the thermal time constant (Hoevers et al., 2000a; Lindeman et al., 2002; Tiest et al., 2002; Luukanen et al., 2003). They also found that the excess noise contribution changed with bias point: that is, with the resistance of the TES.

Early on, several sources were hypothesized to explain this noise, including internal thermal fluctuations (ITFN) due to the finite thermal conductance of the TES itself (Gildemeister et al., 1999; Hoevers et al., 2000b) and fluctuations in the superconducting order parameter (Luukanen et al., 2003). Simultaneously, groups began to experimentally investigate the relationship between the amount of excess noise and the TES geometry. Ullom et al. (2004) measured excess noise in a series of identically sized Mo/Cu membrane-isolated TESs with varying patterns of normal metal banks and bars deposited on top of the bilayers. The amount of excess noise varied between designs by up to a factor of ten. The amount of excess noise was lowest in devices with normal metal bars placed perpendicular to the direction of current flow. Most significantly, they found that the amount of excess noise was strongly correlated with α, suggesting that the geometry of the normal metal features was only important insofar as it reduced α. Ullom et al. also tried applying an external magnetic field to their devices, and found that the field simultaneously reduced excess noise and α (see Fig. 3.3). Staguhn et al. (2004) found similar results in Mo/Au TESs. They compared TESs with normal metal bars parallel and perpendicular to the flow of current, and found the excess noise was lowest in the design with perpendicular bars. They pointed out that if the excess noise was caused by

ITFN, the addition of the normal metal bars may be confining regions that were driven normal by the bias current, thereby preventing them from interacting and reducing the noise. Furthermore, as Hoevers et al. (2000b) showed, the amount of excess noise due to ITFN should be proportional to the current through the TES and α, so ITFN could potentially explain the correlation observed between excess noise and α.

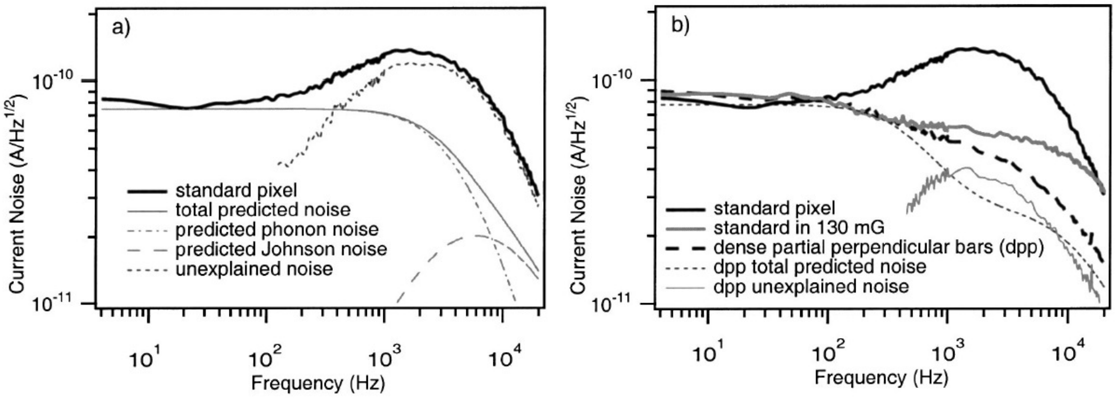

Figure 3.3: Measurements of current noise from Ullom et al. (2004) showing excess noise. The devices are 400 μm × 400 μm Mo/Cu TESs. Left: The "standard pixel" is bare TES with no additional normal metal stripes, biased at 60% R_N and B=0. The predicted noise spectrum does not include contributions from non-linear Johnson noise, or any other "excess" noise. Right: The unexplained noise contribution is suppressed in the presence of a magnetic field ("standard in 130 mG"), and in a pixel with added normal metal bars ("dense partial perpendicular bars (dpp)"), consistent with the finding that reducing α reduces the excess noise.

However, the observed excess noise was not totally consistent with ITFN in all observations, suggesting more than one culprit (for example, see Tiest et al. (2002); Kinnunen et al. (2008)). Rather than looking for complex effects related to the superconductivity in the TES, Irwin (2006) extended the calculations for Johnson noise in a microcalorimeter to account for thermometer nonlinearity (nonzero β) and operation out of equilibrium (when the thermometer temperature does not equal the bath temperature). Irwin showed that in this case, the power spectral density of the current noise is given by:

$$i_n^2 = \frac{4k_B T_0}{R_0}(1 + 2\beta) \tag{3.6}$$

where T_0 and R_0 are the bias point temperature and resistance of the sensor, respectively. So, some of the observed "excess" noise was simply due to this nonlinear Johnson noise term that was not accounted for in the original theory. Jethava et al. (2009) measured the noise spectra of a variety of devices with varying α, this time with the $(1 + 2\beta)$ term in their noise model, and quantified the remaining excess noise. They found that for devices with $\alpha < 100$ the addition of the nonlinear Johnson noise term accounted for all the observed noise. However, for devices with $\alpha > 100$, they again observed excess noise. The amount of excess was correlated with α, but not β. They also observed that α and β were correlated, but β was not an accurate predictor of α (nor the amount of excess noise). The finding that the addition of normal metal features could be used to suppress α and therefore the magnitude of the excess noise has led to their widespread use in TES designs. However, since reducing α comes at the cost of reducing the theoretical best energy resolution, identifying and understanding the sources of the excess noise (above the nonlinear Johnson noise) and then hopefully finding ways to mitigate them is important for continuing TES development.

As we learned in Section 2.3, thermodynamic fluctuations are an unavoidable consequence of statistical fluctuations of power flow across a thermal conductance. This might occur within the TES itself, or between the TES and an attached absorber. These sources are often collectively referred to as "internal thermal fluctuation noise" to differentiate them from the fluctuation noise between the system and the heat bath. As an example, the finite internal thermal conductance of the TES (G_{TES}) causes temperature fluctuations within the device, which we then measure as current noise at the output. Assuming the TES is close to isothermal, we know from Equation 2.11 that the power fluctuations are given by $p_{ITFN}^2 = 4k_BT_0^2G_{TES}$, which results in temperature fluctuation given by $dT_{TES} = p_{ITFN}/G_{TES}$ up to a cutoff frequency $f_{TES} = G_{TES}/2\pi C_{TES}$. Hoevers et al. (2000b) show that for frequencies above $f_e = (1 + BL)/(2\pi\tau_0)$, the current noise due to ITFN in the TES can be written:

$$i_{ITFN} = dT_{TES}(\alpha I_{bias}/2T_0)(1 + B) \tag{3.7}$$

where $B \equiv (R - R_{SH})/(R + R_{SH})$ and $L \equiv \alpha P/GT_0$. So, the current noise due to ITFN should be directly proportional to α and the bias current. Although in this case we are only considering the ITFN to be a result of heat transfer within the TES, devices with attached absorbers have been successfully modeled with an additional source of fluctuation noise due to the exchange of heat with the absorber Kinnunen et al. (2012). In either case, the ITFN is the result of heat exchange between superconducting and normal regions of the device. Even in a bare TES, this is presumably not a simple matter of two cleanly separated regions connected by a single conductance, so G_{TES} is really some average over a distributed system of conductances.

A number of authors have generalized the expressions for thermal fluctuation noise in TES detectors using what is referred to as a “block model.” Each block represents a heat capacity that can be connected to one or more other heat capacities in the device, and each connection has a separate thermal conductance. Then, every thermal conductance in the system is a source of thermal fluctuation noise. For an example of a block model including decoupling of the absorber and thermometer, see Galeazzi & McCammon (2003). More recently, a more general description of two and three block models is given by

Maasilta (2012), including equations for current noise. These more general models with multiple heat capacities and thermal conductances have proven valuable for fitting and interpreting TES noise. Goldie et al. (2009) used such a model to fit data for bare (no attached absorber) Mo/Cu TESs that included the thermal fluctuations between the TES and the bath (TFN), within the TES, and between the heat capacity of the TES and the heat capacity of the SiN membrane. To their surprise, they found that the nitride membrane had a heat capacity well in excess of Debye-model predictions, and that its thermal fluctuation noise contribution was the dominant source of excess noise in some of their devices. Kinnunen et al. (2012) also found that a three block model was needed to model their Ti/Au TES devices, and they too identified heat exchange with the membrane (with an unexpectedly large membrane heat capacity) as the likely source of the noise that could not be attributed to the TES-to-bath contribution or to internal fluctuations within the TES.

The most obvious and easiest course of action for reducing ITFN is to reduce α, which has the unfortunate consequence of reducing the theoretical best energy resolution one can achieve. However, in many cases the use of normal metal features to limit α to less than 100, where one generally only needs to contend with the nonlinear Johnson noise, has proven to be a favorable compromise. In general, excess TFN can be reduced by keeping thermal conductances of the TES and between the TES and the absorber as high as possible. It is also worth noting, as Kinnunen et al. (2012) point out, that in the case where these conductances are large it is possible that the cutoff frequency may be higher than the cutoff for the readout, causing it to look like white noise, and making it more difficult to correctly identify. Last, the ITFN is directly proportional to the bias current. However, for a given device reducing the bias current is not necessarily helpful, as it tends to be inversely correlated with α. The work by Goldie et al. and Kinnunen et al. also suggests that thinning or minimizing the size of the nitride island may be beneficial, but more work is probably necessary to fully understand the role of the membrane.

Alongside the evolving understanding of internal thermal fluctuations, a variety of alternative sources for excess noise have been proposed that are related to the superconductivity in the TES. One possibility is phase-slip shot noise caused by the current-induced motion of vortices across a superconducting film, sometimes referred to as flux-flow noise after an analagous effect that occurs in type-II superconductors. This source was proposed by Voss et al. (1980) to explain observations of current noise in very high resistivity thin films of tin and aluminum, and shortly thereafter Knoedler (1983) proposed that it could contribute to noise in superconducting bolometers. However, in the working regime of most modern TES devices, the contribution from this source is probably negligible, except perhaps when working at very low resistance and high current (Galeazzi, 2011). Another proposed noise mechanism is the fluctuation in the superconducting order parameter from the random creation and dissociation of Cooper pairs. This effect had been known for several decades (Aslamazov & Larkin, 1968) and a calculation for the amount of noise it would produce had been available for some time (Nagaev, 1991) when Luukanen et al. (2003) applied it to excess noise they observed in a Ti/Au TES. Then Seidel & Beloborodov (2004) provided calculations for the noise spectral density due to pair fluctuations in the general TES case, showing that in most cases this noise was expected to be much smaller than the TES Johnson noise. While flux-flow and fluctuation superconductivity are probably the best studied examples of superconductivity-related noise sources in TES, new ideas are still being proposed (see, for example, Kozorezov et al. (2012) on noise in the RSJ model, or Lindeman et al. (2006) on noise in the percolation model).

As yet there is not a great deal of experimental evidence that any of the superconductivity-related effects dominate the noise spectra in any real devices. However, for some TESs, fitting nonlinear Johnson noise and ITFN models is still inadequate to describe all of the observed noise. A full accounting of sources of excess noise in TESs and an understanding of ways to mitigate their effects remains an ongoing investigation.

Chapter 4

Detector design

4.1 Motivation for design and materials

The constraints on materials and design for our devices come from the available equipment (cryostat and electronic readout) and the environment and duration of a sounding rocket flight. As outlined in section 1.2, these are:

- better than 2 eV FWHM energy resolution from 50-500 eV
- 890 μm × 890 μm collecting area with near unity efficiency from 50-500 eV
- 50 mK base temperature

All the TES devices tested for this work were fabricated at Goddard Space Flight Center's Device Design Laboratory (DDL). The DDL has considerable expertise working with Mo/Au bilayers, which have been the material of choice for the GSFC group's X-ray TESs for over a decade. Therefore, we will start with a Mo/Au bilayer for our design. The fabrication process typically starts with a 50 nm layer of Mo, then 200-300 nm of Au is applied to achieve a T_c between 70 - 125 mK. The thicker the Au layer relative to the Mo layer, the lower the critical temperature will be. Both molybdenum and gold have relatively large heat capacities, so simply scaling the size of the detector to 890 μm × 890 μm and absorbing the X-rays directly in the TES would result in a device with too much heat capacity. Therefore, we will attach an 890 μm × 890 μm absorber to a much smaller TES.

The basic TES design for this project is adapted from devices used for the Micro-X sounding rocket mission, and is similar to detectors designed for what is currently the Athena satellite project. The Mo/Au bilayer is a 140 μm × 140 μm square. Superconducting Mo leads overlap two opposing edges to allow readout and biasing. Then normal metal (Au) banks are added to the two remaining edges to prevent a superconducting short along the device, and several gold bars are added perpendicular to the direction of current flow to suppress noise (see section 3.3 for details on why this is necessary). An illustration of the device is shown in Figure 4.1.

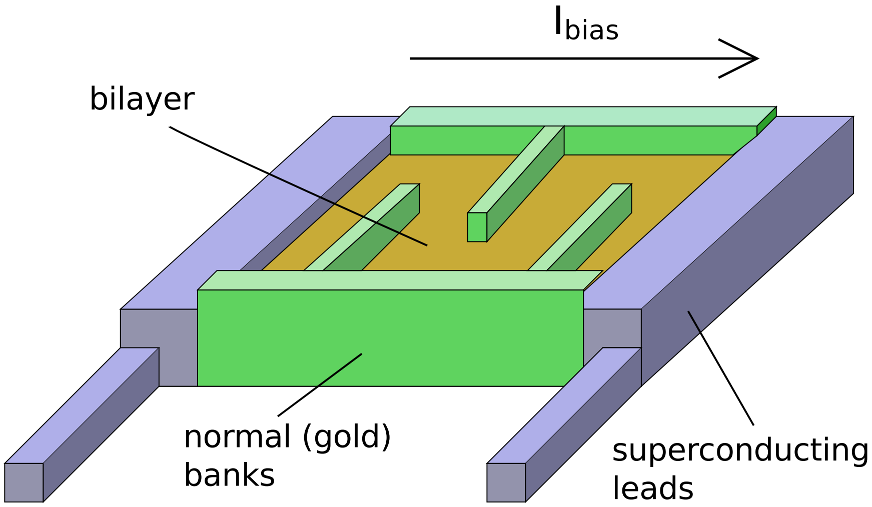

Figure 4.1: Illustration of a bilayer (gold) with superconducting leads (light blue) to carry the bias current, with the direction of current flow indicated by the arrow. Normal metal (green) banks parallel to I_{bias} are added to prevent superconducting shorts along the device. Perpendicular bars reduce α and suppress excess noise.

With the TES design set, the key to achieving the desired performance will be choosing the material for the absorber and controlling the thermal time constants in the device. For the absorber, we'd like to keep the total heat capacity as low as possible. One way to do this, regardless of the material we choose, is to operate the device at a low temperature. As previously established, the bath temperature is set at a minimum of 50 mK. We need to keep the bath temperature well below the TES critical temperature, both to take advantage of self-biasing via Joule power dissipation and to make the TES less sensitive to fluctuations in the bath temperature. Therefore, we will try to make a device with $T_c = 70$ mK.

With an absorber that will be much larger than the thermometer, it is going to be critical to have high lateral thermal conductivity in the absorber. That is, if an X-ray impacts the absorber in a corner, far from the TES, the heat must be transported quickly throughout the device so that the entire system comes to a uniform temperature before some of the heat is carried away by the weak thermal link to the bath. Otherwise, X-rays that strike close to the TES will be measured as having more energy than X-rays that strike farther away. This is called position dependent pulse shape, and it will be discussed in detail in the next chapter. For now, we'll just state qualitatively that the absorber material we choose should have a low heat capacity, but a high lateral thermal conductivity.

Our choices for absorber materials can be roughly lumped into three groups: superconductors, normal metals, and semi-metals that can still be electrodeposited. To efficiently stop X-rays, any absorber we choose must be a high-Z material. Superconducting absorbers are attractive because they have much lower heat capacity than comparably heavy normal metals. Whereas in normal metals the electronic heat capacity decreases linearly with temperature, the electronic heat capacity of a superconductor decreases exponentially for $T < T_c$. However, in practice it has proven difficult to produce high quality superconducting absorbers.

The best results have been achieved with high purity bulk tin, which is diced and then epoxied to the TES thermometer. This technique is primarily used for gamma ray detectors where the thick bulk material is necessary to provide stopping power for 100 keV photons. Such a detector has been demonstrated with 27 eV FWHM energy resolution at 103 keV (Horansky et al., 2007). However, despite the high performance of this device, the authors found the response showed an additional long athermal decay time constant, which contained 31% of the total energy of the pulse. This limits the counting rate at which good energy resolution can be achieved. This effect has been observed by multiple groups in bulk tin. Initially, it was speculated that this was due to unexpected long-lived quasiparticle states or an increase in heat capacity due to defects or contaminants (Horansky et al., 2007). More recently, however, it has been shown that most of the effect can be attributed to the epoxy joint that thermally connects the absorber and the thermometer (Hatakeyama et al., 2013; Horansky et al., 2009). Attempts have been made to extend these results to lower energy devices by thinning the tin absorber, which means electrodepositing films rather than using bulk material. Thus far, it has proven very difficult to deposit high quality tin films, as they tend to show unexpectedly high heat capacity, sensitivity to magnetic fields (Galeazzi et al., 2006) and, once again, long athermal time constants that degrade the resolution (Ishisaki et al., 2004). In this case, there is no epoxy joint between the absorber and thermometer, so long-lived quasiparticle states or lattice defects may be to blame for this behavior.

In search of a high-Z, low-C alternative to superconducting absorbers, many groups have used the semi-metal bismuth. Bismuth films can be evaporated or electroplated, which is important when considering the possibility of future kilopixel scale arrays, and this also avoids the epoxy joint issues experienced with bulk tin absorbers. However, it has proven challenging to reliably fabricate bismuth films with close to bulk properties, and bismuth's low thermal conductivity has proven problematic. Early attempts to evaporate bismuth absorbers found excess heat capacity and poor lateral thermal conductivity that degraded the detector response (Yoshino et al., 2006; Vaillancourt et al., 2004). Adding one or more layers of normal metal (Cu or Au) to bismuth absorbers improved the conductivity, although at the expense of added heat capacity (Sadleir et al., 2006). Additionally, bismuth can diffuse and form intermetallic structures at interfaces with normal metal layers, which reduces the effectiveness of the added normal metal. Later, GSFC developed a process for electroplating gold/bismuth absorbers, which improved their performance (Brown et al., 2008). However, interdiffusion remains a problem, both for reproducibility and degradation of the thermal properties of the normal metal conducting layer (Eckart et al., 2009).

Given these complications with superconductors and semi-metals, we would like to be able to use a normal metal for the absorber. Gold is the obvious choice, since compared to other metals with good thermal conductivity like copper or silver, it has higher Z and therefore will require a thinner layer. The requirement for the surface area of the absorber (890 μm × 890 μm) was set assuming a near-unity quantum efficiency. Poor absorption efficiency would simply need to be offset by increasing the area, thereby increasing the heat capacity, so we will choose the thinnest layer of gold that provides acceptable efficiency. We chose a 200 nm layer of gold, which is roughly 99% efficient from 0 - 500 eV, except for an anomalous feature at around 160 eV where the absorption efficiency dips to about 91% (see Figure 4.2). Since the transmission is an exponential function of the path length and the energy resolution increases as $\sqrt{C}$, increasing the thickness of the gold to get slightly higher efficiency at 160 eV is a losing battle.

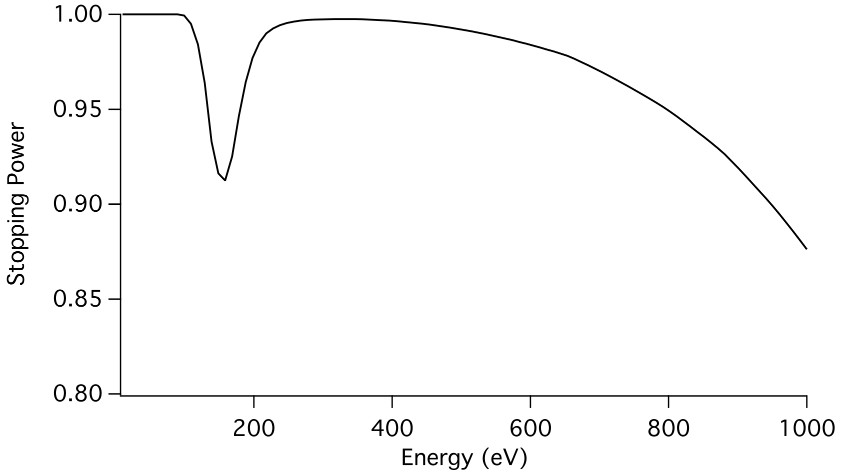

Figure 4.2: The absorption efficiency of 200 nm gold layer for soft X-rays (Henke et al., 1993).

The final element of the detector design is the weak thermal link to the bath. This is provided by the silicon nitride membrane between the bilayer and the silicon wafer. To further reduce the membrane thermal conductivity and also prevent pixel-to-pixel thermal crosstalk, the silicon can be etched away from the back side of the wafer, leaving free-standing nitride. In this case, the conductivity between the membrane and the bath will be determined by the the phonon-emitting perimeter of the device and the perimeter of the membrane. If large areas of the device are in contact with the membrane, the conductivity will tend to be high. However, we can reduce this conductivity by etching slots into (perforating) the membrane near the edges.

Up to this point, we have not discussed how the absorber will be constructed, nor how it will be thermally connected to the TES. We have, however, determined that it is important that the absorber and thermometer reach an equilibrium on a time scale that is short compared to the thermal time constant for decay back to the bath temperature. Therefore, the conductivity between the absorber and the TES should be much larger than the conductivity between the TES and the bath. Since our gold absorber has a high internal thermal conductance, we can overlap part of the gold absorber with the TES to make a strong thermal link. Also, the heat flow between the absorber and the membrane must be as small as possible, so we would like to minimize the amount of phonon-emitting perimeter of the absorber that is in contact with the membrane.

GSFC has developed a method for fabricating absorbers in which only a small patch of the absorber contacts the TES and the rest is cantilevered above the sensor, leaving a vacuum gap between absorber and substrate (Bandler et al., 2008). This design has a number of advantages. The limited contact patch between the absorber and the TES minimizes interaction, which can alter the properties of the TES transition. The absorber can be made larger than the sensor, so it can be used to cover wiring and increase the focal plane filling fraction. And,most importantly for our purposes, if the absorber is suspended above the sensor and membrane, the only thermal connection between the absorber and the bath will be via the TES. Unfortunately, gold is soft, so an 890 μm × 890 μm × 0.2 μm absorber would not be self-supporting. We will need to add additional support "stems" that sit on the nitride membrane and keep the absorber from drooping or breaking. To minimize the heat lost to the membrane, the total footprint of the stems on the membrane should be small. Illustrations of the full design, showing the membrane, sensor, and absorber geometry are shown in Figures 4.4 and 4.3.

4.2 Predicting detector performance

The theoretical noise, energy resolution, and pulse shape for our design were calculated using the μCal code, developed at GSFC, which uses the matrix method outlined by Figueroa-Feliciano (2001) to calculate the noise spectrum and responsivity. This model includes the effects of the bias circuit and SQUID readout, the electrical and thermal

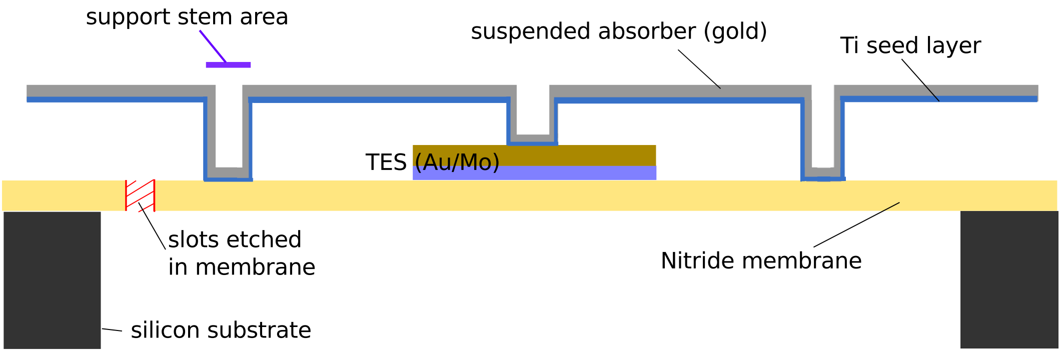

Figure 4.3: A cross sectional illustration of the pixel geometry. The 890 μm × 890 μm × 0.2 μm gold absorber (gray, with titanium seed layer shown in blue) is thermally connected to the TES and is mechanically supported by stems that sit on the nitride membrane (yellow) and bilayer (gold/purple). The thermal conductivity between the membrane and the bath is reduced by etching slots (highlighted in red) into the perimeter of the membrane. Note that the drawing is not to scale. For example, the gap between absorber and membrane is only 2-4 μm, and the lateral footprint of the support stems is 7-20 μm.

properties of the TES, and treats the absorber as a separate thermal system from the sensor. The model requires a long list of input parameters, which can be found in Appendix A.1 for the pixel depicted in Figure 4.4. In this section, I'll highlight some of the most important parameters and how they were determined, and show the results of the modeling.

The heat capacity of the device is dominated by the gold absorber. In a normal metal, the specific heat is given by the sum of the lattice and electron heat capacities: $C = C_{latt.} + C_e = \beta T^3 + \gamma_e T$. At very low temperatures, the electronic term dominates and we can ignore the lattice contribution. For gold, the electronic heat capacity coefficient $\gamma_e = 0.729$ mJ mol^{-1} K^{-2} (Kittel, 1996). We multiply by the volume of the absorber (890 μm × 890 μm × 0.2 μm) and divide by the molar volume of gold (10.17 cm^3/mole) to find that total heat capacity of the absorber at 100 mK is 1.1×10^{-12} J/K.

Determining the heat capacity of the TES is less straightforward. According to BCS theory, the heat capacity of a superconductor at its transition temperature is 2.43 times

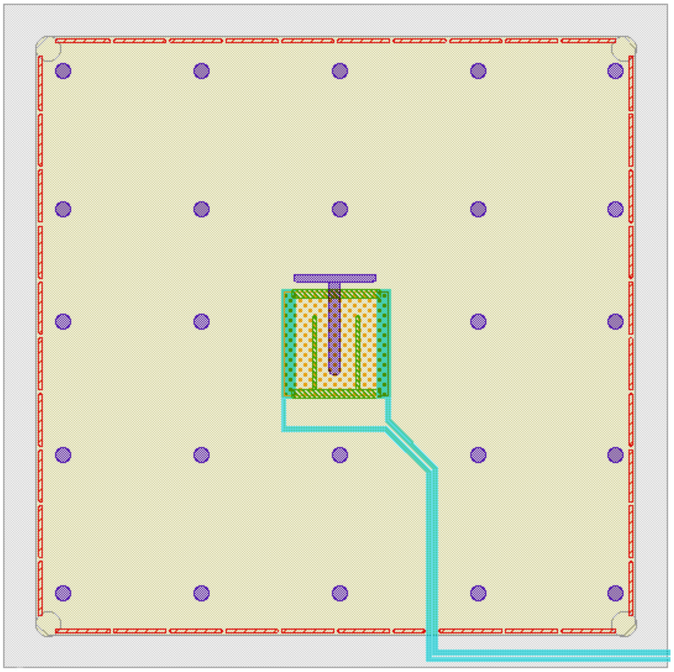

Figure 4.4: Face on illustration of the pixel design. The 890 μm × 890 μm × 0.2 μm gold absorber (gray, shown semi-transparent since it obscures the TES) is thermally connected to the TES via a T-shaped support stem (footprint highlighted in purple), and is mechanically supported by 24 additional 20 μm diameter stems that sit on the nitride membrane (yellow). The thermal conductivity between the membrane and the bath is reduced by etching trenches (red) into the perimeter of the membrane. Drawing is to scale.

larger than its normal metal value. Since the TES is operated within its superconducting transition at $R < R_{normal}$ its heat capacity may be less than $2.43C$ (see, for example, Lindeman et al. (2008)). The only way to know exactly what the heat capacity is for a given bias point would be to measure it. In our case, the volume of the TES is about 4% of the absorber volume, so any error in calculating the expected resolution due to uncertainty about C_{TES} will be small. For modeling purposes, we can take $2.43C$ as an upper limit. The TES is 140 μm × 140 μm, and will be made up of a 50 nm layer of molybdenum and approximately 250 nm of gold. For Mo, $\gamma_e = 2.0$ mJ mol^{-1} K^{-2} and the molar volume is 9.346 cm^3/mole (Kittel, 1996). Therefore, the heat capacity of the bilayer at 100 mK (when it is fully normal) is 5.08×10^{-14} J/K.

Next, we will need to estimate the thermal conductivity between the sensor and the bath, which is provided by the silicon nitride membrane. In thin membranes at low temperatures (< 4 K for a 1 μm thick membrane), the phonon mean free path can exceed the thickness of the membrane and surface scattering effects become important. The conductance of the membrane can be written $G = 4\sigma AT^3\xi$. The Stefan-Boltzmann constant $\sigma = 15.7$ mW cm^{-2} K^{-4} (this is a material specific result obtained using measurements of SiN membranes), and A is the cross sectional area perpendicular to the heat flow (Holmes et al., 1998). If the surface scattering were perfectly specular, than the factor $\xi = 1$. When the scattering is partially diffuse $\xi < 1$. Holmes et al. (1998) found that in general for membranes of micron-scale thickness the value of ξ at temperatures as low as 100 mK is always greater than the Casimir limit (purely diffuse scattering, where a phonon striking the surface has an equal probability of scattering to any direction in the half space), but less than 1. Furthermore, in highly perforated membranes the measured conductivity is often much lower than expected based on the reduction in cross sectional area, and the temperature dependence is slightly weaker than the expected T^3 for insulators [see, for example, Mauskopf et al. (1997); Leivo & Pekola (1998)].

As an alternative method to estimate G for highly perforated membranes, we can use a measurement of the conductivity from a device GSFC has made in the past, and scale that result based on the product of the fraction of the membrane's perimeter that remains after perforation and the perimeter of all the phonon emitting areas that are in contact with the membrane (including the TES plus any additional absorber support stems). The total phonon emitting perimeter times the fraction of remaining membrane perimeter has been found to be a more reliable predictor of the thermal conductance than the geometry of the bridges formed by etching the membrane in situations where surface scattering dominates, since surface roughness and contamination affect the scattering (Stahle et al., 2002; Figueroa-Feliciano, 2001). In Eckart et al. (2009), the authors found that a device with several large support stems and an 84% perforated membrane had $G = 225$ pW/K. A smaller device with 4× less phonon emitting perimeter but no membrane perforations had the same thermal conductivity. We are interested in determining what pattern and density of support stems is necessary to reliably yield thin absorbers, so we will test pixels with a variety of stem patterns, and consequently a variety of conductivities. For the example design shown in Figure 4.4, which has twenty-four 20 μm diameter round support posts plus a T-stem to attach the absorber to the thermometer and a 91.7% perforated membrane, the expected conductivity based on this scaling argument is $G = 110$ pW/K.

The detector response depends on the shape of the transition, so we will need estimates of the two partial derivatives of the temperature and current dependent resistance, α and β. Studies have found that α and β are strongly correlated to one another, to the current through the device, and to the TES critical current (Smith et al., 2008). Thanks to this complex behavior, there is no practical way to accurately predict α and β based on the materials or geometry of the device. Instead, we'll make estimates based on results from previous devices, since the TES we will use has the same geometry as sensors GSFC has previously fabricated for the Micro-X and Athena missions. These sensors were observed to have $\alpha \approx 75$ for the Athena devices, and $\alpha \approx 35 - 55$ for Micro-X (Eckart et al., 2009). In the Micro-X devices, $\beta \approx 0.45 - 1.4$. We can use this to get a rough idea of what we might expect to see in our devices, keeping in mind that those detectors had twice the thermal conductivity that our devices are designed to have, so consequently the current through our devices will be proportionally smaller.

Finally, we can put everything together and simulate the expected pulse shape, noise spectrum, and energy resolution for a range of reasonable α and β to get an idea of how our design will perform. We will assume that the device has a critical temperature of 70 mK and the bath is held at 50 mK. A full list of the input parameters for the simulation, including the bias circuit parameters such as SQUID noise and shunt resistance, can be found in Appendix A.1. We are not yet taking into account the affect of finite thermal diffusion time in the absorber, so the temperature change in the absorber is considered to be instantaneous. The thermal conductivity of the nitride membrane strongly affects the decay time constant of the pulse, as shown in Fig. 4.5. The predicted noise spectrum is shown in Figure 4.6. The only source of "excess" noise accounted for by the model is the nonlinear Johnson noise component, which depends on the value of β. Finally, the predicted energy resolution as a function of α and β is shown in 4.7.

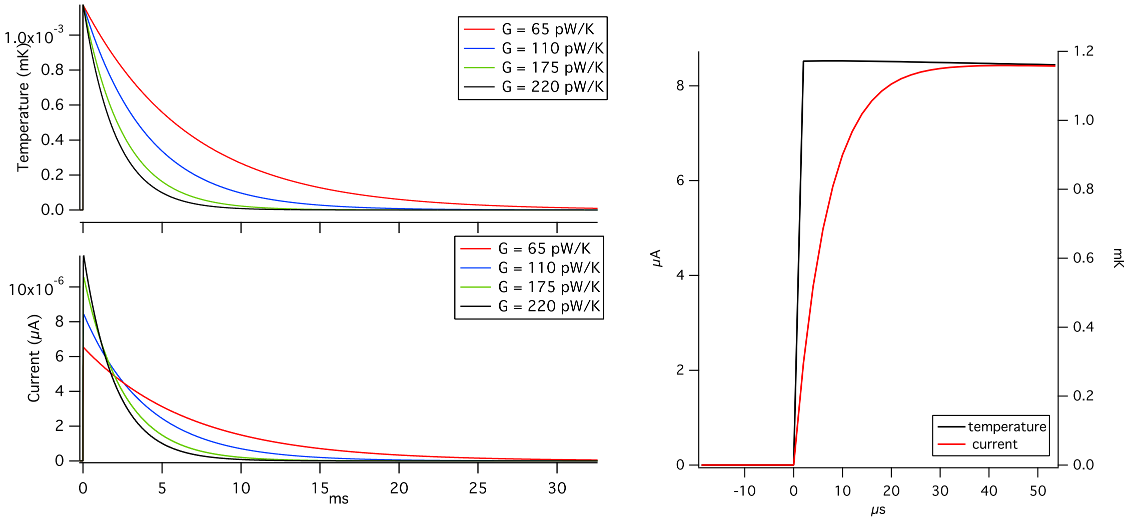

Figure 4.5: Left: Simulated pulse shape in current and temperature for a variety of values of G_{bath}. Incident X-ray energy is 6 keV. For all cases, detector is assumed to be biased at 15% R$_{normal}$ with α = 55 and β = 1.25. Right: Expanded leading edge of simulated pulse in current and temperature for G_{bath} = 110 pW/K, showing the rise. This simulation assumes instantaneous thermalization in the absorber and a very large conductivity between the absorber and TES ($G_{abs-tes}(0.1K)$ = 0.5 μW/K), so when the X-ray is absorbed at time t = 0, the absorber and TES almost immediately come to equilibrium. In the current pulse, this sharp rise is low pass filtered by the L/R time constant determined by the SQUID's input inductance and the resistances of the TES and shunt.

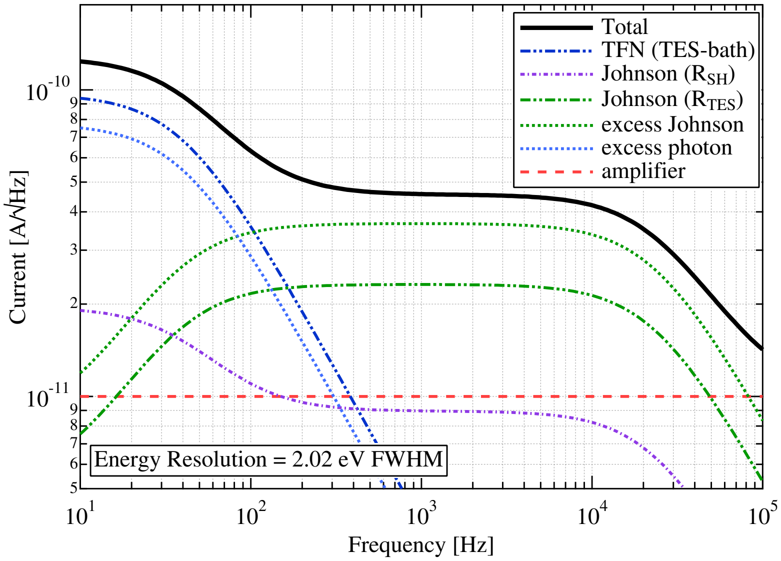

Figure 4.6: Predicted noise spectrum for a detector biased at 15% R_{normal} with $\alpha = 55$ and $\beta = 1.25$. The conductance $G_{bath} = 110$ pW/K. The only source of “excess” noise accounted for by the model is the nonlinear Johnson noise component, which depends on the value of β

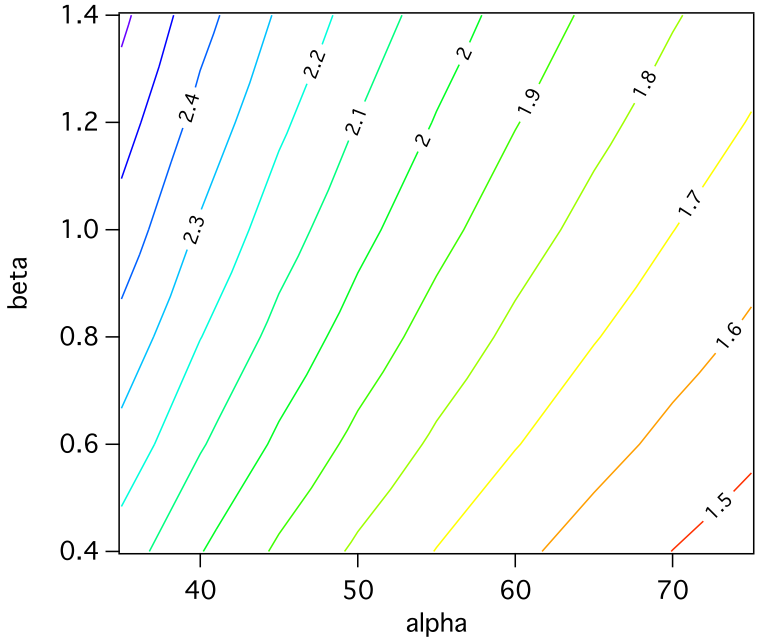

Figure 4.7: Contours of constant energy resolution (in eV FWHM) for a range of α and β. Pixel is biased at 15% R_n with $G_{bath} = 110$ pW/K.

4.3 Experiment design for first devices

The arrays of designs for the first wafer of devices (dubbed the “MXW” wafer) were laid out with two goals in mind. First, it was not known if it would be possible to yield 200 nm thick self-supporting cantilevered gold absorbers. So, the test wafer included a variety of designs such that we were guaranteed something would yield in all but the very worst-case scenario. Then, we needed to be able to assess the validity of all of the estimates that went into the device design. We wanted to verify that the heat capacity of the devices came out close to predictions, to see that the scaling relation for the nitride membrane thermal conductivity was valid, and to see what sort of α values we were going to get. We also wanted to test a variety of different support stem configurations, since there would be to be a tradeoff between mechanical stability and low thermal conductivity, and this has consequences for the severity of the effects of finite diffusion time in the absorber. And if possible, we’d like to improve the resolution by optimizing the TES design, so we wanted to include some devices where we changed the TES geometry to see if we could produce a higher resolution device.

The DDL has some experience working with thin gold cantilevered absorbers. They have made several wafers using the Micro-X mask set with 0.6 μm thick electroplated gold absorbers. The largest area absorbers on this mask are 590 μm × 590 μm. These absorbers showed wrinkling near the support stems and signs of curling at the edges, but the absorbers were continuous and no shorts were found to the substrate or TES (Eckart et al., 2013). However, past experiments with thinner layers have indicated that the wrinkling near the stems could result in breakage.

As an alternative to the cantilevered absorbers, I designed devices where the absorber was deposited directly onto the nitride membrane (no vacuum gap) next to the TES and was thermally connected by an overlapping "finger" of gold. GSFC had considered a design like this in the past (Figueroa-Feliciano et al., 2008), but devices were never fabricated. Although this design avoids some of the fabrication issues anticipated for the self-supporting suspended absorbers, it does have several drawbacks. One disadvantage is that without the overhanging absorber to cover the silicon frame and wiring, the focal plane filling factor is significantly reduced. This is tolerable for our experiment, where there are no optics and we are not interested in imaging. Another complication is that without the absorber to cover the TES, there will be significantly more events that are thermalized directly in the sensor. These events may have a different pulse shape (faster rise time), and could be vetoed or processed separately to recover the best energy resolution. Controlling the thermal conductivity to the bath is also a concern as there is a large phonon emitting perimeter in contact with the membrane, so heat loss to the substrate may exacerbate the problem of position dependent pulse shape. Last, I designed the gold finger that thermally connects the absorber and TES to have the same overlap shape and area as a T-stem in the standard design, hoping to minimize its effect on the shape of the transition. However, since the absorber gold in the finger needs to overlap several layers of metal (Mo/Au in the bilayer, plus extra Au in the banks), breakage at this junction was a potential problem. An illustration of this design is shown in Figure 4.8. We refer to this design as the "coplanar" configuration since the TES and absorber lie in the same vertical plane, as opposed to the standard cantilevered or "suspended" absorber designs.

Previous experience testing the all-gold-absorber Micro-X devices also guided this design. We tested devices with 590 μm × 590 μm × 0.7 μm gold absorbers and $T_c \approx 90$ mK. Measurements on two pixels found that their heat capacity was more than double what was calculated based on the absorber thickness. This finding was supported by the measured NEP for the pixels, which ranged from 5-7 eV, compared to 3.5-4 eV as expected.

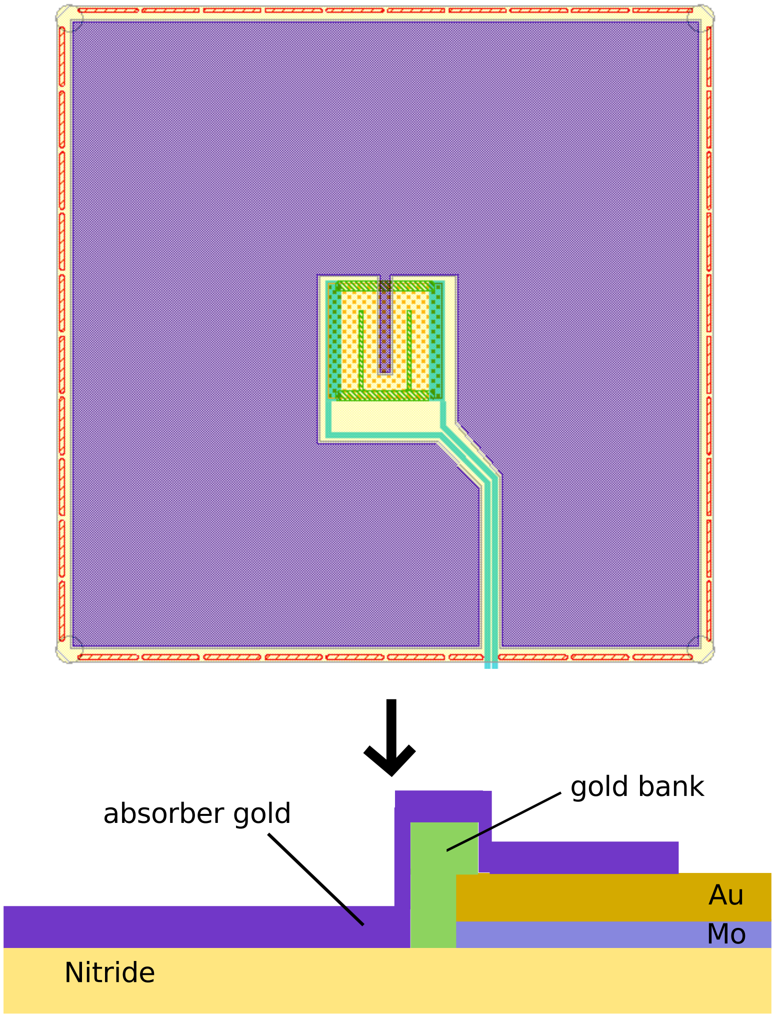

Figure 4.8: Drawing illustrating the coplanar pixel design. The absorber (purple) is deposited directly onto the nitride membrane (yellow). The perimeter of the membrane is 90% perforated (areas marked in red). Top: Face on-view, drawn to scale. Bottom: Simplified drawing to illustrate the thermal connection between the absorber and the TES (drawing not to scale). The black arrow indicates the area where step coverage may be a concern: poor coverage may weaken the thermal connection.

The reason for this large excess heat capacity was not understood. Therefore, the MXW wafer design included three absorbers sized smaller than the 890 μm × 890 μm target device. If we observed excess heat capacity, we would then be able to check whether or not it scaled with the absorber volume. The absorber sizes chosen were 240 μm × 240 μm to facilitate comparison to previous devices created for Athena, and 440 μm × 440 μm and 590 μm × 590 μm to match Micro-X designs.

Finally, another issue that we hoped to address with the MXW wafer was the discrepancy in TES sensitivity between the the Micro-X design versus superficially similar sensors designed for Athena. Measured values of α for the Micro-X detectors have typically been less than 50. Similar sized TESs fabricated earlier for the Athena project also had the same pattern of normal metal banks and noise-suppressing bars, but had α as high as 100 (Bandler et al., 2008). The MXW wafer included two arrays of pixels with 240 μm absorbers with varying absorber attachment stems and superconducting lead geometries to test their effects on the detector sensitivity.

For descriptions of all the pixel designs included on the MXW wafer, along with μCal simulations calculating the predicted NEP and effective decay time constant for each design, refer to Appendix A.2.

Chapter 5

Thermal diffusion in absorbers

5.1 Position dependent pulse shape

Position dependent pulse shape occurs when the time constant for heat diffusion in the absorber results in a change in the pulse rise time depending on where in the absorber a photon is absorbed. If an X-ray impacts near the edge or corner of an absorber that is much larger than the thermometer, the finite time it takes for the heat to diffuse into the TES will lengthen the rise time, and consequently introduce an error into the estimate of pulse height when the pulse is compared to the average pulse shape. In materials with a low diffusion constant, such as bismuth, position dependence can severely degrade the performance of a detector. For example, Hoevers (2006) reported a degradation of $\Delta E \approx 20$ eV for a TES with a 0.1/8 μm Au/Bi absorber that extended 75 μm beyond the thermometer, which increased to $\Delta E \approx 200$ eV for a device with a 200 μm overhang.

There are a number of ways to mitigate the impact of position dependent pulse shape. Of course, choosing a material with good internal thermal conductivity will reduce the diffusion time. For this reason, we would like to be able to use a normal metal with high conductivity (Cu, Ag, Au), and of the available options, gold is both easy to work with and has a high X-ray stopping efficiency. Next, we can decrease the thermal conductivity between the TES and the bath, which will lengthen the fall time of the pulses. This will allow the absorber and TES to equilibrate before heat is lost to the substrate. Finally, since the pulse shape differences occur on time scales that are short compared to the TES-to-bath thermal time constant, we can also reduce the degradation of the energy resolution in the data processing stage by applying a low pass filter to the optimal filter. This essentially means throwing out pulse data beyond a certain cutoff frequency, and therefore not using the entire signal-to-noise content of the pulses. Although this limits the best energy resolution that can be achieved in theory (i.e. in the absence of any pulse shape variation), it at least mitigates the degradation when there is significant position dependent pulse shape (Saab et al., 2007).

Initially, most efforts to make microfabricated absorbers that were larger than the attached TES limited the overhang to 50-200 μm to limit the pulse shape variation (Lindeman et al., 2004; Bandler et al., 2008). More recently, GSFC fabricated 600 μm × 600 μm Bi/Au absorbers coupled to a TES by a T-shaped support stem. These devices showed signs of rise time/pulse height correlation, and position-dependent response (Eckart et al., 2013). Even though we might expect an all-gold absorber to thermalize faster than Bi/Au, our design (presented in the previous chapter) has more than twice as much surface area as the Micro-X devices, and the gold layer is thinner (0.2 μm versus 0.5 μm). And, although our design also couples the absorber to the TES via a T-stem, the Micro-X design places the TES near one corner of the absorber, whereas in this design the TES lies under the center of the absorber. To get an idea of what effect position dependent pulse shape variation might have on our results, we would like to model the thermal diffusion in this new device design.

5.2 Diffusion model and predicted behavior

To simulate the diffusion of heat throughout the absorber as a function of time, we will use a numerical simulation based on the forward time-centered space (FTCS) differencing method. This method was used by Saab et al. (2007) to successfully model diffusion in a Bi/Au absorber coupled to a position sensitive TES device (PoST). The simulation divides the absorber into small discrete volume elements and uses an assumed value for the lateral diffusivity to calculate the temperature change in each element in the absorber and TES as a function of time. Essentially, the FTCS method numerically solves the coupled differential equations that describe the heat transport in the TES and absorber:

$$\begin{aligned}\frac{\partial E_{abs}(x,y,t)}{\partial t} &= D_{abs}\nabla^2 E_{abs}(x,y,t) - \frac{G_{abs-tes}}{C_{abs}}E_{abs}(x,y,t) + \frac{G_{abs-tes}}{C_{abs}}E_{tes}(x,y,t)\\ \frac{\partial E_{tes}(x,y,t)}{\partial t} &= D_{tes}\nabla^2 E_{tes}(x,y,t) + \frac{G_{abs-tes}}{C_{tes}}E_{abs}(x,y,t) - \frac{G_{abs-tes}}{C_{tes}}E_{tes}(x,y,t)\\ &- \frac{G_{tes-b}}{C_{tes}}E_{tes}(x,y,t)\end{aligned} \tag{5.1}$$

E_{abs} and E_{tes} are the energies in a single volume element at a given time. The thermal diffusivity of the absorber and TES are represented by D_{abs} and D_{tes}, respectively, and are assumed to be constant. C_{abs} and C_{tes} are the heat capacities of a single volume element. The thermal conductivity between the absorber and the TES is described by $G_{abs-tes}$, and it is assumed to be nonzero only where the absorber and TES are in direct contact (e.g., the T-stem). The TES also has a thermal conductivity to the bath, described by G_{tes-b}. In fact, if the absorber has additional support stems on the nitride membrane that do not contact the TES, then there will be an additional thermal conductivity between the absorber and the bath. Generally, we have tried to design devices such that the number and size of these support stems are limited, and we can assume that the TES dominates the thermal conductivity to the bath. However, in the case where the additional support stems are large, their contribution to the bath conductivity is probably significant. The design modeled in the previous chapter (see 4.4) has many support stems, but they are small (20 μm diameter) relative to the TES (140 μm × 140 μm), so to simplify the calculations and the interpretation of the results we will neglect the absorber-to-bath thermal conductivity for the time being. Although both thermal conductivity and heat capacity are functions of temperature, since the temperature change due to an X-ray absorption event is typically small, they are treated as constant for simplicity. Last, in the constant-voltage biased TES, the pulse fall time is shortened by electrothermal feedback. We account for this effect by increasing the value of G_{tes-b} to the effective value that produces the correct pulse fall time with the addition of feedback.

To predict the degradation due to position dependence in our design, we need to know the absorber diffusivity. The diffusivity is related to the internal thermal conductivity and heat capacity of the absorber: $D = x^2(G/C)$, where G is the end-to-end conductivity, C is the total heat capacity, and x is the length of the absorber (Saab et al., 2007). We can estimate the conductivity using the Wiedemann-Franz law, and calculate the expected heat capacity based on the volume. Assuming bulk resistivity for the gold and RRR = 5, this would imply $D = 6.6 \times 10^4$ $\mu\text{m}^2/\mu\text{s}$ for these devices. This is probably optimistic, as it is often difficult to achieve bulk resistivity in a thin film. Furthermore, as we shall see later, the absorbers often show signs of excess heat capacity. The diffusivity will decrease linearly as the room temperature resistivity or the low-temperature heat capacity increase, or as RRR decreases. We can simulate a range of diffusivities to get an idea of how the performance will degrade as the diffusivity decreases.

In the following simulations, the geometry and thermal and electrical properties of the TES and absorber were assumed to be identical to the device modeled in Chapter 4. The

890 μm × 890 μm × 0.2 μm absorber was divided into 441 equally-sized volume elements, and Equations 5.1 were used to calculate the temperature of the TES as a function of time for X-rays incident in each element. An illustration of the grid used to model the TES and absorber is shown in Figure 5.1.

The energy input used in simulation was 1.4867 keV, equivalent to an Al Kα X-ray. This energy was chosen to facilitate comparison to data, since we can readily produce these X-rays in the lab, and the natural line width for Al Kα is narrow, which makes it

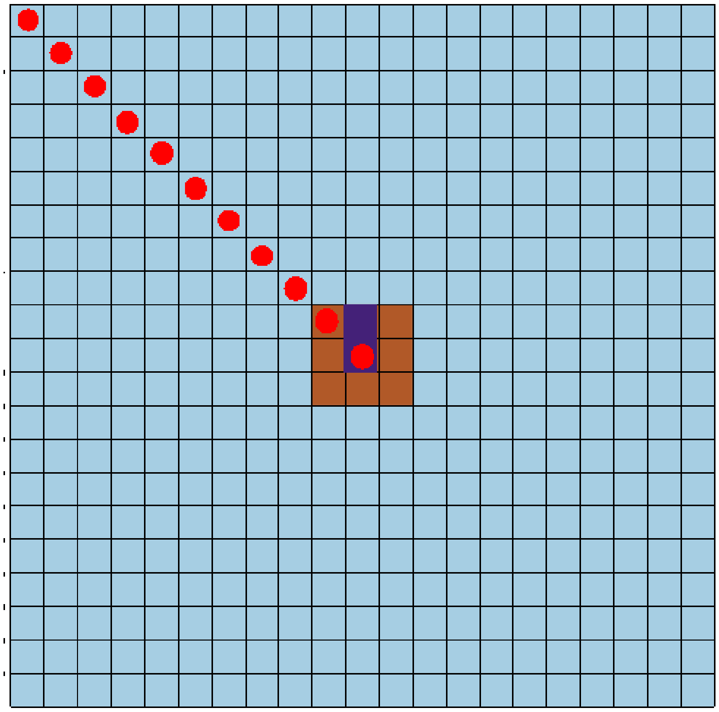

Figure 5.1: Illustration of the simulation geometry. The 890 μm × 890 μm × 0.2 μm absorber (light blue) is divided into 441 equally-sized volume elements. The location of the TES is shown in brown at the center of the absorber. The TES lies underneath the absorber, and makes thermal contact to it only in the stem area, marked in purple. The red dots indicate the locations of the incident X-rays plotted in Fig. 5.2, Fig. 5.3, and 5.4. When the X-ray strikes where the absorber and TES overlap, the X-ray is assumed to be thermalized in the absorber, and the heat is transported into the TES via the stem, which has a large (but finite) thermal conductivity ($G(0.1K) = 0.5$ μW/K for this simulation).

useful for characterizing high resolution detectors. However, the amount of broadening simply scales linearly with energy, so the result can be extrapolated to any incident energy.

Figures 5.2 and 5.3 show how the temperature rise in the TES changes as a function of incident X-ray position for two different absorber diffusivities (D=1×10^4 and 3×10^4 $\mu\text{m}^2/\mu\text{s}$, respectively) as a function of time. We see that events that are absorbed close to the TES are sharply peaked in temperature, and that the entire device comes to equilibrium on a time scale of tens of microseconds. The current signal that is read out via the SQUID amplifier chain will be low-pass filtered by the input inductance of the SQUID and the shunt resistance. For typical input inductance of 20 nH, and $R_{sh} \approx 250\ \mu\Omega$, this cutoff frequency is about 2 kHz. Since the device equilibrates within about twenty microseconds, we expect the pulse shapes at longer times to be identical (or, equivalently, we expect the pulse shape power spectra to be identical at low frequency), which we see in Figure 5.4. This result implies that slowing the fall time of the pulses will reduce the degradation due to position dependent pulse shape, which only occurs at high frequencies.

Now, we would like to determine how the position dependent pulse shape degrades the energy resolution. To do this, we assume the absorber is evenly illuminated by the X-ray source, and construct an average pulse shape template by weighting the pulse shapes as a function of distance from the TES accordingly. Then, we use the average pulse template and the expected noise spectrum for this device (modeled using μCal software, see Chapter 4) to construct the optimal filter. The optimal filter is applied to each of the simulated events to determine the pulse height (e.g. the best estimate of the incident X-ray energy). In Chapter 4, we found that the intrinsic energy resolution for this device was 2 eV FWHM due to the fundamental sources of noise in the device, including thermal fluctuation noise, Johnson noise, and amplifier noise. We can convolve our pulse height spectrum for the

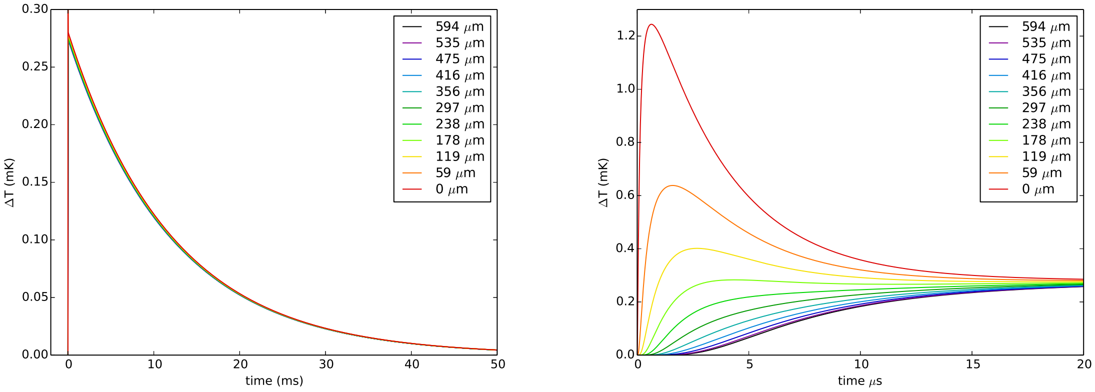

Figure 5.2: TES temperature as a function of time for X-rays incident at varying distances from the sensor (indicated by red dots in Figure 5.1) and absorber D = 1 × 10^4 $\mu m^2/\mu s$. The distances given are computed as the distance between the center of the TES and the center of the volume element where the X-ray was incident. Left: The full pulse. The time scale on which the pulse decays back to the bath temperature is determined by $\tau \equiv C/G_{tes-b}$, and is much longer than the absorber thermalization time, so the pulse shape variation is difficult to see on this time scale. Right: An expanded view of the pulse rise, showing the position dependent pulse shape.

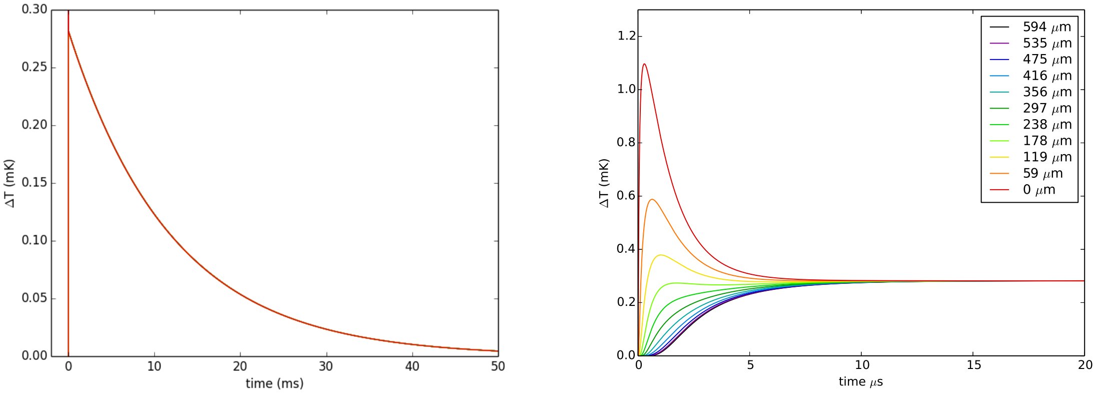

Figure 5.3: TES temperature as a function of time for X-rays incident at varying distances from the sensor (indicated by red dots in Figure 5.1) and absorber D = 3 × 10^4 $\mu m^2/\mu s$. The distances given are computed as the distance between the center of the TES and the center of the volume element where the X-ray was incident. Left: The full pulse. The time scale on which the pulse decays back to the bath temperature is determined by $\tau \equiv C/G_{tes-b}$, and is much longer than the absorber thermalization time, so the pulse shape variation is difficult to see on this time scale. Right: An expanded view of the pulse rise, showing the position dependent pulse shape.

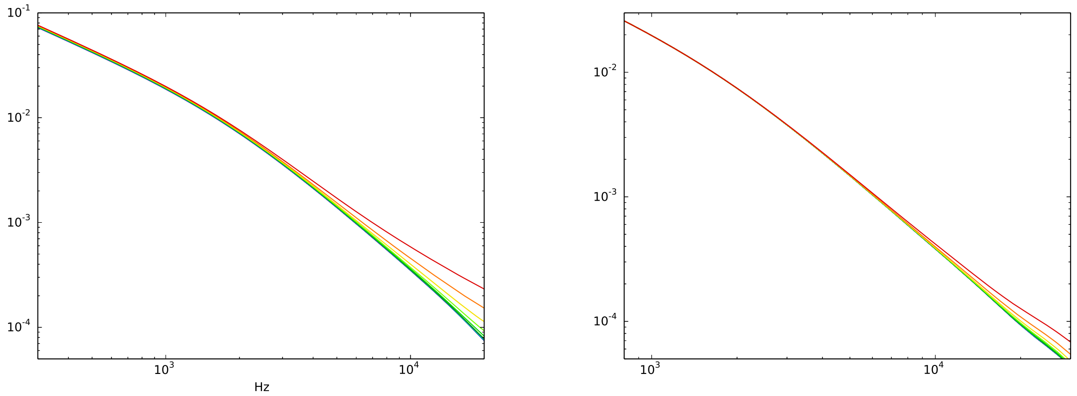

Figure 5.4: Pulse shape differences in frequency space as a function of distance of the incident X-ray from the sensor. The input inductance of the first stage SQUID and the shunt resistor form a low-pass filter that reduces some of the effect of the position dependence (shown: L = 20 nH, R = 0.22 mΩ. The colors of the traces correspond to the same distances indicated in Fig. 5.2 and 5.3). Left: D = 1 × 10^4 μm^2/μs Right: D = 3 × 10^4 μm^2/μs

position-dependent pulse shapes with the 2 eV intrinsic detector response to see how the shape of the pulse height spectrum changes as the absorber diffusivity decreases. As Figure 5.5 shows, the broadening due to position-dependent pulse shape is non-gaussian and tends to produce a high energy "shoulder" on the line. We also see that for the pixel we have modeled, the broadening due to position dependence is minimal for diffusivities larger than about 1.5 × 10^4 μm^2/μs at 1.5 keV.

Since the broadening is highly non-gaussian, we cannot characterize it using the FWHM, like we do for the intrinsic resolution. Instead, we can characterize the amount of broadening as a function of diffusivity by taking the difference between the maximum and minimum optimally filtered energies. This value is plotted for 1.4867 keV incident energy in Figure 5.6. We see that for D = 1.5 × 10^4 μm^2/μs, we expect our 2 eV intrinsic response to increase to about 2.5 eV at 1.5 keV. Extrapolating to the 250-500 eV range that we are ultimately interested in, this would result in less than 0.1 eV change in line width.

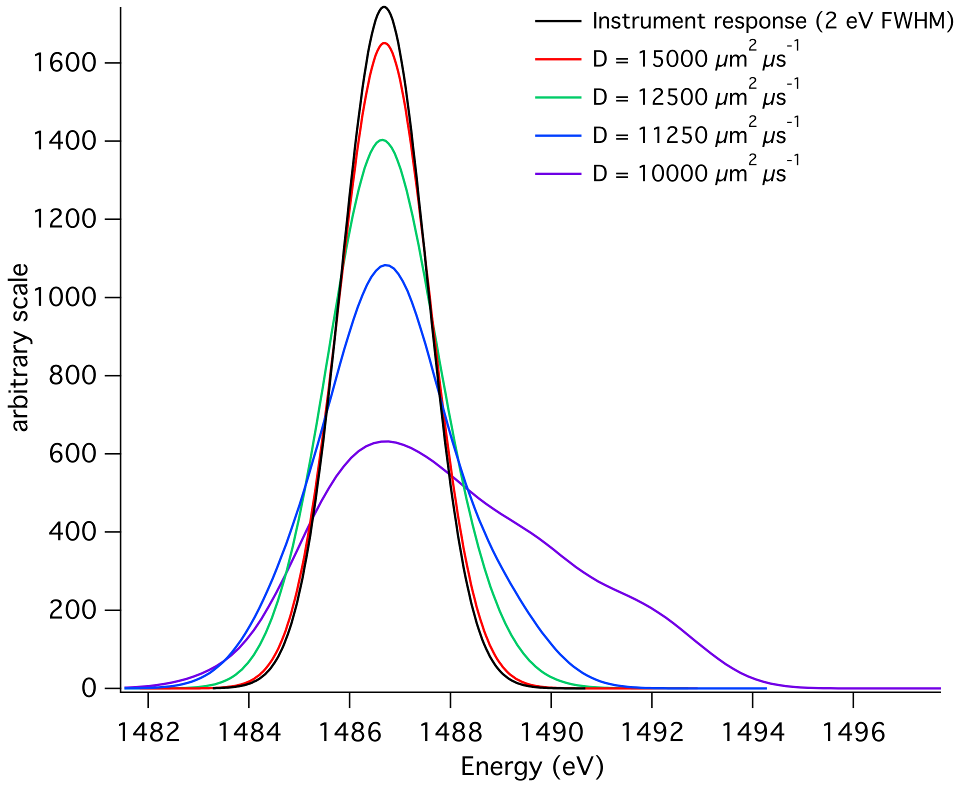

Figure 5.5: Simulated pulse height spectrum at 1.4867 keV (Al Kα) for a range of absorber diffusivities, convolved with the detector response, assuming the TES has 2 eV FWHM intrinsic energy resolution. The broadening due to diffusivity is non-gaussian and scales linearly with incident energy. For high diffusivity ($D_{abs} > 15000\,\mu\,\mathrm{m}^2\,\mu\mathrm{s}^{-1}$), the broadening is small compared to the intrinsic response of the detector at energies below 1.5 keV.

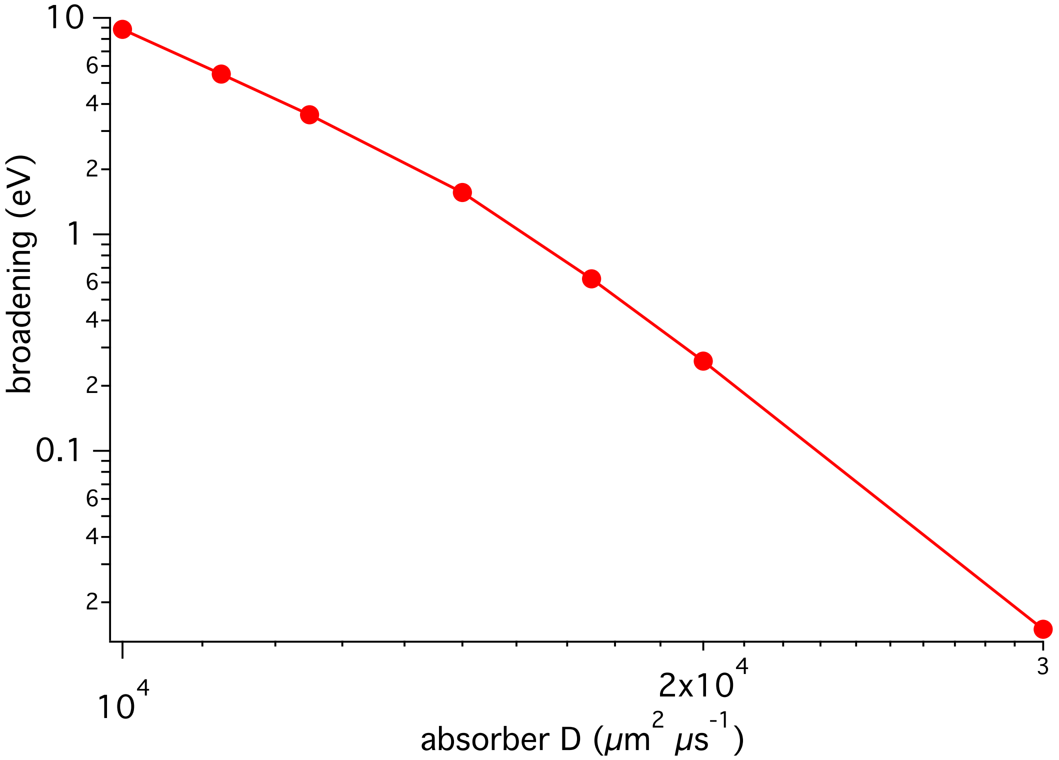

Figure 5.6: Amount of broadening due to diffusivity (not including the intrinsic detector resolution) as a function of absorber diffusivity for 1.5 keV incident energy. The broadening is non-gaussian, so the magnitude of broadening given is the difference between the maximum and minimum optimally filtered energies.

Chapter 6

Results: Fabrication

This chapter outlines the fabrication procedure for the devices, which were made by the Detector Development Laboratory (DDL) at Goddard Space Flight Center. The first wafer (MXW1) was completed in July 2014. MXW1 was given thicker gold absorbers (0.5 μm rather than 0.2 μm) out of concern that if they were made thinner the suspended absorbers would be likely to fail. The 0.5 μm suspended absorbers yielded successfully, but a high failure rate for the pixels with coplanar absorbers led to a number of changes to their construction. While MXW1 was finished and tested, the DDL developed a new process for making suspended absorbers. All of these new ideas were incorporated into the second wafer, MXW2, completed in February 2015.

The molybdenum/gold bilayers are e-beam evaporated onto a heated Si wafer with a 1 μm low stress silicon nitride layer. The molybdenum layer is 50 nm, and the thickness of the gold is adjusted to produce the desired T_c. The amount of normal metal needed is process dependent, and in this case, approximately 240-250 nm of gold was expected to produce a 70 mK transition temperature. The gold is then selectively etched away to form the TESs, and the molybdenum is patterned into bias leads and contact pads. A layer of niobium is added to the leads, increasing their superconducting transition temperature. Next, extra gold is deposited onto the TES to form banks parallel to the current flow, and bars perpendicular to the bias current that do not extend across the entire device. These bars, sometimes referred to as “zebra stripes,” suppress α, and therefore reduce the internal thermal fluctuation noise. The banks serve the dual purpose of helping suppress excess noise and preventing a superconducting short across the TES in the event that the gold layer is over-etched.

Next, reactive ion etching is used to make trenches in the nitride membrane that reduce the thermal conductivity between the TES/absorber and the bath. The absorbers require several processing steps. First, a thin titanium layer is sputtered to act as a sticking layer between the gold and the nitride membrane. In GSFC’s conventional process, a thin layer of gold is also sputtered, followed by a layer of electroplated gold to bring the absorber to its final thickness. MXW1 was given 0.5 μm thick absorbers, rather than 0.2 μm called for by the design, because a process to yield the thinner suspended absorbers was still in development. So, MXW1 received a 5/100 nm Ti/Au sputtered “seed layer,” followed by 0.4 μm of electroplated gold. For MXW2, the entire thickness (0.2 μm) of the gold layer was sputtered. The absorber metal layers are then patterned into individual pixels.

Finally a deep RIE etch is used on the back side of the wafer to etch through the silicon. The DRIE process creates a “well” with nearly vertical sidewalls underneath each pixel, leaving a freestanding nitride membrane to thermally isolate the pixel from the bath. Finally, acetone is used to remove the remaining photoresist from the front side, releasing the absorbers and leaving a gap between absorber and substrate/TES.

6.1 First wafer: lessons from MXW1

Although the target critical temperature for the Mo/Au bilayer was 70 mK, the actual T_c for MXW1 turned out to be considerably higher, about 100 mK. And, as previously mentioned, the absorbers were electroplated to a total gold thickness of 0.5 μm. Therefore, these devices had higher heat capacity and consequently poorer energy resolution than the target design. Nonetheless, the fabrication process proved highly instructive.

The results from MXW1 pointed to a number of ways that the yield could be improved for subsequent wafers. The suspended absorbers showed signs of rippling or warping (see Figure 6.1), which was consistent with results from previous attempts to fabricate 0.5-0.7 μm gold absorbers (Eckart et al., 2013). It is likely that this rippling is caused by high stress in the titanium seed/adhesion layer. Although the rippling did not cause breakage or touches to the substrate, these problems would be more likely for MXW2 when the gold layer was 2.5 times thinner. On future wafers, we would deposit titanium only underneath the stems where it was necessary to adhere the absorber gold to the nitride/TES.

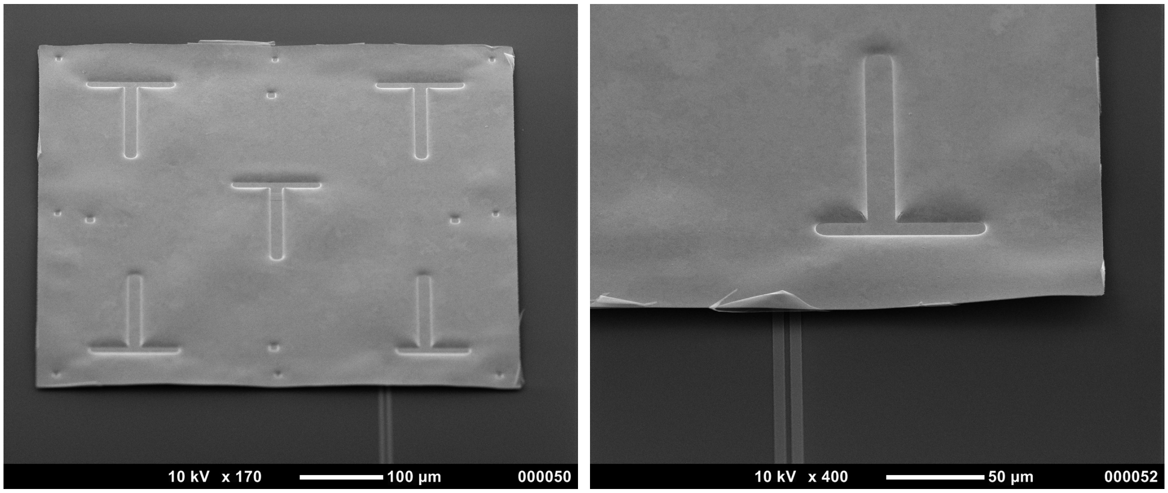

Figure 6.1: SEM image of a 590 × 590 × 0.5 μm gold absorber showing signs of rippling/warping. Although nearly all the suspended absorbers looked warped, SEM images revealed no evidence of cracking, breakage, or touches to the substrate.

Contrary to expectations, the coplanar absorbers fared quite poorly relative to the suspended designs. The coplanar pixels were made in three sizes, with absorber areas of approximately 350 × 350 μm, 480 × 480 μm, and 765 × 765 μm (minus the area of the TES). On many pixels, inspections revealed cracks in the nitride membrane, most often near the corners of the pixels (see Fig. 6.2 and Fig. 6.3). Cracks were most frequent on larger sizes (nearly 100% of the 765 × 765 μm pixels showed signs of breakage) and on the membranes with the highest percentage of the perimeter perforated. The cracking was aggravated by wirebonding and thermal cycling, causing several of the 765 × 765 μm pixels to break out completely. Again, we attributed this to high stress in the absorber, probably in the titanium sticking layer. Rather than warping or wrinkling like the suspended absorbers, the membrane simply cracked.

One aspect of the coplanar pixel fabrication that proved more successful than anticipated was the gold "finger" thermally connecting the absorber and the TES. Given that the gold absorber layer would have to climb over the Mo/Au bilayer and the thick extra gold deposited to form the banks, there was concern that the step coverage would not be adequate to provide a good thermal connection between absorber and thermometer. Anticipating this problem, MXW1 had several design variants for the thermal finger. In the simplest case, the absorber gold simply overlapped the bilayer/bank layers. On some pixels, we added a break in the bank making a trench so that the absorber gold only had to climb up over the bilayer. Other pixels were given an extra gold layer placed underneath the bank and absorber gold to form a "bridge" connecting the two structures. Visual inspection of the finished wafer did not show signs of cracks or breaks in the thermal finger, and during testing we saw no signs of poor thermal connection between absorber and TES (see section 8), even on the simplest designs.

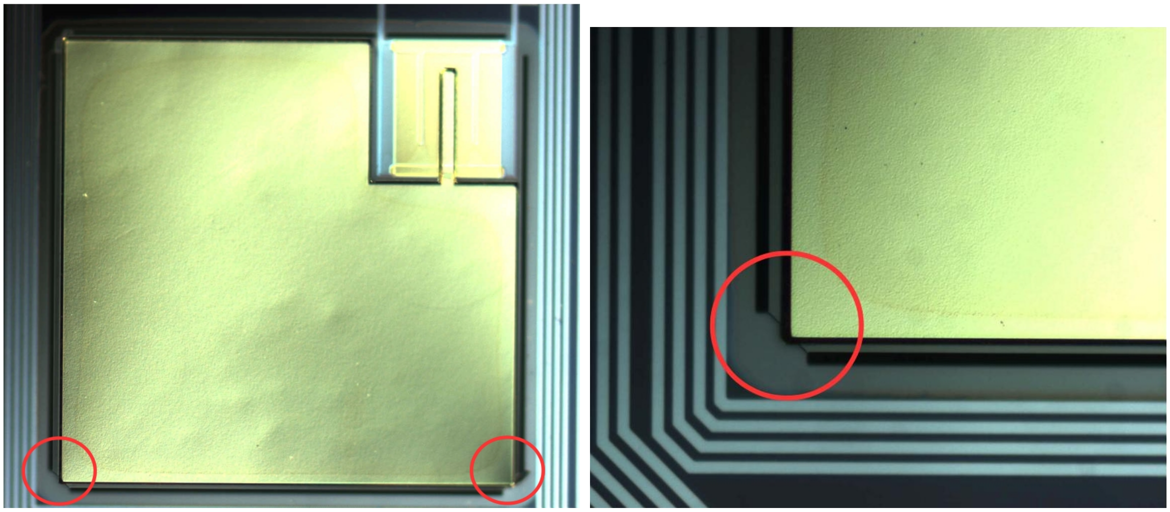

Figure 6.2: MXW1 optical microscope images. Cracks in the nitride membrane (circled in red) appeared on pixels with coplanar absorbers, probably due to stress in the titanium sticking layer. This pixel has a 480 × 480 μm absorber and long slots etched into each side of the membrane. Left: 20× zoom. Right: 50× zoom showing cracked membrane.

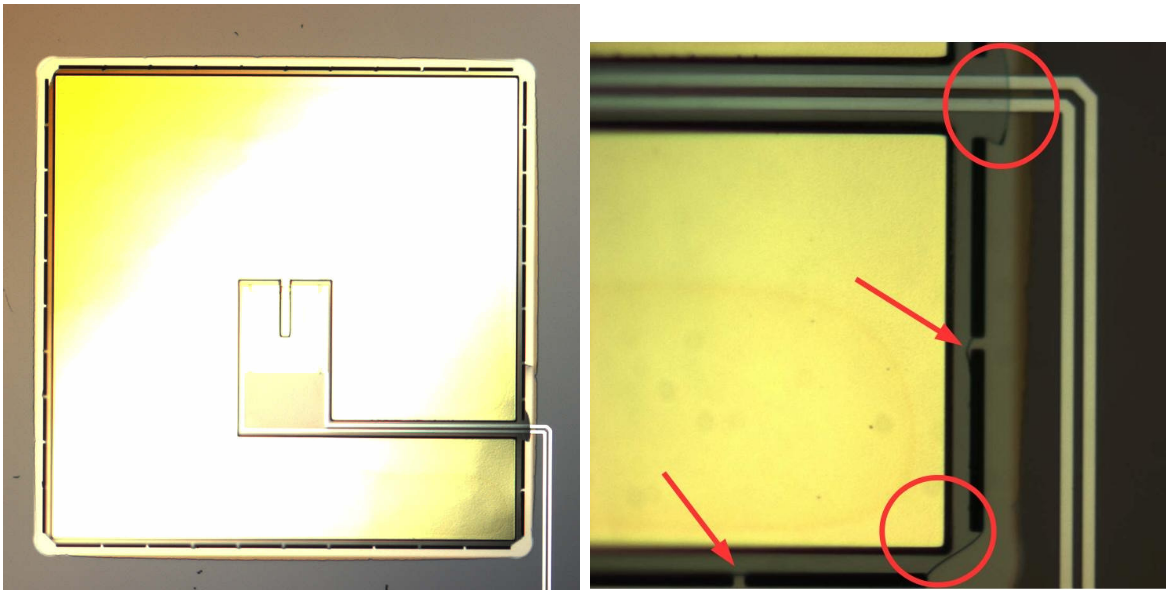

Figure 6.3: MXW1 optical microscope images. Cracks in the nitride membrane (circled in red) appeared on pixels with coplanar absorbers, probably due to stress in the titanium sticking layer. This pixel has a 765 × 765 μm absorber and approximately 90% of the membrane perimeter is etched. Left: Extensive cracking of the membrane has caused the pixel to partially detach from the wafer. Right: close-up view showing cracks between slots etched into the membrane, including a crack that severed the electrical leads.

6.2 Second wafer: changes for MXW2

A number of changes were made to the mask layout prior to the second fabrication run in hopes of improving yield for coplanar absorbers and improving the odds of survival for the suspended absorbers, since this wafer would have 200 nm thick gold. In the original design, the titanium seed layer had the same footprint as the absorber gold layer. Since titanium has a tendency to be high stress, it was thought that the Ti seed layer might be to blame for the membrane cracks in the coplanar pixels and some of the wrinkling in the suspended absorbers. However, some titanium is necessary to provide adhesion between the gold and the membrane; without it, the absorbers would just detach. So, to reduce the area of the Ti layer, we altered the masks so that titanium was only sputtered directly underneath the support stems for the suspended absorbers. Where there was a vacuum gap between the absorber and the membrane/TES, there would be no titanium. In the coplanar designs, the Ti was put down in a grid of 10 μm diameter dots to stick the absorber to the membrane.

To further reduce stress in the membrane the corners of the slots cut into the membrane were rounded. Though the motivation for this change was to address the issues with the coplanar designs, the rounded corners were used for both coplanar and suspended designs. Finally, since the absorber-to-TES overlapping "finger" used in place of the T-stem on the coplanar designs showed no signs of step coverage issues on MXW1, we eliminated the designs with a break in the normal metal bank along the edge of the TES, but kept the designs with an additional gold "bridge" running under the bank between absorber and TES.

In an attempt to provide additional mechanical support for the thin suspended gold layer, 15 μm of gold was electroplated into the stems after they were sputter deposited (see illustration in Fig. 6.4). This is a technique developed by the DDL that had been shown to eliminate the wrinkling in thin comparably thin absorbers, although it had not been previously attempted on membrane suspended devices. The DDL fabricated two "dummy" wafers ahead of the final MXW2 device wafer. The first of these had 10 μm of gold plated into the stems, but after releasing the absorbers from the photoresist used to define the vacuum gap, they were very wrinkled, and in many cases drooped down to touch the substrate. The second dummy wafer was given a 15 μm electroplate, but this did not resolve the issue.

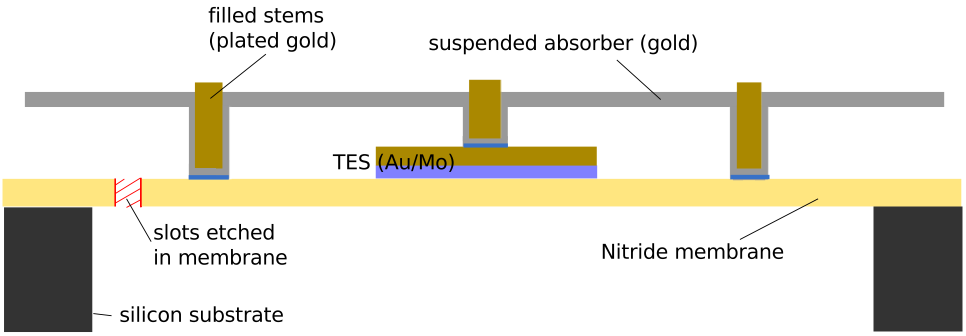

Figure 6.4: Cross sectional drawing of MXW2 suspended design, showing stems filled in with electroplated gold, and the area of the titanium seed layer (blue) reduced so that it is only deposited directly underneath the support stem areas.

Stress in the titanium seed layer was no longer a likely culprit for wrinkling the absorbers. Another possible cause is the heating required for the wax used to adhere the device wafer to the backing wafer for the deep RIE etch that clears the silicon underneath the membranes. So, an alternative process was tried on the first of two new wafers that were expected to yield testable devices. a heat release tape that works at a slightly lower temperature was substituted for the wax . Unfortunately, the heat release tape appeared not to provide adequate heat sinking during the etch, resulting in near universal failure of the nitride membranes. Although several possibles fixes for the heat release tape process were identified, we elected to run the second product wafer with the original wax process.

This was expected to yield the coplanar devices, but probably result in wrinkled and possibly drooping suspended absorbers.

The final product MXW2 wafer was completed and tested in February, 2015. The TES bilayer was sputter deposited, with 50 nm of molybdenum and 240 nm of gold, with an average T_c of about 70 mK. The absorbers had 200 nm of sputtered gold, followed by a 100 nm electroplate in an attempt to prevent wrinkling. However, imaging showed the suspended absorbers were very wrinkled (see Fig. 6.5), and SEM images of the 900 μm absorbers showed that the edges were drooping and in many places touched the substrates. Some of the smallest suspended absorbers (240 μm × 240 μm) did yield successfully without any touches (Fig. 6.6). Fortunately, the coplanar designs proved much more succesful. A visual inspection of a 4 × 5 array of 765 μm sized absorbers (the largest size on the wafer) found no cracks in the membrane after fabrication. Images of a 765 μm sized pixel are shown in Figure 6.7. In contrast, nearly 100% of pixels this size on MXW1 had visible cracks before any thermal cycling or wirebonding. One issue that was observed on many of the coplanar pixels on this wafer was a result of an edge of the coplanar absorbers being left exposed during the stem fill electroplate, causing gold to plate onto many of the coplanar pixels near the leads. The leads were protected by photoresist during this step, so in some cases the excess gold may not be shorting the leads (see Fig. 6.8).

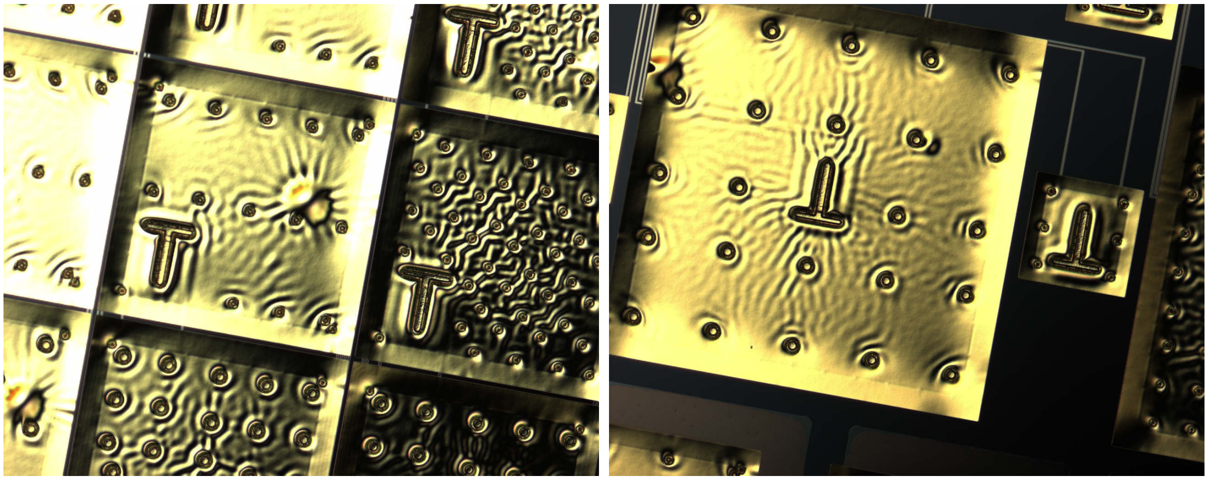

Figure 6.5: Optical microscope images of MXW2 pixels show extensive wrinkling on large suspended absorbers. Left: 590 μm × 590 μm absorbers. Right: 890 μm × 890 μm and 240 μm × 240 μm pixels.

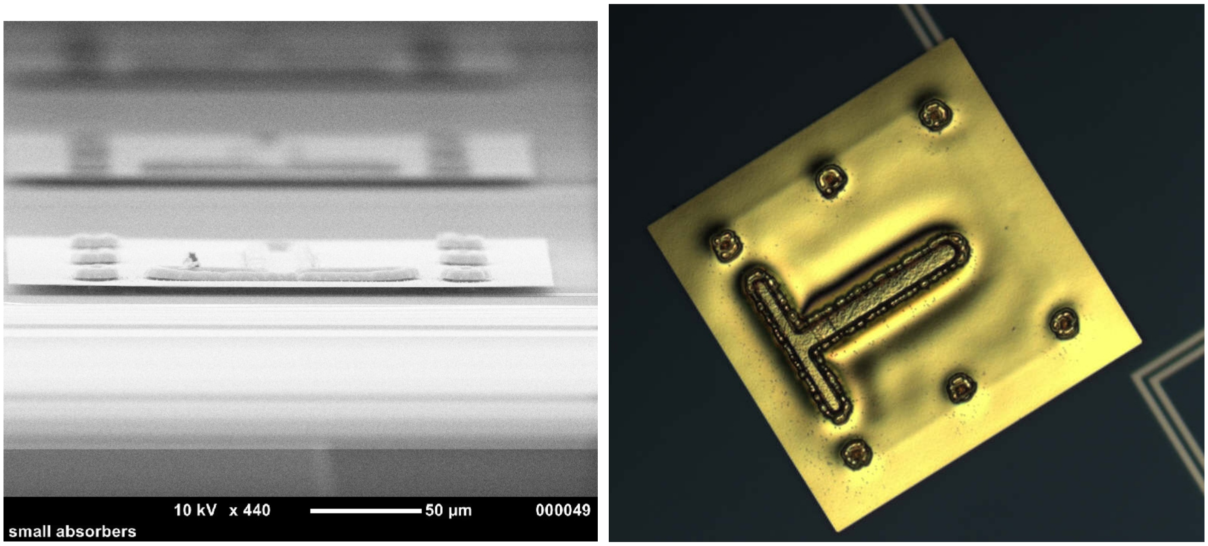

Figure 6.6: Images of MXW2 240 μm × 240 μm suspended absorbers. Left: SEM image (nearly edge-on) showing that the 300 nm thick gold absorber appears flat, and is not wrinkled or drooping. The electroplated gold filling the stem areas is visible protruding above the absorber. Right: Optical microscope image (face-on) of a pixel with the same stem pattern.

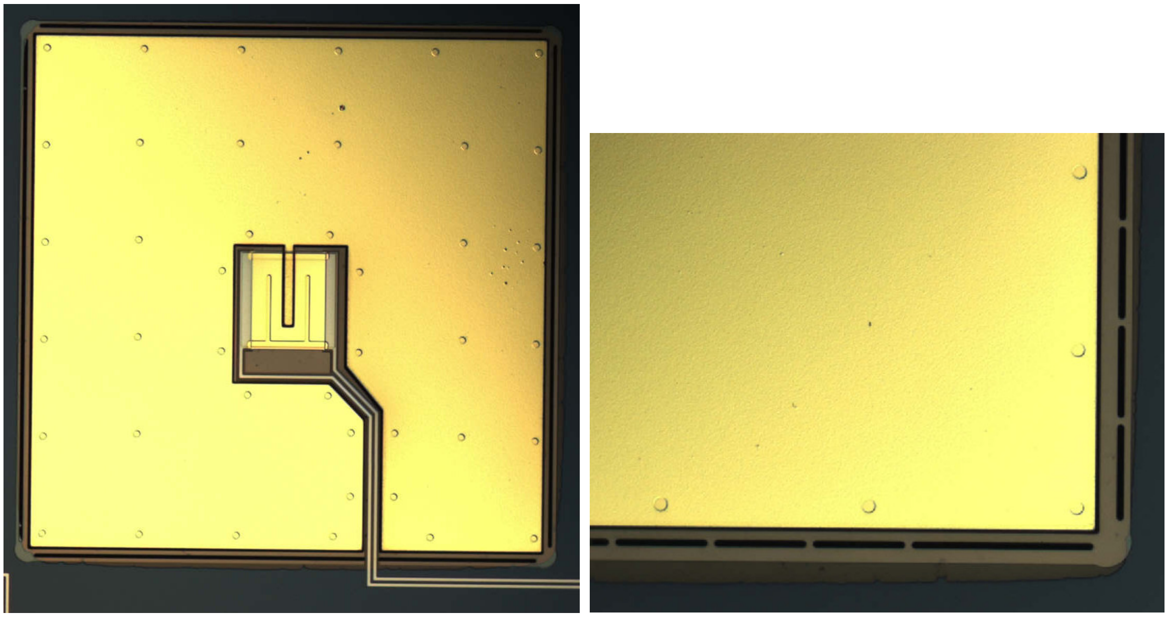

Figure 6.7: Optical microscope images of 765 μm × 765 μm coplanar absorbers. Left: Pixel with long slot cut into the nitride membrane along each side, leaving only the corners intact. Also visible are the 10 μm Ti seed layer dots used to adhere the absorber to the nitride. Right: Close up of a pixel with coplanar absorber and 90% membrane perforation. For MXW2, the corners of the slots were rounded to reduce stress in the membrane.

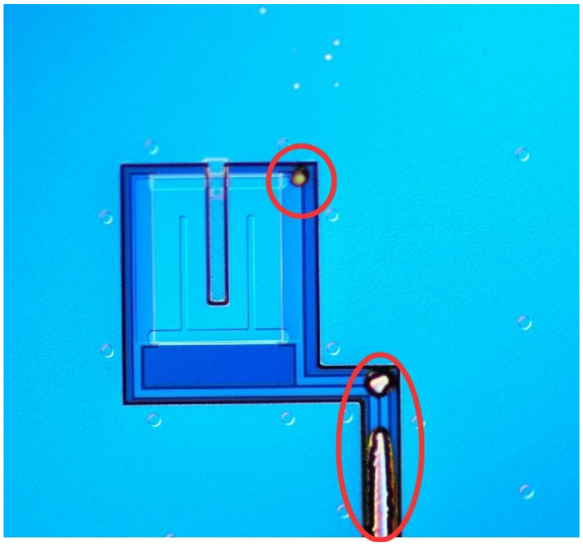

Figure 6.8: Some edges of the coplanar absorbers were left exposed during the stem fill electroplate, causing a small amount of gold to plate over the leads (areas circled in red). The leads were protected by photoresist during the electroplating step, so in some cases the excess gold may not be shorting the leads.

Chapter 7

MXW1 test results: suspended absorbers

7.1 890 × 890 μm suspended absorbers: MXW1d

The first chip tested from MXW1 was a 4 × 6 array of 890 × 890 × 0.5 μm suspended absorbers ("MXW1d"). The pixels differed from one another in the size and number of absorber support stems, and the fraction of the membrane perimeter that was perforated. Therefore, they were all expected to have identical heat capacity, but different TES-to-bath thermal conductivity. The devices were tested at Goddard in an adiabatic demagnetization refrigerator (ADR) capable of cooling the detectors below 50 mK. The detector assembly is enclosed in a niobium box to prevent light leakage and to shield the TESs from magnetic fields. The ADR is cooled to 4 K with liquid helium and nitrogen baths. During the cool down from room temperature a Mu-metal can was placed around the dewar, which was then wrapped with a sheet consisting of multiple layers of Metglas in order to prevent trapping of Earth's magnetic field inside the detector box. The pixels were read out using a two-stage SQUID amplifier (with parts provided by PTB and NIST), consisting of a single input SQUID for each TES, which is then connected to a second stage SQUID array to couple the input stage to the room temperature electronics. The readout provides six channels for testing.

Figure 7.1 shows the absorber support stem layouts; the "small" stem configuration had thirty-two 7 μm $\times$ 7 μm square support stems on the membrane, and the "large" configuration had twenty-four 20 μm diameter round stems on the membrane. All pixels had one T-stem thermally connecting the absorber to the TES. Two different front etches were used, one that removed 91.7% of the membrane perimeter, and one where a long slot was cut along each side of the membrane, leaving only the corners intact (removing 97.5% of the perimeter). Removing more of the membrane reduces the thermal conductivity to the bath, G. This improves pulse shape uniformity, but makes the pulse fall times longer, so pulse pile-up becomes more likely. The combinations of support stems and front etches for the six pixels tested can be found in Table 7.1. The primary purpose of varying the size and density of support stems was to find the configuration that provided the best mechanical support for the thin suspended absorbers. Since the stems sit on the membrane, they are expected to affect the thermal conductivity between the device and the bath. So, while we might expect that having many large stems would provide better mechanical support, it should also increase the amount of heat lost from the absorber to the bath, increasing the conductivity G and possibly contributing to position dependent pulse shape variation.

To measure the transition temperature, the devices were AC biased at T slightly less than T_c. The bath temperature was then increased until the limit of the critical current was observed to go to zero. This temperature was taken as T_c, and is reported in Table 7.1. As expected, the critical temperatures for the six pixels ranged from about 105-107 mK.

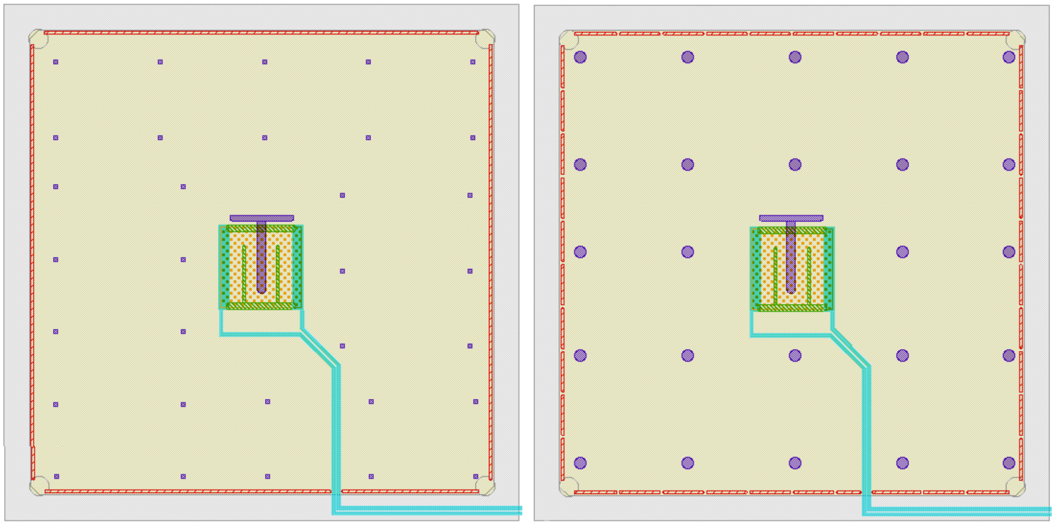

Figure 7.1: MXW1 chip d, illustration showing pixel geometries tested. All pixels had 890 × 890 × 0.5 μm suspended absorbers (gray, shown semi-transparent). Two different front etches were used (shown in red): in one case, 91.7% of the perimeter of the nitride membrane (yellow) was removed, in the other, 97.5% of the perimeter was removed. Two different patterns of absorber support stems (purple) were used. The "small" stem configuration had thirty-two 7 μm × 7 μm square support stems on the membrane, and the "large" configuration had twenty-four 20 μm diameter round stems on the membrane. Table 7.1 gives the membrane perforation/stem combination for each pixel. Left: Pixel 12 and 22, with small stems (purple) and 97.5% membrane perforation. Right: Pixel 23, with large stems stems (purple) and 91.7% of the membrane perimeter perforated.

It is difficult to completely shield the detectors from magnetic fields. However, since trapped fields affect the performance of the TES (see section 3.2), a Helmholtz coil located over the array and inside the niobium detector box is used to null any remaining magnetic field. One effect of the trapped field is to suppress the critical temperature of the TES, so to determine what external field is needed to null the trapped flux, the applied field is varied until the measured T_c is maximized. In this run, the maximum applied field was less than 2 μT, and the maximum change observed in the critical temperature was 0.3 mK, implying that there was very little residual field present (see Table 7.1). All subsequent data was acquired with the current in the field coil set to the value that maximized the

Pixel	stems	membrane	applied field (μT)	T_c (mK)	T_c w/ applied field
11	small	91.7%	-1.2	105.95	106.07
12	small	97.5%	-0.63	106.2	106.45
13	small	91.7%	-1.4	105.55	105.85
21	large	97.5%	0.95	106.20	106.33
22	small	97.5%	0.51	105.40	105.62
23	large	91.7%	1.96	105.80	105.90

Table 7.1: MXW1d pixel geometries tested. Applied field is the field that is observed to maximize T_c, and is assumed to be the field that nullifies the trapped flux. It is calculated based on the geometry of the field coil.

apparent T_c.

Current-voltage (IV) curves were used to measure the normal resistance (R_n), the sensor resistance, and the power dissipated in the sensor. An voltage (V_{in}) is applied to the bias circuit through a large input resistor ($R_{in} = 1.095\ k\Omega$), which forms a voltage divider with the shunt resistance ($R_{SH} = 0.2$ mΩ) to supply a bias voltage to the TES. This TES current is measured and converted to resistance and then power, since the shunt resistance is known. IV curves taken at a variety of bath temperatures were used to determine the thermal conductivity of the nitride membrane. The power dissipated in the sensor at 50% of the normal resistance is plotted versus temperature in Fig. 7.2 and Fig. 7.3. This data is fit using the expression $P = K(T_c^n - T_b^n)$ to determine T_c, n, and K (recall that $K \equiv G/nT^{n-1}$). Here, T_c is defined as the temperature at $R/R_n = 0.5$, so we have made the assumption that 50% R_n occurs at the same temperature for every T_b. However, the power dissipated at 50% R_n gets smaller as T_b increases. Therefore, the TES current at 50% R_n changes with T_b. If β, the current dependence of the TES resistance, is not zero, then the temperature at 50% R_n depends on the TES current. So, assuming that the TES temperature is the same at 50% R_n for every T_b is the same as assuming that $\beta = 0$. Based on past experience, we know β is probably non-zero, which introduces some error in the determination of the conductivity G and its temperature dependence, n. However, we also know that β tends to be small (< 1, for example, see Fig. 9.6) high in the transition, so the effect on G and n should be small. Once we have determined the conductivity, we can use the dissipated power to calculate the sensor temperature, since $T_{TES} = (P/K + T_b^n)^{(1/n)}$. We can now plot $R(T)$, and take partial derivatives to find α_{IV}.

We found $G(0.1K) = 100.2 \pm 9.3$ pW/K and $n = 3.32 \pm 0.03$ for pixel 11 (small stems, 91.7% perforation). For pixel 22 (small stems, 97.5% perforation) we measured $G(0.1K) = 84.4 \pm 4.3$ pW/K and $n = 3.37 \pm 0.02$. Based on the membrane perforation and the total perimeter of the TES and support stems, we expected $G_0 = 82$ and 25 pW/K for pixel 11 and 22, respectively. Fits to dissipated power as a function of bath temperature to determine G for pixels 11 and 22 are shown in Fig. 7.2 and 7.3, and IV curve data is shown in Fig. 7.4 and 7.5. Both pixels show smooth transitions, with no kinks or jumps. The transitions are also fairly sharp; α_{IV} is greater than 60 through most of the transition (though this method of determining α is sometimes found to overpredict the sensitivity, as opposed to deriving α from the shape of the X-ray pulses or from complex impedance measurements, see Ullom et al. (2004)).

X-ray spectra were obtained using manganese (Kα = 5.898 keV) and aluminum (Kα = 1.486 keV) targets fluoresced with an electron beam. Fig. 7.6 shows the average pulse shape and noise spectrum for pixel 22 illuminated with Mn Kα X-rays with a base temperature $T_b = 55$ mK. The pixel was biased at 15% R_n, as determined using the IV curve data. The data are optimally filtered (see Chapter 2) and fit using the known line shape for the Mn Kα complex to find that the energy resolution of the detector is 7.10 ± 0.2 eV FWHM. To interpret what that number means, we can compare it to the predicted resolution using the model discussed in Chapter 4. Since the membrane thermal conductivity we measured was significantly different from the prediction, we adopt the

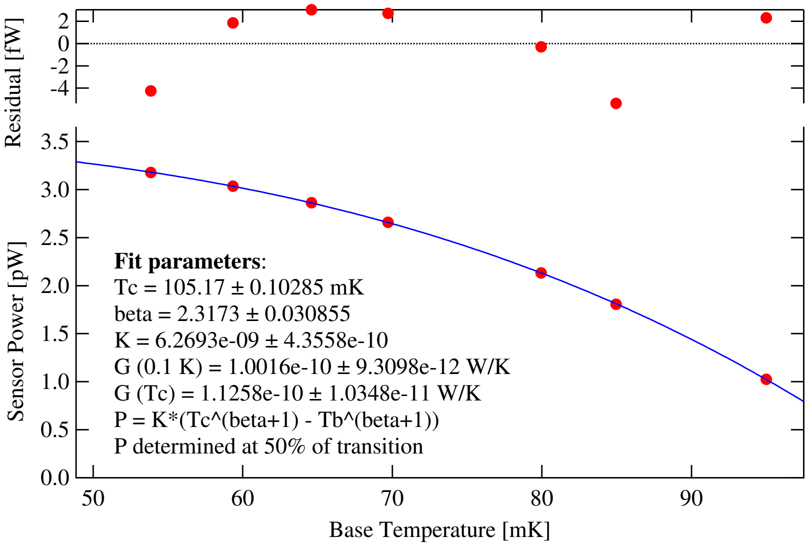

Figure 7.2: Pixel 11 (small stem pattern, 91.7% perforated membrane) dissipated power at 50% R_n as a function of bath temperature. Blue line shows a fit to $P = K(T_c^n - T_b^n)$, where T_c is the temperature at 50% R_n. Derived thermal conductivity between the sensor and the bath is $G_0 = G(0.1K) = 100.2 \pm 9.3$ pW/K, with $n = 3.32 \pm 0.03$.

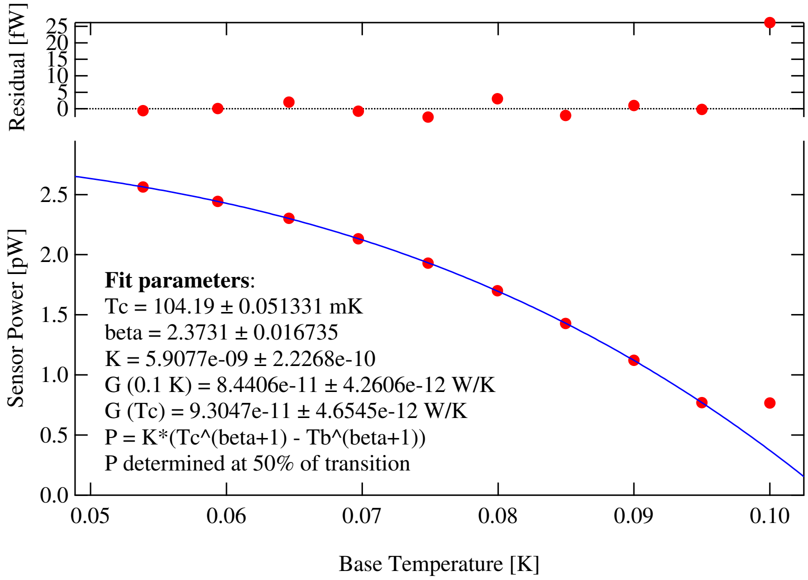

Figure 7.3: Pixel 22 (small stem pattern, 97.5% perforation) dissipated power at 50% R_n as a function of bath temperature. Blue line shows a fit to $P = K(T_c^n - T_b^n)$, where T_c is the temperature at 50% R_n. Derived thermal conductivity between the sensor and the bath is $G(0.1K) = 84.4 \pm 4.3$ pW/K, $n = 3.37 \pm 0.02$.

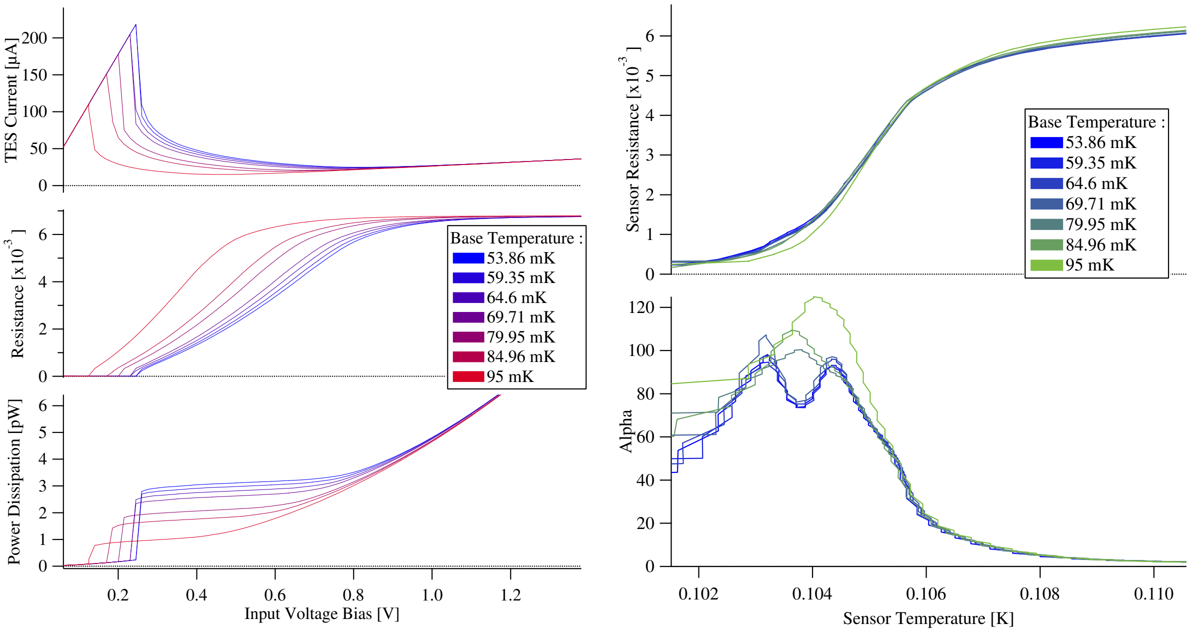

Figure 7.4: Pixel 11 (small stem pattern, 91.7% perforated membrane). A voltage (V_{in}) is applied to the bias circuit through a large input resistor ($R_{in} = 1.095\ k\Omega$), with a known shunt resistance (($R_{SH} = 0.2$ mΩ)) Left: TES current (top), resistance (middle) and dissipated power (bottom) as a function of V_{in}. Right: TES resistance (top) and sensitivity α (bottom) as a function of TES temperature, determined using the measured thermal conductivity and power dissipation.

measured value (G(0.1 K) = 84 pW/K). In Chapter 4, we assumed α = 55 and β=1.25. Putting these parameters and the measured G into our model, we find that the model predicts ΔE = 5.31 eV.

One source of discrepancy between the observed resolution at the Mn Kα line and the model's prediction could be broadening due to position-dependent pulse shape. Since this broadening should scale with incident energy, we should compare the resolution at 5.899 keV (and the predicted resolution, which does not account for position dependent broadening) to the energy resolution derived from the measured NEP and to the baseline "0 eV" energy resolution. The energy resolution from NEP (ΔE_{NEP}) is determined by integrating the signal-to-noise ratio, using the average X-ray pulse shape and average

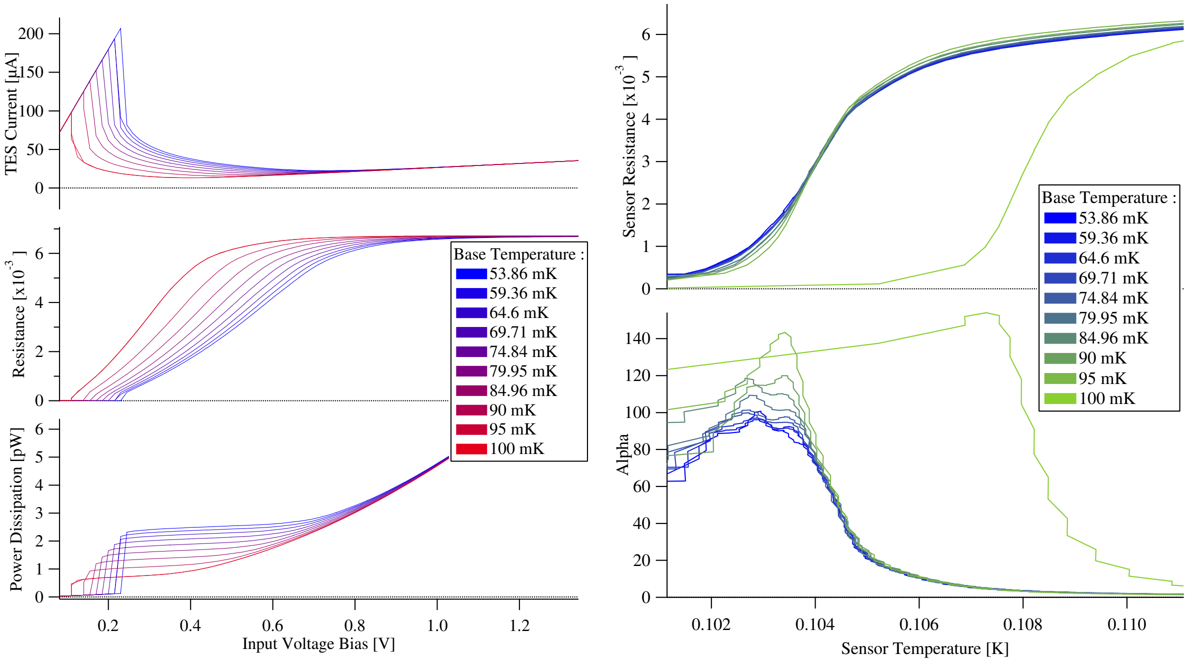

Figure 7.5: Pixel 22 (small stem pattern, 97.5% perforation). A voltage (V_{in}) is applied to the bias circuit through a large input resistor ($R_{in} = 1.095\ k\Omega$), with a known shunt resistance (($R_{SH} = 0.2\ \mathrm{m}\Omega$)) Left: TES current (top), resistance (middle) and dissipated power (bottom) as a function of V_{in}. Right: TES resistance (top) and sensitivity α (bottom) as a function of TES temperature, determined using the measured thermal conductivity and power dissipation.

noise spectrum that were used to optimally filter the data (see Equation 2.10). The energy resolution at $E > 0$ cannot be better than the resolution derived from the NEP. It will be the same as ΔE_{NEP} only if the detector is perfectly linear up to E_γ and there is no excess broadening.

The baseline resolution is obtained by applying the optimal filter to data segments without an X-ray pulse, so the fitted pulse height should be zero. Fitting a gaussian to a histogram of many samples of no-pulse data gives the baseline energy resolution, which should be just equal to ΔE_{NEP}. The ΔE_{NEP} for this data set was 6.11 eV, and the baseline resolution was 6.29 ± 0.06 eV. Since the baseline resolution and ΔE_{NEP} are close to one another, and both are significantly better than the 7.1 eV Mn Kα resolution, the excess

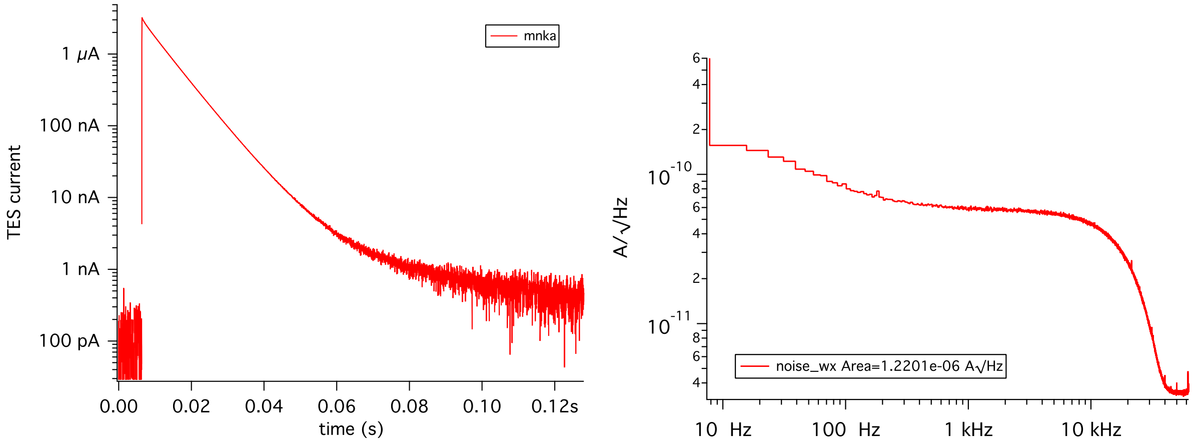

Figure 7.6: Pixel 22 (small stem pattern, 97.5% perforation), biased at 15% R_n, $T_b = 55$ mK. Left: Mn Kα average pulse shape. Right: Average noise spectrum.

broadening at 5.899 keV is likely due to position dependence. We can try to mitigate the effects of pulse shape variation and bring the Mn Kα resolution closer to the baseline by applying a low-pass filter to the data. Since this amounts to throwing out high frequency signal-to-noise ratio, ΔE_{NEP} will worsen. Applying a 10kHz single pole low pass filter increased ΔE_{NEP} to 6.15 eV, but the FWHM at Mn Kα improved to 6.66 ± 0.2 eV. With a 5 kHz low pass filter, $\Delta E_{NEP} = 6.20$ eV, and $\Delta E_{MnK\alpha} = 6.62 \pm 0.2$ eV. The fitted baseline and Mn Kα spectra with a 5 kHz filter applied to the optimal filter template are shown in Fig. 7.7.

The degradation in resolution between the baseline and 5.898 keV and subsequent improvement with the addition of the low pass filter implies a small amount of position-dependent broadening. The excess broadening and the baseline resolution add in quadrature, so we can derive that for $\Delta E_{base} = 6.3$ eV and $\Delta E_{MnK\alpha} = 7.06$ eV, the amount of broadening we can attribute to position dependence is about 3.27 eV. Ultimately, we're interested in the energy resolution in the $^1/_4$ keV range, so scaling linearly, we would expect only 0.8 eV broadening at 1.4 keV (e.g. the aluminum line) and 0.14 eV at 250 eV.

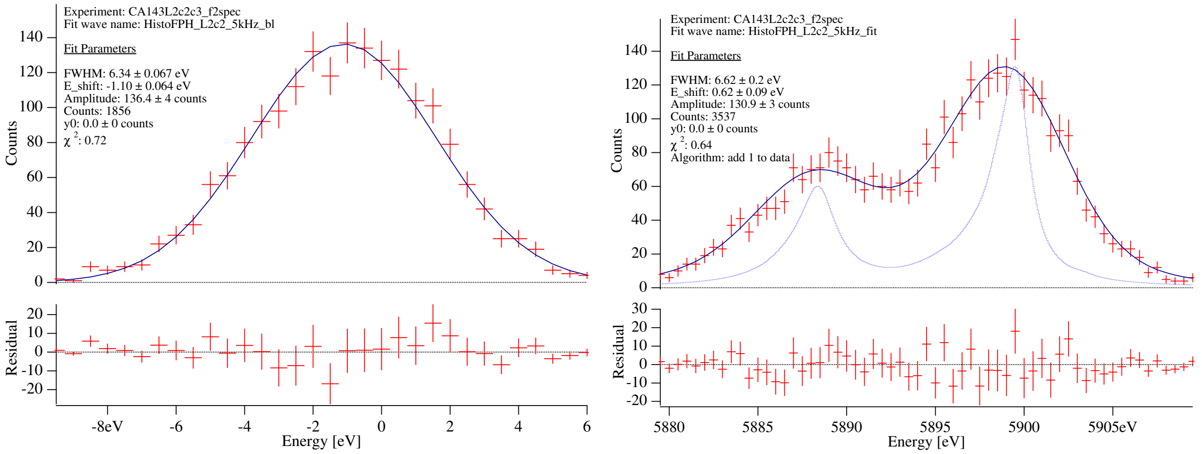

Figure 7.7: Pixel 22 (small stem pattern, 97.5% perforation), biased at 15% R_n, $T_b = 55$ mK. Left: baseline width is 6.29 ± 0.06 eV. Right: Mn Kα X-ray spectrum with 5 kHz low pass filter applied to optimal filter. Resolution is 6.66 ± 0.2 eV FWHM. The blue line shows the intrinsic profile of the Mn Kα1,2 line complex.

Even at 1.4 keV, this amount of broadening is negligible: the aluminum line would widen from 6.3 eV to 6.35 eV FWHM. To further convince ourselves that there is little position dependence, we can also look at a plot of the pulse rise time versus the optimally filtered pulse height for the Mn Kα line, as shown in 7.8, which shows no obvious correlation.

Spectra for Al Kα X-rays (Fig. 7.9) are consistent with our expectation that the broadening should scale with energy. We found $\Delta E_{NEP} = 6.01$ eV, the fitted baseline resolution was 6.12 ± 0.07 eV, and the Al Kα resolution was 6.05 ± 0.06 eV, even without applying a low pass filter.

Since all of the X-ray data described so far was obtained with the pixel biased at 15% R_n, we investigated how the energy resolution depends on the bias point. Fig. 7.10 shows the average pulse shape and noise spectra as the bias point ranges from 5-60% R_n. We use these data to calculate the ΔE_{NEP}, which is summarized in Table 7.2. In general, we see that the resolution is better lower in the transition, and that 15% R_n is probably close to the optimal bias point.

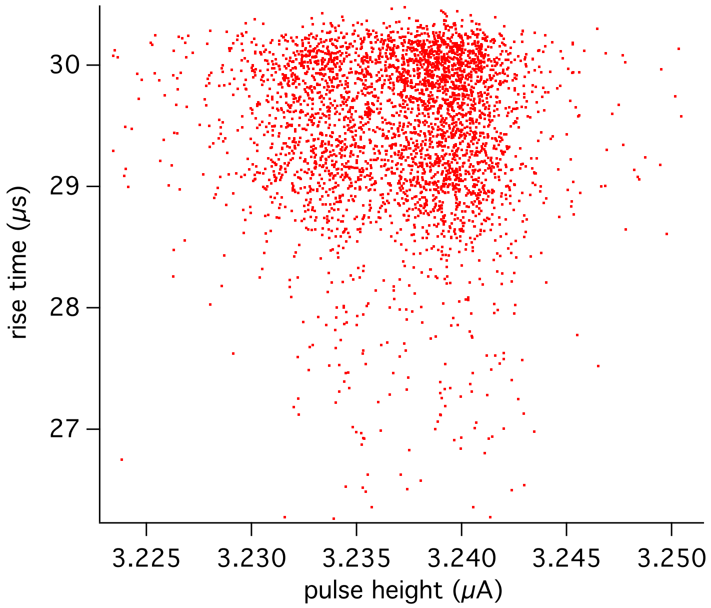

Figure 7.8: Pixel 22 (small stem pattern, 97.5% perforation) Mn Kα pulse rise time versus optimally filtered pulse height, same data set shown in Figure 7.7.

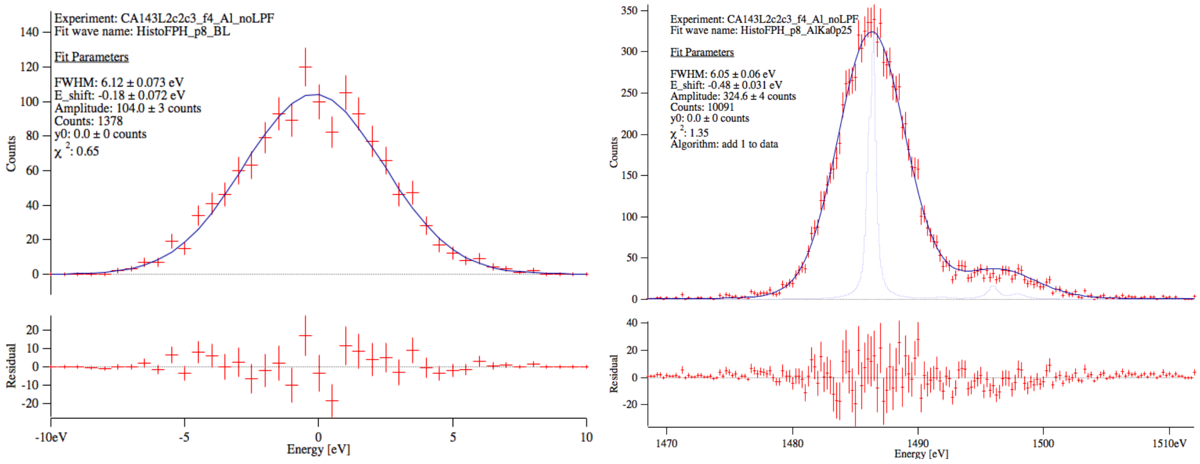

Figure 7.9: Pixel 22 (small stem pattern, 97.5% perforation), biased at 15% R_n, $T_b = 55$ mK. Left: baseline resolution is 6.12 ± 0.07 eV. Right: Al Kα X-ray spectrum. Fitted resolution is 6.05 ± 0.06 eV. The blue line shows the intrinsic profile of the Al Kα line complex.

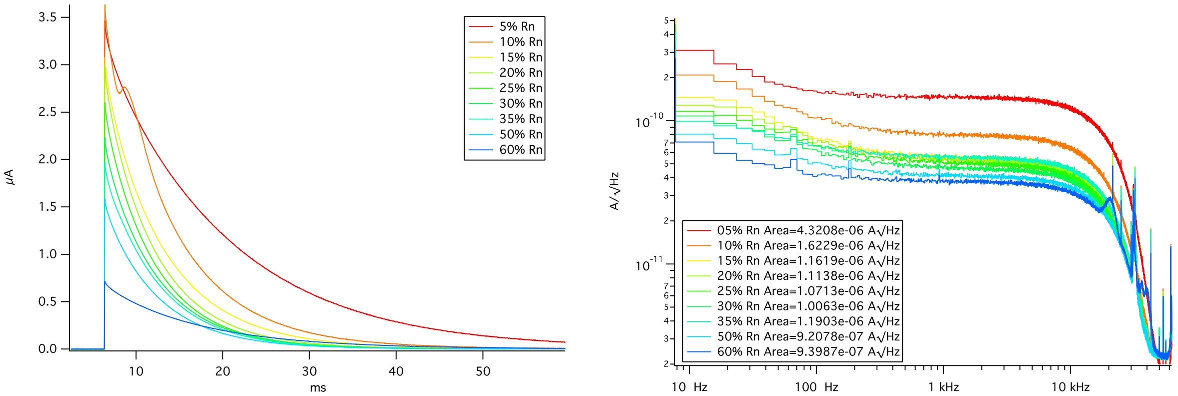

Figure 7.10: Pixel 22 (small stem pattern, 97.5% perforation), $T_b = 55$ mK. Left: Average pulse shape as a function of bias point (R/R_n). Right: Average noise versus bias point.

bias (% R_n)	pulse height (μA)	τ (ms)	α_{IV}	ΔE_{NEP} (eV)
5	3.64	14.03	72.3	9.11
10	3.47	7.42	88.7	6.48
15	3.08	7.07	98.1	6.02
20	2.98	5.93	100.1	6.01
25	2.60	5.83	90.0	6.36
30	2.23	6.03	86.8	6.67
35	1.92	6.19	83.5	7.75
50	1.58	6.19	64.5	7.51
60	0.72	11.18	39.4	11.55

Table 7.2: MXW1d pixel 22 measured values of pulse height, decay time, and energy resolution (derived from measured noise spectra and pulse shapes) as a function of bias point. The column α_{IV} gives α values derived from the IV curves (see Fig. 7.5).

We also obtained Mn Kα and Al Kα X-ray spectra for pixel 23. This pixel has large stems and 91.7% of the membrane perimeter perforated. This combination should produce a higher G compared to pixel 22. The larger stems also give the the device 36% more phonon emitting perimeter, which will increase loss between the absorber and substrate. However, the larger G has negligible effect on the modeled energy resolution, so we expect similar results for baseline resolution and ΔE_{NEP} to what we measured for pixel 22. The results are shown in Fig. 7.11 and 7.12. For the run using the Mn Kα source, the ΔE_{NEP} was 6.68 eV, with a fitted baseline resolution of 6.63 ± 0.11 eV. The energy resolution at 5.9 keV is 7.65 ± 0.23 eV, about 3.8 eV of broadening. This is slightly more than we observed on pixel 22 (3.3 eV broadening at 5.9 keV), which is qualitatively consistent with the increase in stem perimeter between the two pixels. The resolution improved to 7.06 ± 0.21 eV with a 5 kHz low pass filter applied to the optimal filter. For the Al Kα dataset, ΔE_{NEP} = 6.18 eV (the difference in ΔE_{NEP} from the Mn Kα data may be attributable in part to improved temperature stability). The fitted energy resolution at 1.486 keV was 6.38 ± 0.09 eV with no filtering. Scaling the broadening observed at 5.9 keV to this lower energy, we would expect to see 6.25 eV resolution for Al Kα.

Although modeling indicated that differences in ΔE_{NEP} should be negligible between these pixels, ΔE_{NEP} was worse for pixel 23 compared to pixel 22. This may be due to a combination of factors. For one, the applied magnetic field was tuned to cancel the field in pixel 22, which may have left a very small residual field in pixel 23. And, with scant IV curve data available for pixel 23, the bias point is less certain, which means that pixel 23 may have been biased higher or lower in the transition than pixel 22. It is difficult to ascertain how much of the pixel to pixel variation can be attributed to differences like these and how much may be due to other factors, such as pixel geometry or fabrication-related differences.

Finally, we measured the total heat capacity of pixels 11 and 22 by taking X-ray data at $T_b \approx T_C$, where the effects of electrothermal feedback are minimal and we can assume that the fall time of the pulses is dominated by the thermal time constant, $\tau_0 = C/G$. Fitting the average pulse shapes to a single exponential (see Fig. 7.13) and using the measured thermal conductivity, we to find that C(0.1 K) = 4.92×10^{-12} J/K for pixel 11 and 4.77×10^{-12} J/K for pixel 22. This is about 70% higher than the expected heat

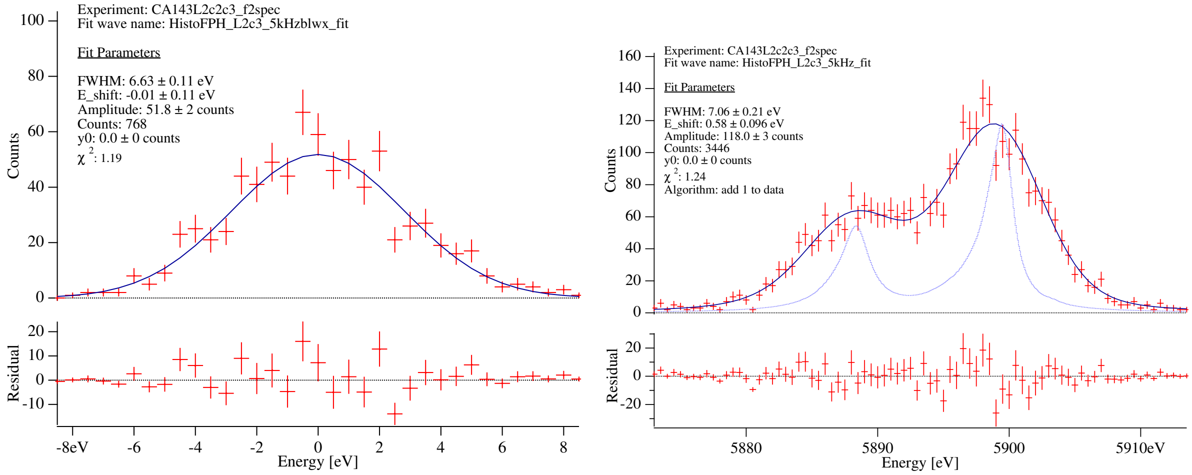

Figure 7.11: Pixel 23 (large stem pattern, 91.7% membrane perforation), biased at 15% R_n, T_b = 55 mK. Left: baseline resolution is 6.63 ± 0.11 eV Right: Mn Kα spectrum with 5 kHz low pass filter applied to the optimal filter. Resolution is 7.06 ± 0.21 eV. The blue line shows the intrinsic profile of the Mn Kα1,2 line complex.

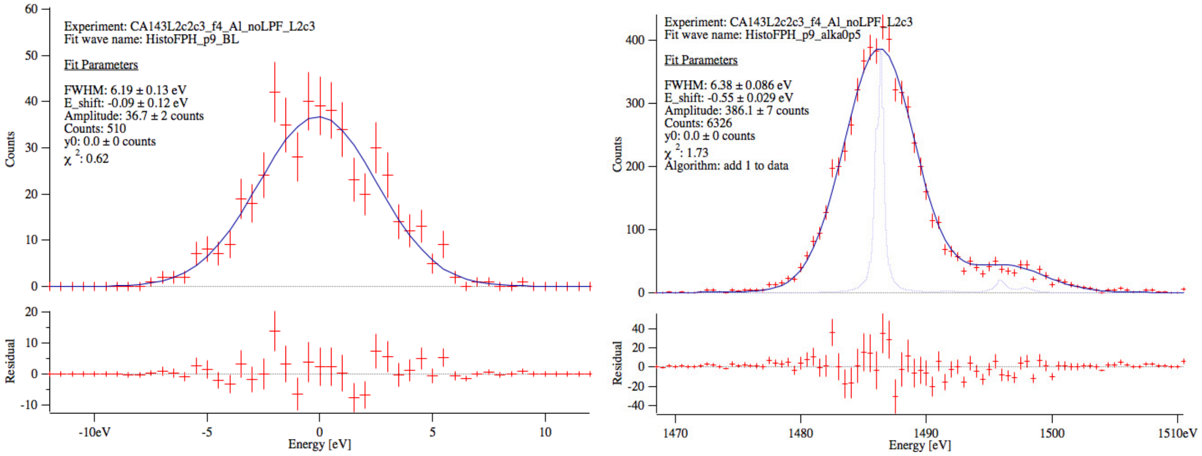

Figure 7.12: Pixel 23 (large stem pattern, 91.7% membrane perforation), biased at 15% R_n, T_b = 55 mK. Left: baseline resolution is 6.19 ± 0.13 eV. Right: Al Kα spectrum. Resolution is 6.38 ± 0.09 eV. The blue line shows the intrinsic profile of the Al Kα line complex.

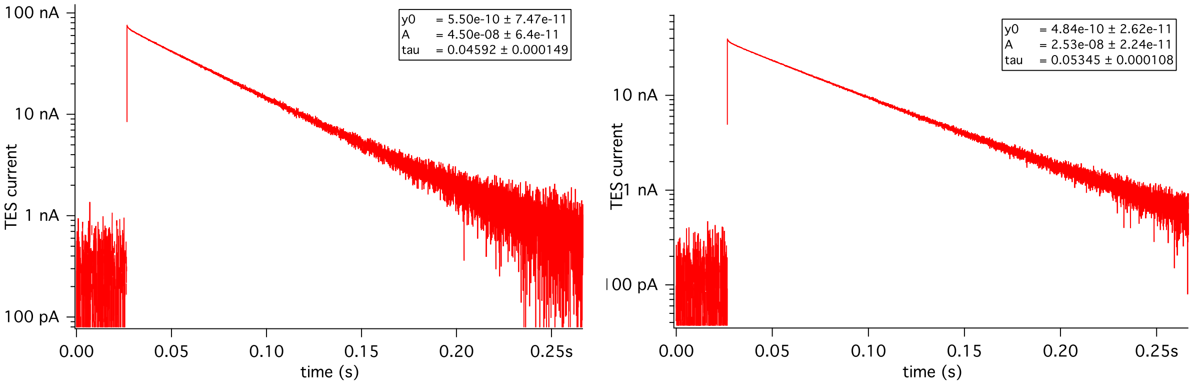

Figure 7.13: Average pulse shape at $T \approx T_c$, where $\tau_{eff} \approx \tau_{th}$ fit to single exponential to determine thermal decay time constant. Left: pixel 11. Right: pixel 22

capacity based on calculations from the literature, which is 2.85×10^{-12} J/K for the absorber and the TES combined.

A large excess heat capacity helps explain why the measured ΔE_{NEP} is worse than predicted by the model, even though the measured α_{IV} are quite high (we assumed $\alpha = 55$ for modeling based on our past experience with similar TES designs, but at 15% R_n we measured $\alpha_{IV} = 98.1$). One major source of uncertainty, however, is that we do not know β. As a further diagnostic, we can look at how α and β affect the pulse shape:

$$\alpha_\tau = [(\tau_0/\tau) - 1](GT_c/P_b)(1 + \eta + \beta)/(1 - \eta) \tag{7.1}$$

where $\eta \equiv R_{sh}/R$. Returning to our model, we can fix the heat capacity and thermal conductivity to the measured values for pixel 22, and set $\alpha = \alpha_{IV} = 98.1$ at 15% R_n. Fitting to the pulse shape, we find that $\beta = 1.86$ (see Fig. 7.14). Looking at the pulse shapes, we see that the measured average pulse begins to deviate from a single decay time constant at a few tens of milliseconds. The agreement of the modeled and measured noise is good at high frequency, but poor below 1 kHz. The modeled $\Delta E_{NEP} = 5.54$ eV, slightly better than what we observe (6.01 eV at 15% R_n). We can also try allowing the model to fit for both α and β, which yields a best fit of $\alpha = 38.9$ and $\beta = 0$. Then, the modeled $\Delta E = 6.06$ eV, closer to what we observe. However, referring to Figure 7.15, we see that the pulse shapes still differ at long times, and the agreement between modeled and measured noise is poor.

With so many parameters in the model and the uncertainty in deriving some of the measured quantities, like α and C, it is perhaps not surprising that we cannot produce exact agreement. In particular, the presence of a second time constant in the average pulse shape may indicate that the large measured heat capacity may not be a single lumped element, but the excess may in fact be a "hanging" heat capacity connected to the rest of the device by an unknown conductivity. Since our model treats the absorber as a single heat capacity, this may explain some of the discrepancy between the fits and the data. Still, we can draw some general conclusions from comparing the data and models for this pixel. We observe heat capacity well in excess of calculations based on the amount of gold in the absorber and the size of the TES. This excess heat capacity reduces the pulse height; if the heat capacity of the absorber was consistent with the literature value for gold, the model would predict a 70% larger pulse. The decoupling of the excess heat capacity implied by the tail in the pulse shape may also lead to internal fluctuation noise which is not accounted for in the model. This may help explain the excess mid-band noise observed (see Fig. 7.14). Improving the thermal model to determine the size of the decoupled excess and how it is thermally connected to the rest of the device may allow us to identify and eliminate the excess in future devices.

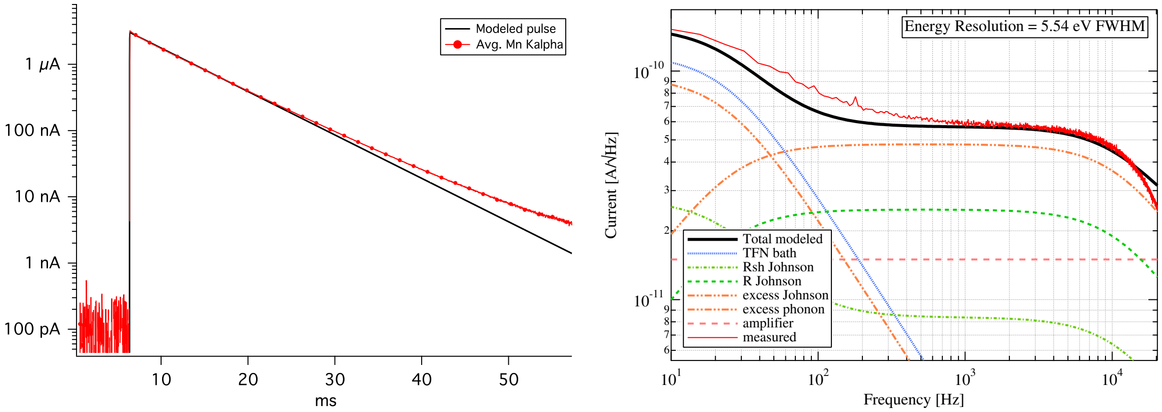

Figure 7.14: Modeled noise and Mn Kα pulse shape for pixel 22 using measured values of C, G$_{bath}$, T_c, and α_{IV}, with $\beta = 1.864$, for $T_b = 55$ mK and biased at 15% R_n. For comparison, the average pulse shape and noise from Fig. 7.6 are also shown. Left: Measured and modeled Mn Kα pulse shapes Right: Measured and modeled noise spectra.

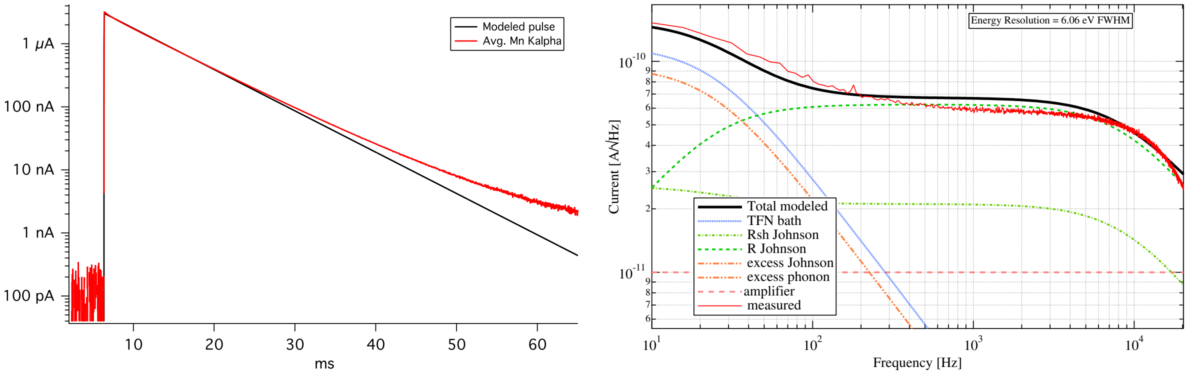

Figure 7.15: Modeled noise and Mn Kα pulse shape for pixel 22 using measured values of C, G$_{bath}$, T_c for $T_b = 55$ mK and biased at 15% R_n. Fit to pulse shape (see Eqn. 7.1) finds $\alpha = 38.9$ and $\beta = 0$. For comparison, the average pulse shape and noise from Fig. 7.6 are also shown. Left: Measured and modeled Mn Kα pulse shapes Right: Measured and modeled noise spectra.

7.2 Small pixels with absorber to TES stem variations: MXW1j

The second array of pixels tested from the MXW1 wafer was chip j, a 4 × 6 array of 240 μm × 240 μm suspended absorbers with modifications made to either the superconducting leads or to the stem that couples the absorber to the TES. These features affect the transition shape (α and β) and magnetic field sensitivity, so we hoped to find a device that outperformed the standard T-stem design used for most of the pixels on MXW1.

Figure 7.16 shows an illustration of the six device geometries tested. Pixel L1c3, with a T-stem and sharp bends in the superconducting leads, represents the "conventional" design. The stem and leads are identical to GSFC's detectors designed for Micro-X, and to the devices coupled to suspended absorbers on the rest of the MXW1 wafer. The Micro-X devices were found to have lower α compared to similar TESs (devices with the same dimensions and T-stem) that GSFC has made in the past. So, changes were made to try to identify what was different about the Micro-X design that contributed to its relatively poor performance. For example, pixel L1c2 was given leads with rounded corners, like some pixels GSFC had designed for IXO/Athena, as opposed to sharp corners (the Micro-X design). On the other four pixels we replaced the T-stem with a different stem design and a thinner extension of the normal metal bank. Having less surface area of normal metal on top of the bilayer should increase α. GSFC has tried the 2 J-stem design (L1c1) in the past, and found that it did have higher α (and consequently faster decay times) than the T-stem design, and better energy resolution for bias points above 15% R_n (Smith et al., 2014). We included two slight variations on this design that had only a single J-stem (L2c2, L2c3). Finally, pixel L2c3 has only a single 7 μm square post connecting the bank to the TES. Small posts like this have been used successfully in

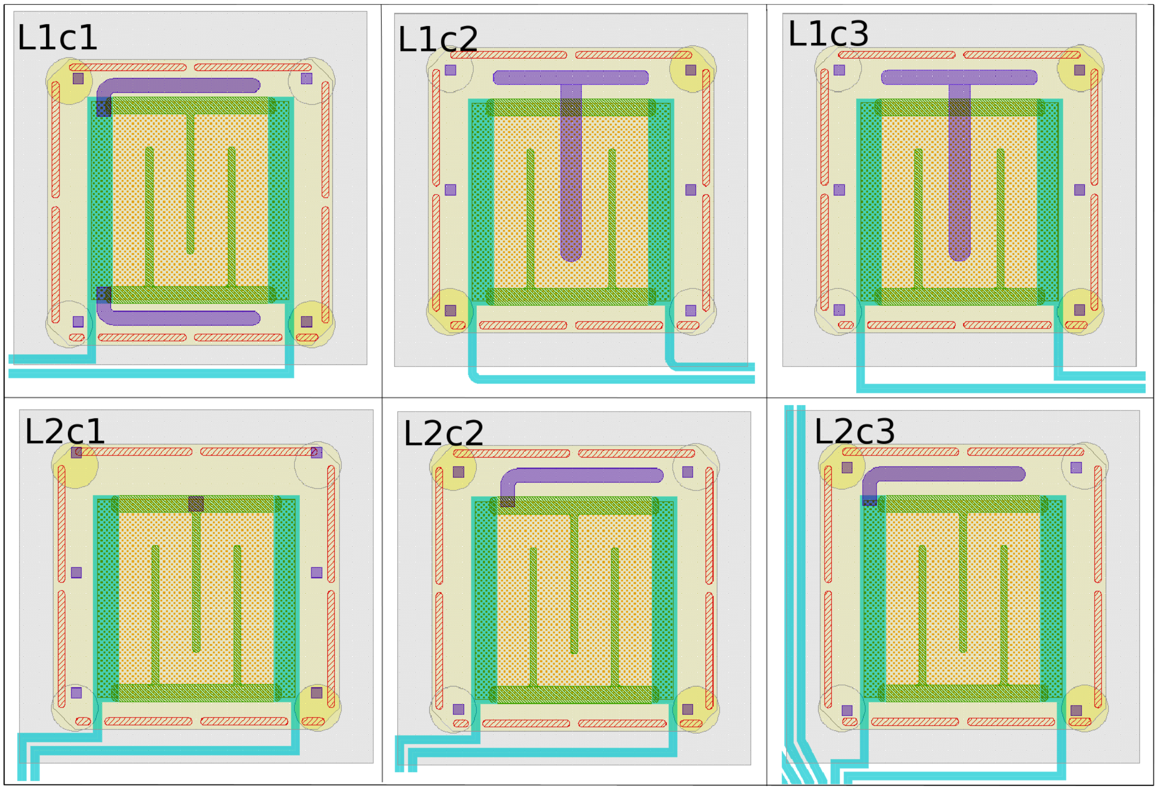

Figure 7.16: MXW1 chip j, illustration showing pixel geometries tested. All pixels had 240 × 240 × 0.5 μm suspended absorbers (gray, shown semi-transparent). The front etch (red) removed approximately 90% of the perimeter of the nitride membrane (yellow). Absorber support stems are shown in purple. Top left: L1c1, 2× J-stem, making thermal contact with a superconducting lead. Top center: L1c2, T-stem with rounded leads. Top right: T-stem, "standard" design. Bottom left: L2c1, 7 μm × 7 μm square stem, centered on normal metal bank. Bottom center: L2c2, single J-stem contacting bank. Bottom right: L2c3, single J-stem contacting lead.

high-α devices with a much smaller, 35 μm × 35 μm TES (Bandler et al., 2013).

The tests were conducted at GSFC in September, 2014 and used the same cryostat and readout electronics as the MXW1d run. The transition temperature measured for all six pixels was about 100 mK, with the exception of pixel L2c3 (see Table 7.3). Upon measuring the applied field needed to null the trapped flux, we noticed that it was about an order of magnitude higher than we observed in the previous run. A larger trapped field

Pixel	stems	B$_{app}$ (μT)*	T_c*	T_c w/ B$_{app}$*	B$_{app}$	T_c	T_c w/ B$_{app}$
L1c1	2×J, on leads	12.77	97.6	100.7	10.43	98.5	101.5
L1c2	T, round leads	6.95	99.0	99.9	3.79	99.4	99.8
L1c3	T, sharp leads	13.08	98.3	100.0	9.48	100.25	100.8
L2c1	7 μm square	7.02	85.8	88.5	N/A	N/A	N/A
L2c2	J, on bank	13.15	88.9	100.6	10.43	98.9	101.0
L2c3	J, on lead	10.05	91.1	96.4	7.46	93.8	97.0

Table 7.3: MXW1j pixel geometries tested. B$_{app}$ (μT) is the field that is observed to maximize T_c (mK). It is assumed to be the field that nullifies the trapped flux. It is calculated based on the geometry of the field coil. Due to the high level of trapped flux observed, we chose to warm the cryostat to room temperature and re-cool. Columns with an asterisk (*) denote data taken on the initial cooldown. For pixel L2c1, "N/A" indicates that we were unable to measure T_c.

is more difficult to cancel precisely, and may affect the performance of the detector. We made measurements of the TES current as a function of the applied field, and collected IV curves for one pixel (L1c2), then allowed to cryostat to warm up to room temperature. We cooled the cryostat again, being careful to arrange the μ-metal can and Metglas shield in the same configuration that was used for the MXW1d run. After re-cooling the cryostat we checked the trapped flux, and found that it was smaller by 25-50%. All of the data presented were collected after the second cool down, except where noted.

Figures 7.19 and 7.20 show IV curve data for pixels L1c2 and L1c3, respectively. The applied magnetic field was set to null the trapped field for each pixel according to the values in Table 7.3. The IV curves have more structure than was observed on other arrays from the MXW1 wafer, which shows up as prominent bends or kinks in the resistance versus temperature curve. The thermal conductivity of these pixels should be identical, and based on the perforations and stem pattern we expect $G(0.1K) = 58$ pW/K. Using the IV curves at a range of bath temperatures, we find $G(0.1K)$ is 55.9 ± 12.6 pW/K for L1c2 (Fig. 7.17), and 64.3 ± 22.6 pW/K for L1c3 (Fig. 7.18), consistent with expectations.

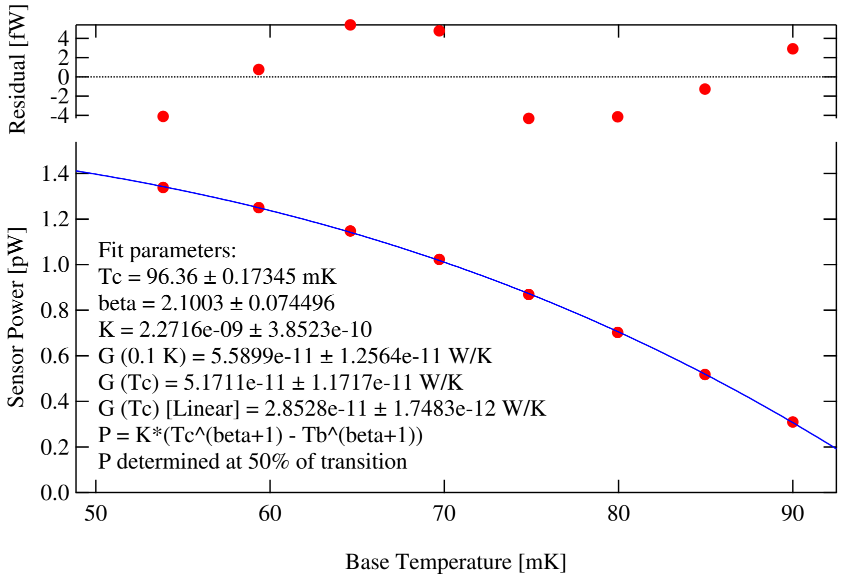

Figure 7.17: Pixel L1c2 (T-stem rounded leads) dissipated power at 50% R_n as a function of bath temperature. Blue line shows a fit to $P = K(T_c^n - T_b^n)$, where T_c is the temperature at 50% R_n. Derived thermal conductivity between the sensor and the bath is $G(0.1K) = 55.9 \pm 12.6$ pW/K, $n = 3.10 \pm 0.07$.

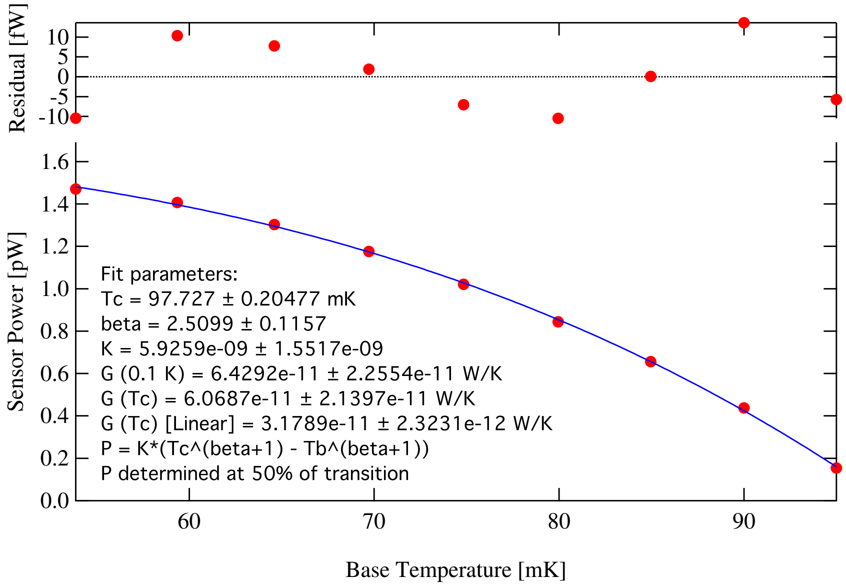

Figure 7.18: Pixel L1c3 (T-stem sharp leads) dissipated power at 50% R_n as a function of bath temperature. Blue line shows a fit to $P = K(T_c^n - T_b^n)$, where T_c is the temperature at 50% R_n. Derived thermal conductivity between the sensor and the bath is $G(0.1K) = 64.3 \pm 22.6$ pW/K, $n = 3.51 \pm 0.12$.

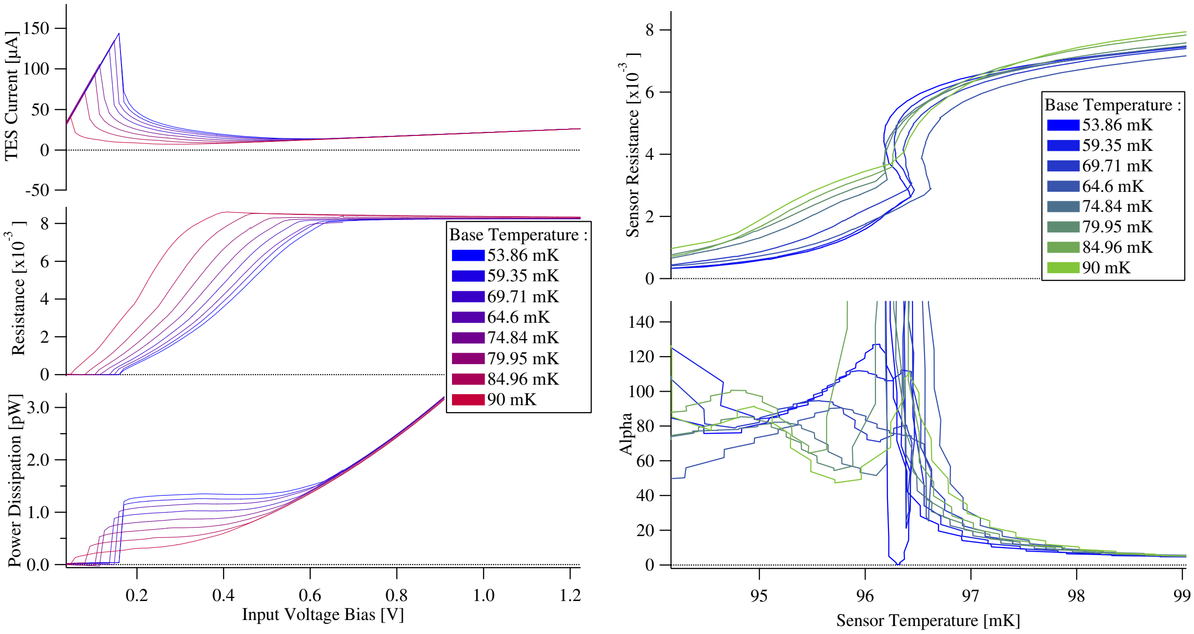

Figure 7.19: Pixel L1c2 (T-stem, rounded leads). A voltage (V_{in}) is applied to the bias circuit through a large input resistor ($R_{in} = 1.095\ k\Omega$), with a known shunt resistance (($R_{SH} = 0.2$ mΩ)) Left: TES current (top), resistance (middle) and dissipated power (bottom) as a function of V_{in}. Right: TES resistance (top) and sensitivity α (bottom) as a function of TES temperature, determined using the measured thermal conductivity and power dissipation.

The IV curve data for pixel L1c2 was acquired before the warm up and second cooldown, but data from a sparse sampling of bath temperatures acquired after the second cooldown yielded the same value for $G(0.1K)$.

The pixel-to-pixel geometry differences are expected to influence the performance of the detectors in two important ways. First, the arrangement of normal metal features on or near the TES is known to affect the shape of the R(I,T) surface and suppress excess noise. Since it is difficult to predict α and β *a priori*, we can try to optimize the design experimentally. Second, the geometry of the device (such as the location of the current-carrying leads) affects its sensitivity to external magnetic fields and changes the self-fielding. The presence of a magnetic field changes the critical current, and consequently

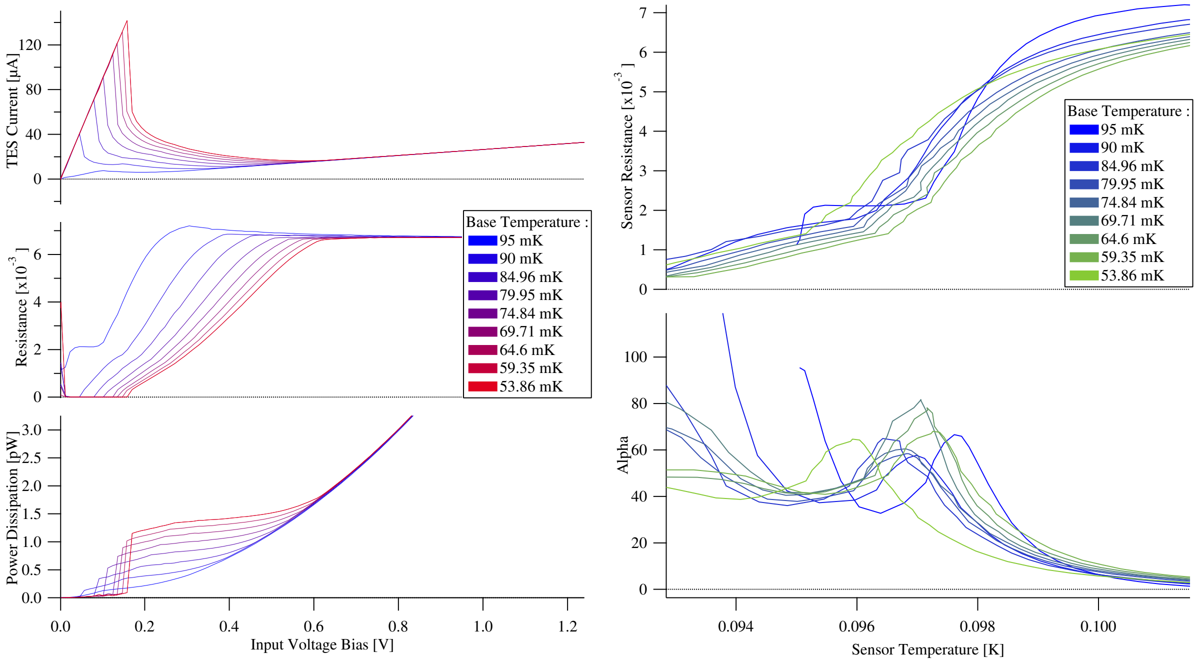

Figure 7.20: Pixel L1c3 (T-stem sharp leads) A voltage (V_{in}) is applied to the bias circuit through a large input resistor ($R_{in} = 1.095\ k\Omega$), with a known shunt resistance (($R_{SH} = 0.2$ mΩ)) Left: TES current (top), resistance (middle) and dissipated power (bottom) as a function of V_{in}. Right: TES resistance (top) and sensitivity α (bottom) as a function of TES temperature, determined using the measured thermal conductivity and power dissipation.

α and β. Although we can eliminate the effect of a trapped field by applying an external field to cancel it, this may prove ineffective on a single-pixel scale if the field is time varying, or on the array scale if the field is spatially varying, even if it is static. We can examine these effects by measuring the pulse shape, noise spectrum, energy resolution, and α throughout the transition both in the zero-field case and as a function of applied field. All of these data were obtained with $T_{bath} = 55$ mK, unless otherwise noted.

The pixel we studied in greatest detail was L1c2. This pixel has a T-stem to thermally connect the absorber and TES, which is identical to the T-stems used on all other suspended absorber designs on the MXW wafer. The leads extend $\sim 50\ \mu$m from the edge of the TES, then make an L-shaped bend to route the leads to the bond pads. In the conventional design, used over most of the wafer, the bends in the leads make a sharp corner, whereas for this pixel they are rounded with an 8 μm bend radius. Figure 7.21 shows the average Mn Kα pulse shape and noise spectrum as a function of bias point (R/R_n) for applied field $B = 3.8$ μT, which was determined to be the field that cancels the trapped field from T_c measurements (see Table 7.3). As in the previous section, we use the NEP to derive an energy resolution at each bias point. Referring to Table 7.4, we see that above 25% R_n, the kink in the $R(T)$ curve (see Fig. 7.19) results in very large α_{IV}. Above 25% R_n, the pulse decays exhibit more than one time constant and appear to have a "peaky" structure near the rise, supporting the idea that the structure observed in the IV curves is real, rather than an artifact introduced by the measurement. Typically TES performance is poor in the vicinity of kinks or bends in the transition, and indeed here the pulse height and energy resolution are observed to decay as the bias point is increased.

Also striking is the poor energy resolution. These TESs are coupled to 240 μm × 240 μm absorbers, so the absorbers have about 7% the heat capacity of the large devices from MXW1d (this ratio is the same for both the measured and expected heat capacity). Those devices had $\Delta E_{NEP} \sim$ 6-6.5 eV. The transition temperatures are the same to within a few mK. For pixels L1c2 and L1c3 the TES geometry is identical to that of the MXW1d pixels, so we might expect similar α. So, if these small pixels had the same TES sensitivity and excess heat capacity that we measured for the large pixels in MXW1d, we would expect them to have 1.6-1.75 eV resolution, versus the observed 2.5 eV. It appears, then, that α for this detector may be significantly different than expected. Referring to Table 7.4, we see that α_{IV} for L1c2 is, generally, much lower than was measured for the 890 μm × 890 μm pixels from MXW1d (see Section 7.1), causing a large reduction in the signal.

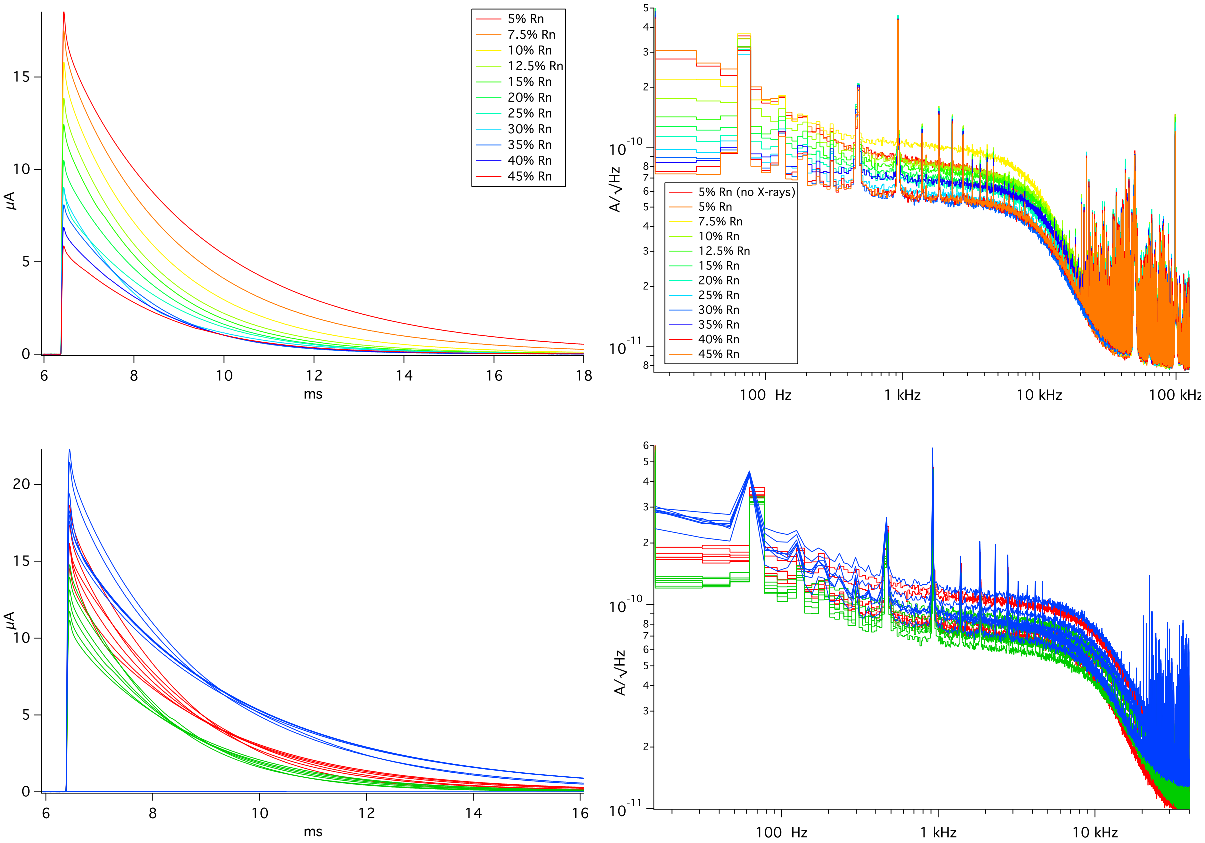

Figure 7.21: Pixel L1c2 (T-stem, rounded leads) , Mn Kα X-rays, T_b = 55 mK. Top, left: Average pulse shape as a function of bias point for B_{app} = 3.8 μT, the field determined to maximize T_c. Top, right: Average noise as a function of bias point for B_{app} = 3.8 μT. Bottom, left: Average pulse shape at I_{bias} =5% R_n (blue), 10% R_n (red) and 15% R_n (green) with varying applied field. Bottom, right: Average noise at I_{bias} =5% R_n (blue), 10% R_n (red) and 15% R_n (green) with varying applied field.

bias (% R_n)	pulse height (μA)	τ (ms)	α_{IV}	ΔE_{NEP} (eV)
5	18.51	3.42	38.5	2.54
7.5	17.5	2.8	50.1	2.83
10	15.78	2.28	62.6	2.76
12.5	13.91	2.02	67.5	2.82
15	12.43	1.89	67.5	2.89
20	10.48	1.85	68.2	3.09
25	9.02	1.99	60.4	3.28
30	9.01	2.12	168	3.11
35	8.08	1.58	518	3.64
40	6.85	1.82	430	3.73
45	5.85	2.05	135	4.12

Table 7.4: MXW1j pixel L1c2 pulse height, decay time, and energy resolution (derived from NEP) as a function of bias point at constant applied B = 3.8 μT. The column α_{IV} gives α values derived from IV curves (see Fig. 7.19). If this detector had $\alpha \approx 100$ and excess heat capacity like the pixels tested from MXW1d, the model predicts $\Delta E_{NEP} = 1.6$ eV. If $\alpha = 55$, like we assumed when designing the devices, we expect $\Delta E_{NEP} = 2.15$ eV.

To compute C, we use the decay time of the pulse at $T \approx T_c$, shown in Fig. 7.22. Unfortunately, this pulse shape also shows a great deal of structure, with several different time constants appearing over the duration of the decay. Fitting a time constant to two different parts of the decay gives 6.16 ms (highlighted in blue) and 16.4 ms (highlighted in black). Using the thermal conductivity measured previously, we can derive a heat capacity of 0.354 pJ/K or 0.942 pJ/K for the short and long time constants, respectively. Based on the amount of metal in the bilayer and absorber, the calculated heat capacity for a pixel this size is 0.28-0.35 pJ/K, depending on what we assume for the heat capacity of the TES in the transition. Given that we observed at most a 70% excess heat capacity for the MXW1d pixels and this chip was taken from the same wafer, 0.354 pJ/K seems more consistent with expectations.

The relatively large trapped field that was observed in this run is a concern, so we

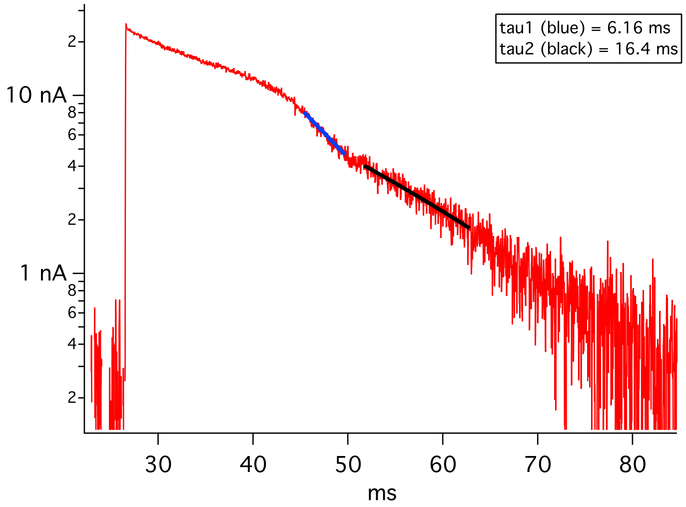

Figure 7.22: Pixel L1c2 Average Mn Kα pulse shape at $T_b \approx T_c$ (where $\tau_{eff} \approx \tau_0 \equiv C/G$) fit to single exponential to determine thermal decay time constant.

turn to examining the effect of an externally applied magnetic field on the detector performance. The resolution may improve if the 3.8 μT field that we applied did not adequately cancel the trapped flux, or if a different applied field corresponds to a more optimal area of R(I,T,B) parameter space (e.g. higher α and lower β). To investigate these effects, we apply an approximately constant voltage bias to the TES and vary the applied field. This does not correspond to a constant current in the TES, as can be seen in Figure 7.23, which shows the change in TES current as a function of the applied field. Changing the applied field changes the resistance of the TES and the shape of the R(I,T) surface. The curves are labeled by the "zero-field" bias point (i.e. R/R_N for the applied I_{bias} at $B_{app} = 3.8$ μT, which we will refer to from now on as B_0). Curves labeled with negative numbers (e.g. -15% Rn) indicate that the direction of the bias current is reversed. Referring to Fig. 7.23, we see that the 15% R_n curve (purple) corresponds to a TES current of 34.3 μA at B_0. Changing the applied field from -10 μT to 0 μT changes the TES current by about 12 μA. Smith et al. (2013) show that, in the weak link model, a net applied field suppresses the critical current, T_c, and α. For constant bias current, we therefore expect an increase in resistance as the applied field increases. So, the maximum of the TES current versus field curve should correspond to $B_{net} = 0$, and the TES is likely to have better energy resolution here. The field that we determined should cancel the trapped flux (B_0) is close to the maximum of the ΔI_{TES} versus field curve, so it is likely close to the net zero field condition.

Figure 7.23 also shows ΔE_{NEP} as a function of applied field plotted along with the ΔI_{TES} curve for three different bias points. Looking at the $R/R_n = 15\%$ curve (purple), we see that $\Delta E = 2.89$ eV at B_0. At $B_{app} = 0.6\ \mu$T we find $\Delta E = 2.68$ eV. At this applied field, the TES resistance has increased to that $R/R_n = 15.6\%$. For such a small change in resistance, we might expect little change in the resolution, and if anything, based on Table 7.4 we would expect the resolution to worsen as the TES resistance increases. So we can conclude that varying the applied magnetic field is changes the shape of the R(I,T) surface, and consequently can improve the energy resolution. However, it is surprising that the best resolution does not coincide with the maximum of the TES current versus applied field curve, where we assume $B_{net} = 0$ and the α is expected to be the largest.

Ultimately, we would like to use this information to determine an optimal bias point for the detector. Considering both bias point and applied field, the available parameter space is much too large to map exhaustively. This will be especially true when we are faced with tuning multiple pixels, or eventually an entire array. One reasonably reliable predictor for energy resolution is the pulse height. Figure 7.24 plots ΔE_{NEP} as a function of pulse height for constant bias voltage with varying field (left), and constant field for varying bias point (right). Though there is detailed structure, particularly when varying the field, in general larger pulses correspond to better resolution. Figure 7.24 also shows that pulse heights are generally larger and ΔE_{NEP} is better at $B_{app} = 0.6\ \mu$T than at

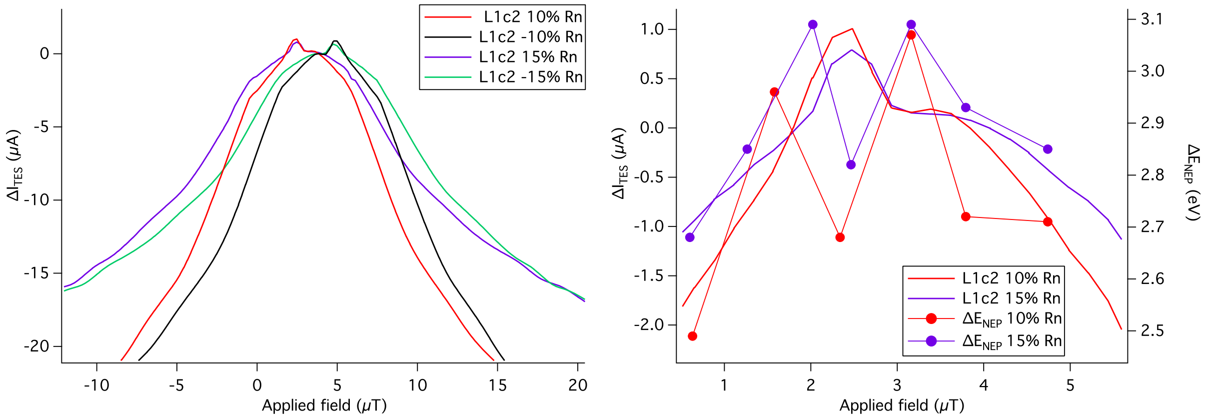

Figure 7.23: Pixel L1c2 (T-stem, rounded leads) Left: change in TES current versus applied field at $T_b = 55$ mK for different voltage biases. Labels indicate bias point at $\Delta I_{TES} = 0$. Curves labeled with negative numbers (e.g. -15% Rn) indicate that the direction of the bias current is reversed. Right: ΔE_{NEP} plotted along with ΔI_{TES} versus applied field.

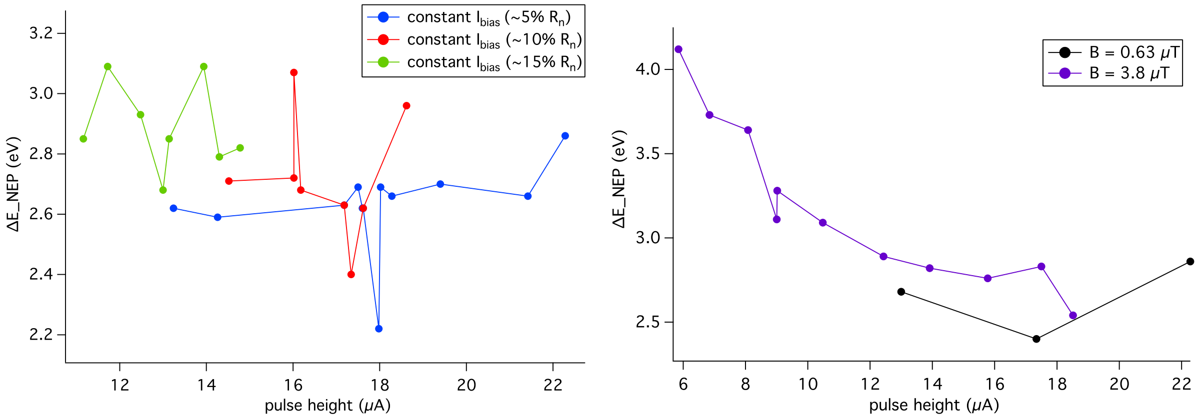

Figure 7.24: Pixel L1c2 (T-stem, rounded leads) ΔE_{NEP} as a function of Mn Kα X-ray pulse height. Left: Constant bias point (R/R_n) and varying applied field. Right: Constant applied field, varying bias point.

B_0. It is may be that $B_{app} = 0.6$ μT is actually closer to net zero magnetic field, which is expected to correspond to larger α and perhaps could account for the slight improvement in resolution. This emphasizes the need for good magnetic shielding or a detector that is not sensitive to small changes in magnetic field.

Pixel L1c3 is nearly identical in design to L1c2; the difference between the two pixels lies in the superconducting leads. Whereas pixel L1c2's leads are rounded where they bend to route away from the TES, pixel L1c3's leads have a sharp corner. This sharp corner design was used on MXW1 chips d and D, and on devices designed for Micro-X. GSFC has made identically sized TESs in the past for IXO/Athena, but with rounded leads. Since those TES tended to have higher α than the Micro-X devices, we wanted to investigate whether or not the lead routing contributed to the difference. We found that L1c3 had very similar energy resolution to L1c2 (compare Table 7.4 and 7.5). The best measured ΔE_{NEP} was the same for both pixels (2.54 eV). However, contrary to what we had hoped, α_{IV} was generally worse for L1c3 throughout the transition. The applied field necessary to cancel the trapped field was significantly higher for L1c3 than in L1c2; subsequent data were collected with $B_{app} = 9.47\ \mu$T. The transition features a prominent kink around 20-25% R_n (see Fig. 7.20), which results in a distorted pulse shape and corresponding degradation of the energy resolution (see Fig. 7.25 and Table 7.5). Like L1c2, the pulse shape at $T \approx T_c$ has multiple time constants, which makes determining the thermal time constant and heat capacity difficult. As before, we fit a short time constant of 6.37 ms ($C = 0.427$ pJ/K) and a long time constant of 11 ms ($C = 0.737$ pJ/K).

The change in TES current as a function of applied field for constant bias current is shown in Figure 7.26. It is qualitatively similar in appearance to data from L1c2, though the energy resolution appears to improve for fields slightly higher than the canceling field we measured by maximizing T_c ($B_{app} = 9.47\ \mu$T). There is also a correlation between pulse height and energy resolution (see Fig. 7.27), and there is no obvious correlation between the field strength and the resolution for a given pulse height.

Three of the pixels tested (L1c1, L2c2, and L2c3) used J-shape stems to connect the TES and absorber. Since the J-stems only overlap the bank or leads of the TES,

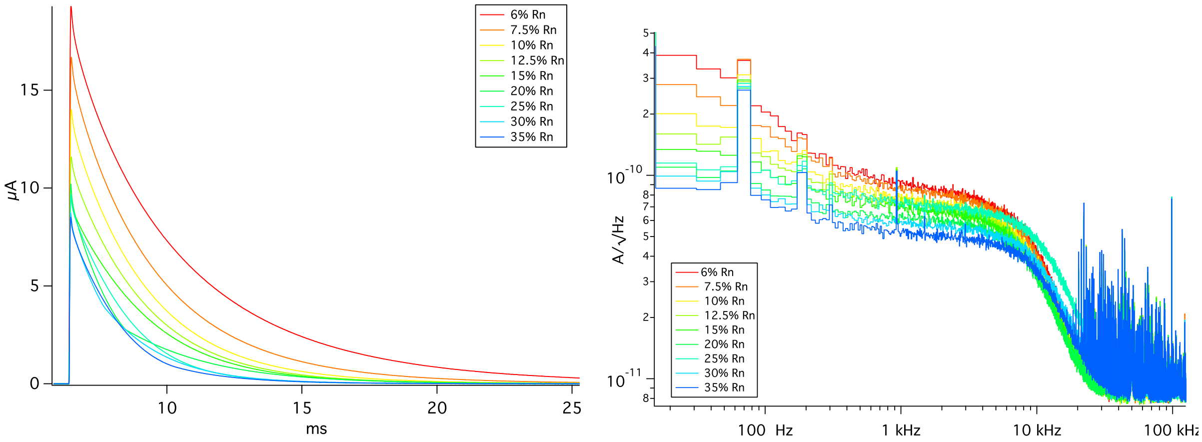

Figure 7.25: Pixel L1c3 (T-stem, sharp leads), Mn Kα X-rays, T_b = 55 mK. Left: Average pulse shape as a function of bias point for B_{app} = 9.48 μT, the field determined to maximize T_c. Right: Average noise as a function of bias point for B_{app} = 9.48 μT.

bias (% R_n)	pulse height (μA)	τ (ms)	α_{IV}	ΔE_{NEP} (eV)
6	19.29	4.26	45.2	2.54
7.5	16.68	3.25	44.9	2.65
10	14.00	2.75	43.0	2.67
12.5	11.60	2.61	39.9	2.9
15	9.50	2.69	38.9	3.14
20	10.22	3.48	46	2.92
25	9.68	1.90	54.3	3.29
30	8.74	2.23	61.6	3.22
35	8.51	2.15	64.5	2.92

Table 7.5: MXW1j pixel L1c3 pulse height, decay time, and energy resolution (derived from NEP) as a function of bias point at constant applied B = 3.8 μT. The column α_{IV} gives α values derived from the IV curves (see Fig. 7.20).

a normal metal stripe is added perpendicular to the flow of current to compensate for the absence of the overlapping T-stem (see Fig. 7.16). We might expect these designs to have slightly higher α, owing to the smaller area of the stripe relative to the T-stem. These designs performed poorly relative to the T-stem pixels. Pixel L1c1 had two J-stems making thermal contact to the TES on the lead, then extending parallel to the normal

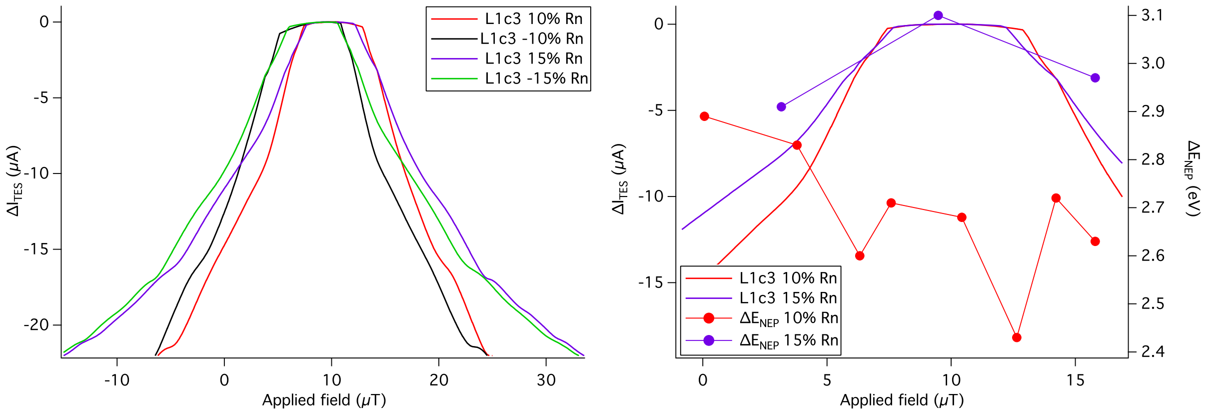

Figure 7.26: Pixel L1c3 (T-stem, sharp leads) Left: change in TES current versus applied field at $T_b = 55$ mK for different voltage biases. Labels indicate bias point at $\Delta I_{TES} = 0$. Curves labeled with negative numbers (e.g. -15% Rn) indicate that the direction of the bias current is reversed. Right: ΔE_{NEP} plotted along with ΔI_{TES} versus applied field.

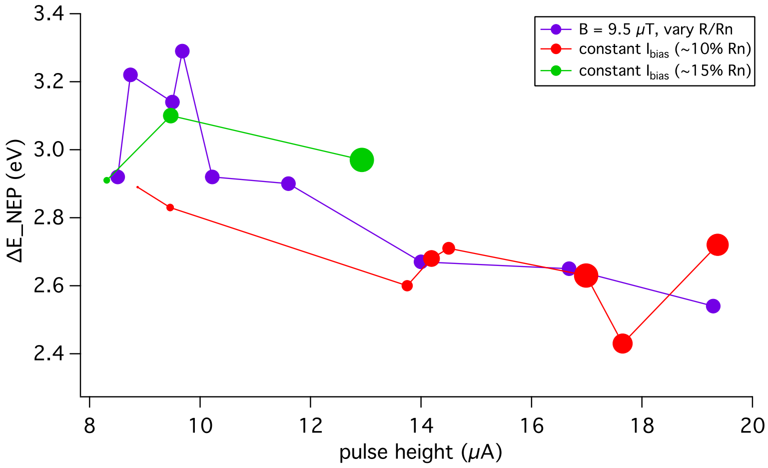

Figure 7.27: Pixel L1c3 (T-stem, sharp leads) ΔE_{NEP} as a function of Mn Kα X-ray pulse height, with point sizes scaled by the magnitude of the applied field.

metal bank and direction of current flow. The peaks, kinks and bends that appear in the average pulse shapes (Fig. 7.28) for several bias points indicate a great deal of structure in the shape of the transition. The energy resolution ranged from 2.5 to 4.4 eV, indicating that the performance is not, in general, better than the T-stem designs. There is clear

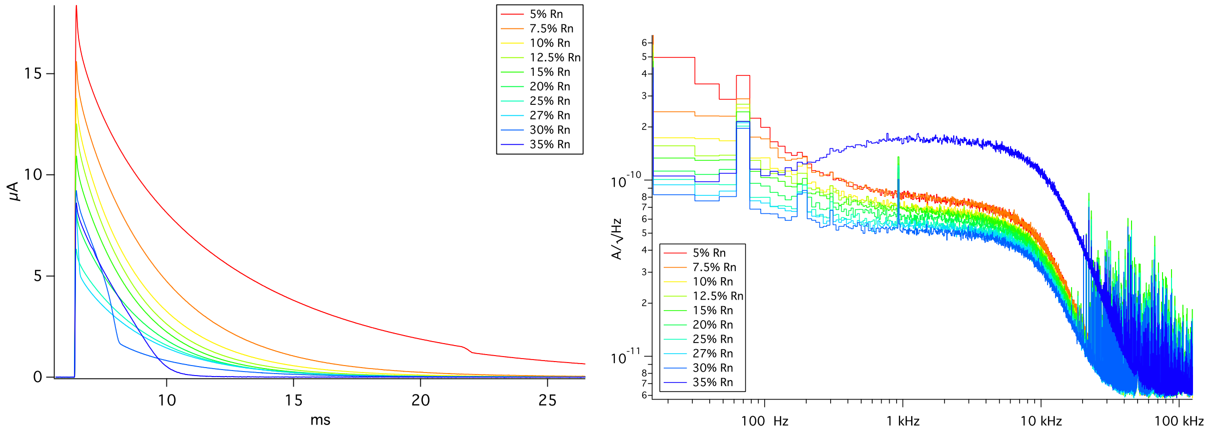

Figure 7.28: Pixel L1c1 (2× J-stem, contacting leads) Mn Kα X-rays, T_b = 55 mK. Left: Average pulse shape as a function of bias point for B_{app} = 10.43 μT, the field determined to maximize T_c. Right: Average noise as a function of bias point for B_{app} = 10.43 μT.

degradation of the energy resolution away from the maximum of the I_{TES} versus applied field curve (Fig. 7.29), consistent with the expectation that large net field should suppress α. An Mn Kα X-ray spectrum is shown in Figure 7.30. The spectrum was acquired at R/R_n =15% and ΔE_{NEP} = 2.99 eV. Significant broadening is observed at the Mn Kα line, for which we fit $\Delta E = 4.47 \pm 0.18$ eV. Applying a 1 kHz low pass filter significantly improves the resolution, with $\Delta E = 3.43 \pm 0.15$ eV and a fitted baseline resolution of $\Delta E = 2.84 \pm 0.04$ eV.

The distorted pulse shapes and strong magnetic field dependence observed in L1c1 are observed to be even more prominent in the single J-stem pixels. Pixel L2c2 features a single J-stem that makes contact with the normal metal bank that runs along the TES. The TES current is a sharply peaked function of the applied field, and the energy resolution worsens dramatically away from the zero-field condition (Fig. 7.32). This may signify the appearance of kinks or bends in the superconducting transition when a net field is present. Figure 7.31 shows the average pulse shapes for three different bias currents and varying applied fields. At all bias currents, when the applied field best cancels the

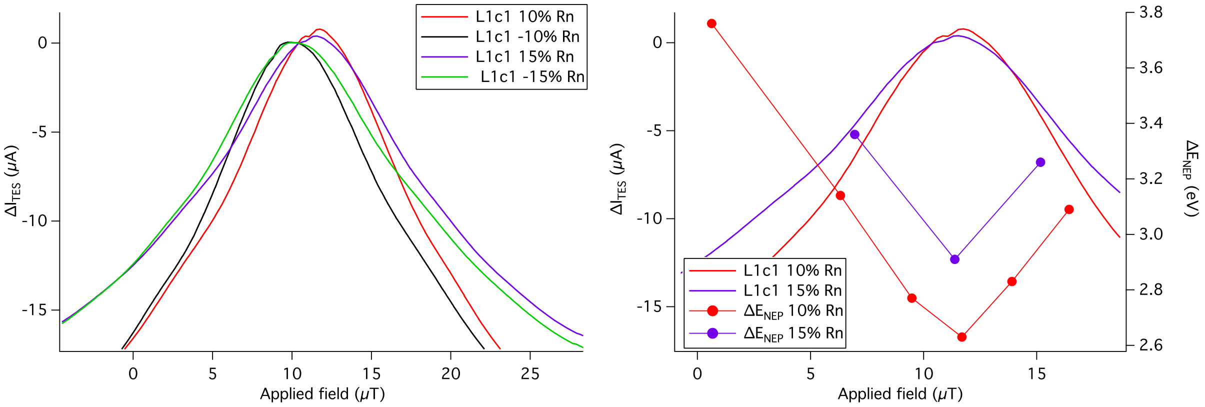

Figure 7.29: Pixel L1c1 (2× J-stem, contacting leads) Left: change in TES current versus applied field at $T_b = 55$ mK for different voltage biases. Labels indicate bias point at $\Delta I_{TES} = 0$. Curves labeled with negative numbers (e.g. -15% Rn) indicate that the direction of the bias current is reversed. Right: ΔE_{NEP} plotted along with ΔI_{TES} versus applied field.

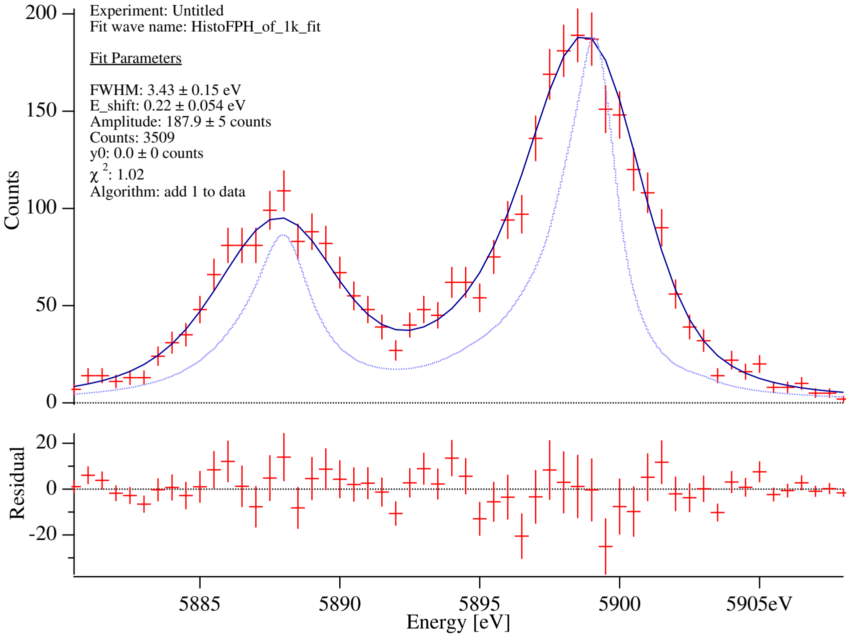

Figure 7.30: Pixel L1c1 (2× J-stem, contacting leads) Mn Kα X-ray spectrum, with TES biased at 15% R_n and $T_b = 55$ mK. A 1 kHz low pass filter was applied to the optimal filter template to reduce excess broadening. $\Delta E_{NEP} = 3.29$ eV, and the fitted Mn Kα resolution is 3.43 ± 0.15 eV. The blue line shows the intrinsic profile of the Mn Kα1,2 line complex.

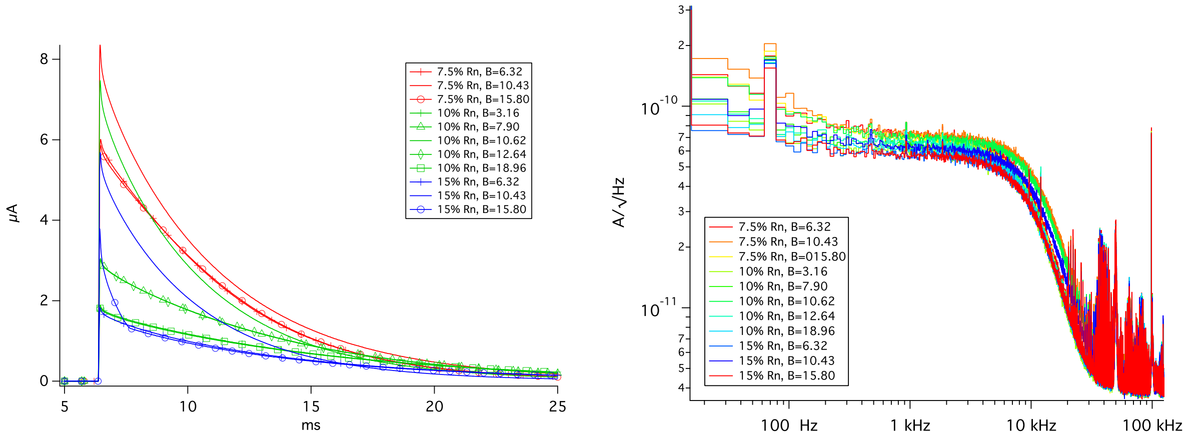

Figure 7.31: Pixel L2c2 (J stem, bank contact), Mn Kα X-rays, $T_b = 55$ mK. Left: Average pulse shape at I_{bias} =5% R_n (blue), 10% R_n (red) and 15% R_n (green) with varying applied field (labels give B_{app} in μT). Right: Average noise at I_{bias} =5% R_n, 10% R_n, and 15% R_n with varying applied field (labels give B_{app} in μT).

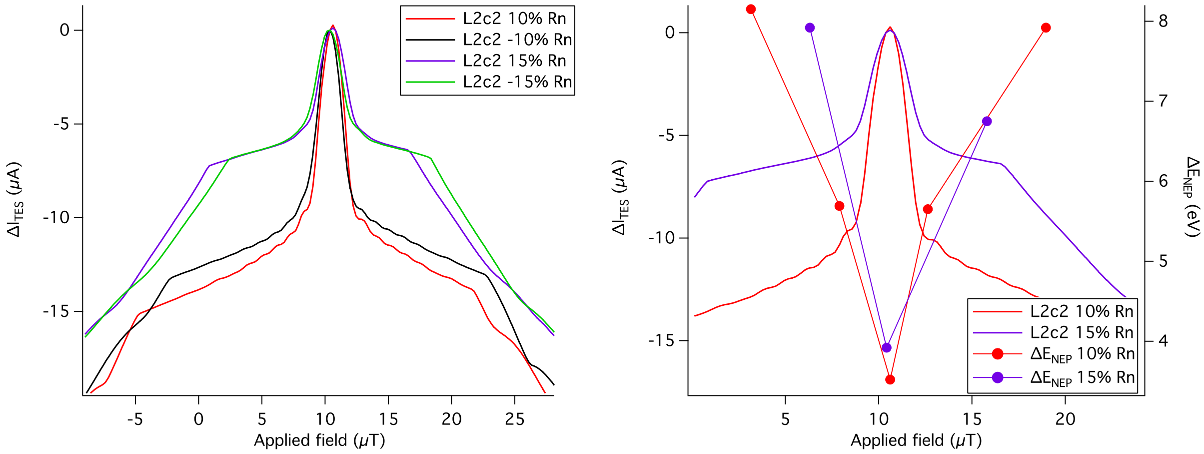

Figure 7.32: Pixel L2c2 (J stem, bank contact) Left: change in TES current versus applied field at $T_b = 55$ mK for different voltage biases. Labels indicate bias point at $\Delta I_{TES} = 0$. Curves labeled with negative numbers (e.g. -15% Rn) indicate that the direction of the bias current is reversed. Right: ΔE_{NEP} plotted along with ΔI_{TES} versus applied field.

trapped field, the pulses are larger, feature less kinks or bends, and appear closer to having a single decay time constant. An Mn Kα X-ray spectrum obtained at $B_{net} \approx 0$ and 15% R_n is shown in Figure 7.33.

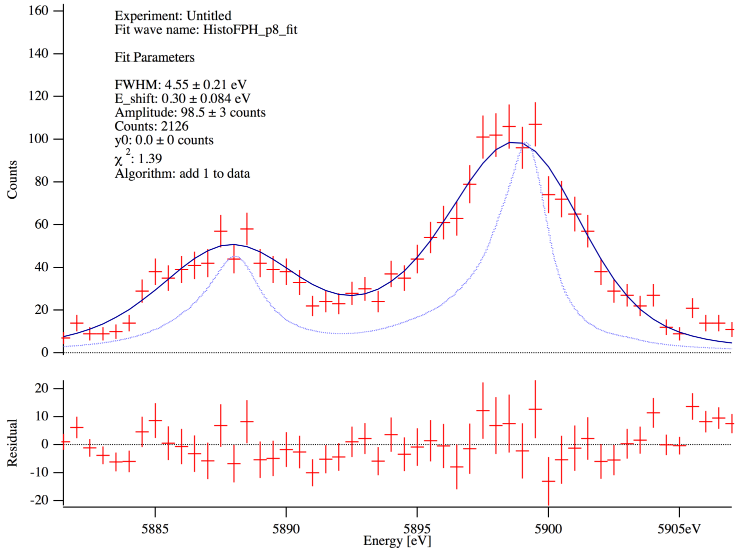

Figure 7.33: Pixel L2c2 (J stem, bank contact) Mn Kα X-ray spectrum with TES biased at 15% R_n and T_b = 55 mK, with a 5 kHz low pass filter applied to the optimal filter to reduce broadening. ΔE_{NEP} = 3.74 eV, and the fitted Mn Kα resolution is 4.55 ± 0.21 eV. The blue line shows the intrinsic profile of the Mn Kα1,2 line complex.

The other pixel with a single J-stem (L2c3, with the J-stem making contact with the lead rather than the bank of the TES) behaved very similar to L2c2. The TES current versus magnetic field curve appeared qualitatively similar, with a sharply peaked feature around what is presumably zero net field (Fig. 7.34). We measured ΔE_{NEP} for different 7.5%, 10%, and 15% R_n, and found the resolution was 9.4, 11.1, and 10.3 eV respectively.

The last pixel, L2c1, had a single 7 μm × 7 μm square stem in the center of the bank. Although time constraints prevented a thorough investigation of this pixel, the limited data available appeared promising. The TES current as a function of applied field curve has much broader peak than the single J-stem pixels (Fig. 7.34, right). A small sampling of energy resolution versus bias point ranged from ΔE_{NEP} = 2.24-2.93 eV, comparable to the best resolution achieved by the two T-stem designs, indicating that this geometry may warrant further investigation.

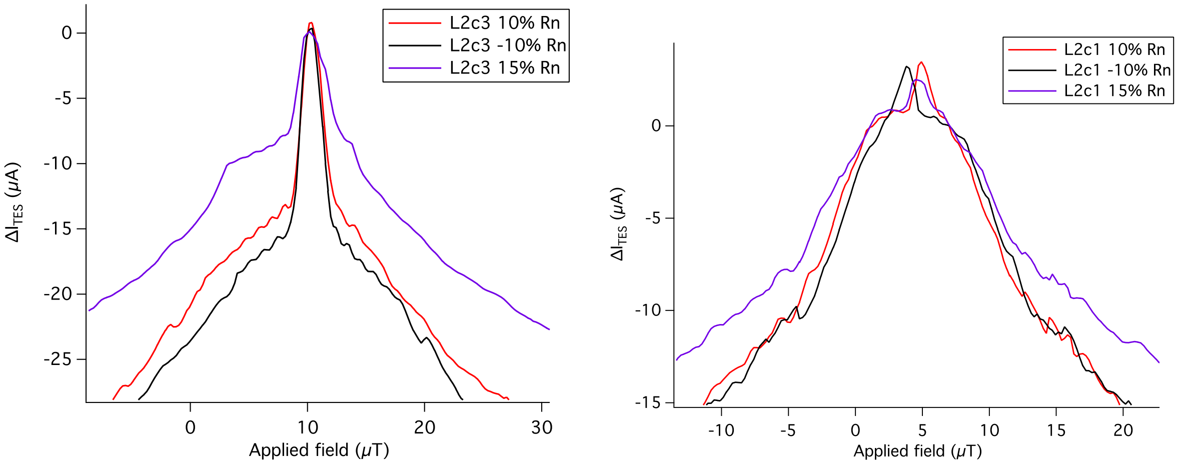

Figure 7.34: Change in TES current versus applied field at $T_b = 55$ mK for different voltage biases. Labels indicate bias point at $\Delta I_{TES} = 0$ Curves labeled with negative numbers (e.g. -15% Rn) indicate that the direction of the bias current is reversed. Left: L2c3 (J stem, lead contact). Right: L2c1 (7 μm square stem)

On the whole, the pixel-to-pixel differences observed in this run are difficult to interpret, and it may not be possible use the results from this array to successfully inform future designs without a better understanding of the poor performance of these pixels relative to other chips from the same wafer. For example, the poor performance of the single J-stem pixels was unexpected, given some success using them in past experiments by GSFC (Smith et al., 2014). And, compared to the other the MXW1d array (890 × 890 × 0.5 μm absorbers), these pixels showed poor α_{IV} , even for pixel L1c3, where the TES geometry was identical to the MXW1d pixels. The devices also had more structure in the IV curves, leading to peaks, steps, and kinks in the X-ray pulse shapes. It is not clear what is to blame for these differences, and we are investigating possible causes in the mask layout or during the fabrication process.

Chapter 8

MXW1D: coplanar absorber geometry

8.1 Coplanar absorbers

Despite the generally low yield for pixels with coplanar absorbers on MXW1, some of the pixels with small absorbers survived the fabrication process. Chip D, a 12 × 12 array of coplanar pixels with absorber sizes from 350-765 μm, was tested at Goddard in September, 2014. The cryostat used for this test run was also a liquid helium cooled ADR, but it is equipped with a slightly different SQUID readout. The two-stage SQUID readout is designed for multiplexing. Eleven input SQUIDs, each coupled to a TES, can be addressed individually and read out by a single SQUID array. There are two SQUID arrays, for a total of 22 readout channels. In multiplexed mode, the array cycles through the input SQUIDs, taking a single time sample from each in turn. However, in this case we did not need the multiplexing capability, so the array was used to address a single input channel at a time.

Upon cooldown, one of the SQUID arrays was not responding to signals sent through its feedback coil. Unfortunately, this prevented us from accessing the 10 detectors wired to this SQUID array. The other array was operational, and we found that two out of the eleven detectors were open circuits. One of these open detectors was coupled to a large absorber (765 μm). These pixels showed signs of cracks in the nitride membranes prior to cooldown. It is likely that one of these cracks broke this pixel's leads. We were left with nine working pixels, for which critical temperatures and applied fields can be found in Table 8.1. Unfortunately some of these pixels were vignetted by the frame used to mechanically support the field coil, and we were unable to shine X-rays on these pixels. Therefore, we focused the most attention on pixels for which we could collect X-ray data. A drawing of the the pixels that were studied in detail is shown in Figure 8.1.

After the conclusion of the run, we discovered that the wrong calibration had been used for reading the cold plate thermometer that monitors the bath temperature. This meant that the temperatures measured during data taking were, in reality, about 6-10 mK higher than what thought. So, for example, a detector with a measured $T_c = 96$ mK had, after applying the correct calibration, $T_c = 106$ mK. All the data could be re-analyzed with the correct calibration applied, so no information was lost. However, it does mean that data were taken at a higher bath temperature than we intended, which increases the noise and slightly degrades the energy resolution. Therefore, the detectors were probably capable of somewhat better performance than what is presented here. All of the data presented in this chapter have been analyzed with the correct calibration, and all reported temperatures are the corrected values.

Despite losing many of the pixels to the SQUID array failure, we were still able to

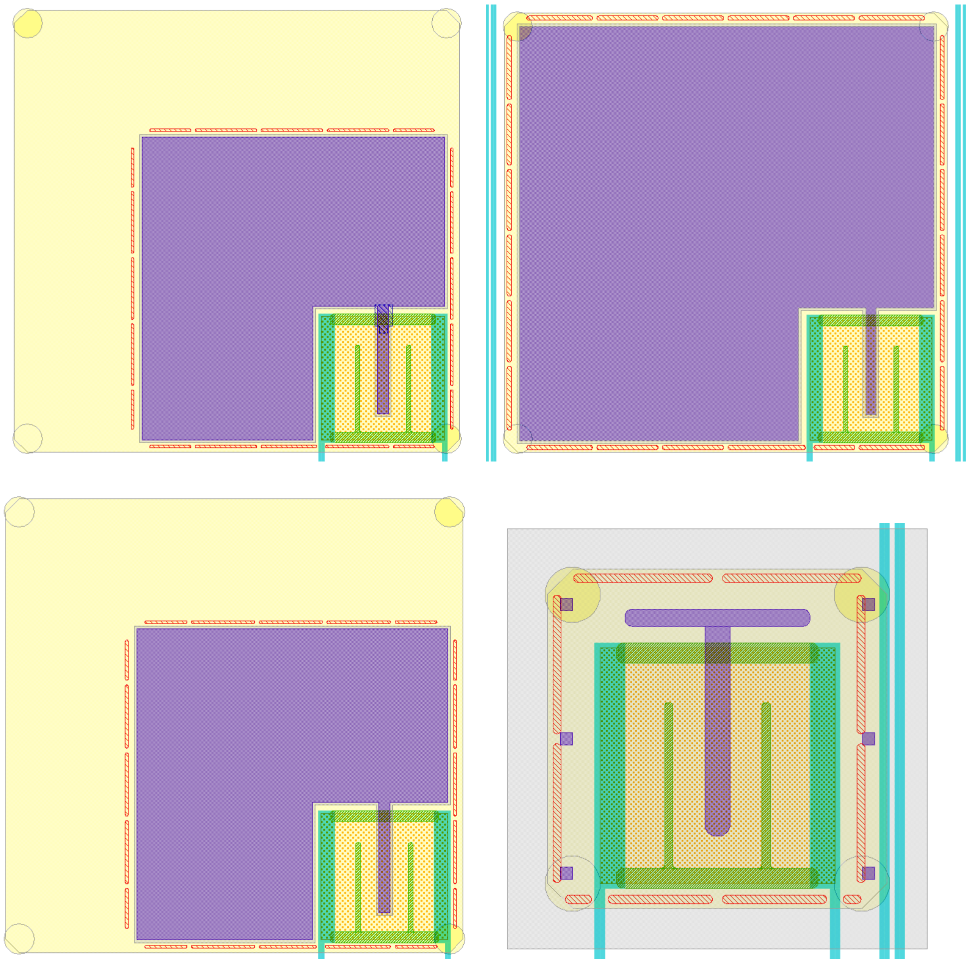

Figure 8.1: MXW1 chip D, illustration showing a selection of the pixel geometries tested. Top left: Pixel 62 had a 350 μm μm × 350 μm absorber, with 90.6% of the membrane perimeter near the edge of the absorber perforated. The back etch well that isolates the nitride membrane was approximately 500 μm across. This pixel also had an extra gold "bridge" running underneath the bank to improve thermal contact between TES and absorber. Top right: Pixel 63 had a 480 μm × 480 μm absorber, with 90.6% membrane perforation. Bottom left: Pixel 65 is identical to 62, except that it does not have a gold bridge. Bottom right: Pixel 66 had a 240 μm × 240 μm suspended absorber coupled to the TES by a T-stem, with 89.9% membrane perforation. Note that this pixel is shown enlarged relative to the others for clarity. The TES is the same size (140 μm × 140 μm) for all pixels.

test four absorber sizes. The smallest was a 240 μm × 240 μm suspended absorber coupled to the TES by a T-stem. This geometry is essentially identical to pixel L1c3 from chip MXW1j (see Section 7.2) and was included as a control to facilitate comparing the results from the coplanar pixels to arrays of suspended absorbers. The coplanar absorbers were 350 μm × 350 μm, 480 μm × 480 μm, or 765 μm × 765 μm, minus a cutout area approximately 150 μm × 150 μm for the TES. Prior to fabrication, we feared that step coverage where the absorber overlaps the TES to make thermal contact may be a concern. On some designs, a gap was left in the normal metal bank that runs parallel to the direction of current flow, so that the absorber gold layer would only have to climb up over the bilayer to make thermal contact. Other designs had an additional metal layer forming a short (50 μm) "bridge" of gold that ran from the TES, beneath the normal metal bank, and under the absorber gold. Some pixels had both of these features. The configurations tested in this run are described in Table 8.1 and drawings of selected designs are shown in Figure 8.1.

Pixel	size (μm)	membrane	B_{app} (V)	T_c (mK)	T_c w/ B_{app}	note
55	765	91.7%	0.480	106.1	107.3	nitride cracks
57	350	89.2%	-0.190	108.1	108.9	gap in bank
61	480	95.8%	-0.130	106.1	106.0	
62	350	90.6%, 600 μm	-0.160	107.9	108.3	bridge
63	480	90.6%	-0.130	106.2	106.6	
64	480	90.6%	-0.120	106.4	106.6	bridge
65	350	90.6%, 600 μm	-0.170	107.9	108.6	
66	240	90.6%	-0.150	108.0	108.6	suspended
67	240	92.1%	-0.120	108.3	109.4	suspended

Table 8.1: MXW1D pixel geometries tested. Size is the lateral dimension of the absorber. The membranes were either approximately 90% perforated or etched with a long trench that left only the corners intact. The free-standing area of the membrane was either matched to the absorber size or, where noted, may be larger. In these cases the approximate lateral dimension of the membrane is given. Applied field is the field that is observed to maximize T_c, and is assumed to be the field that nullifies the trapped flux. A geometry-based conversion from applied voltage to applied field is unavailable, so the applied voltage is reported. T_c values are given with zero field and with an applied field.

Nearly all of the large (765 μm) coplanar pixels on chip MXW1D were observed to have cracks in the nitride membrane. In some cases, the pixels broke out completely. Although pixel 55 appeared to have survived with only minor cracks, these were either worse than they appeared from visual inspection, or they worsened on cooldown. Although the predicted thermal conductivity for this pixel was $G(0.1K) = 235$ pW/K, we measured only 59.5 ± 13.5 pW/K. This probably means that the pixel partially detached from the substrate, breaking the nitride beams and reducing the thermal conductivity. This pixel also required a very different applied magnetic field to null the trapped flux than the rest of the pixels tested, again probably indicating that it was no longer lying flat in the plane.

The thermal conductivity of these pixels is of particular interest, since there is a large area of absorber gold in contact with the nitride membrane, which may make the conductivity to the bath difficult to control. We obtained IV curves at different bath temperatures for pixels c63 and 65 and used them to derive the TES to bath thermal conductivity (see Fig. 8.2 and 8.3), as described in Section 7.1. The conductivity is then used to determine the TES resistance and α_{IV} as a function of the TES temperature, which are plotted shown in Figures 8.4 and 8.5. The transitions appear generally smooth and featureless, with none of the kinks or bends observed in the MXW1j pixels (small pixels with absorber-to-TES stem variations, see Section 7.2). The transitions are also relatively steep, with α_{IV} greater than 60 throughout most of the transition for both pixels. For pixel 63, the measured thermal conductivity was 137.7 ± 33.9 pW/K, consistent with the the predicted value based on the perimeter of the TES plus absorber and the membrane perforation, which was 134 pW/K. For pixel 65, the expected thermal conductivity was 123 pW/K, (this assumes that the large area of isolated membrane outside of the perforations does not affect the conductivity). We measured 155.4 ± 21.1 pW/K, slightly high but still consistent with the predicted value.

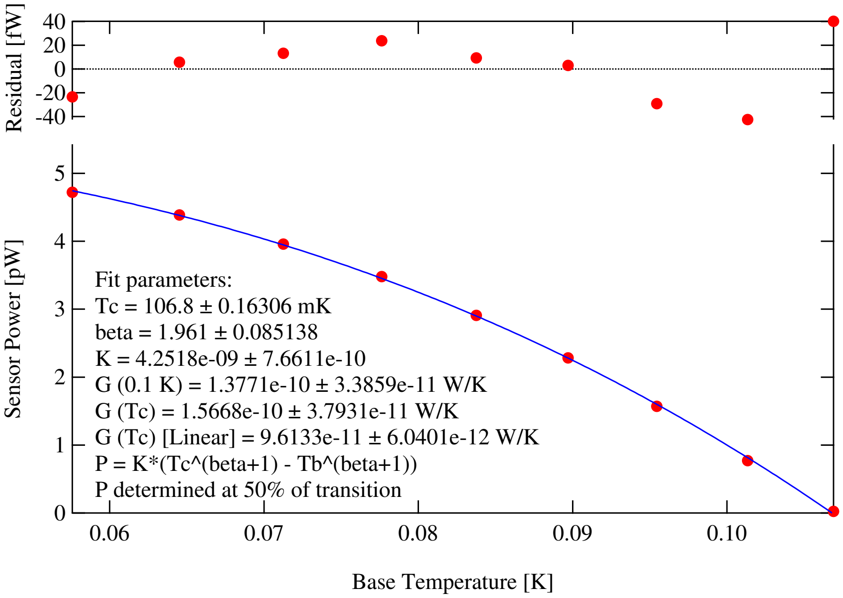

Figure 8.2: Pixel 63 (480 μm, 90.6% perforation) dissipated power at 50% R_n as a function of bath temperature. Blue line shows a fit to $P = K(T_c^n - T_b^n)$, where T_c is the temperature at 50% R_n. Derived thermal conductivity between the sensor and the bath is $G_0 = G(0.1K) = 137.7 \pm 33.9$ pW/K, with $n = 2.96 \pm 0.09$.

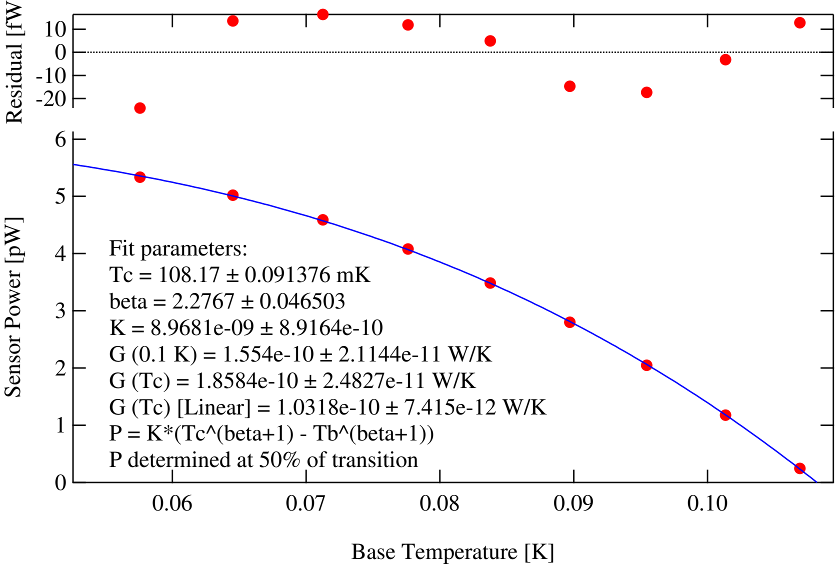

Figure 8.3: Pixel 65 (350 μm, 90.6% perforation) dissipated power at 50% R_n as a function of bath temperature. Blue line shows a fit to $P = K(T_c^n - T_b^n)$, where T_c is the temperature at 50% R_n. Derived thermal conductivity between the sensor and the bath is $G_0 = G(0.1K) = 155.4 \pm 21.1$ pW/K, with $n = 3.28 \pm 0.09$.

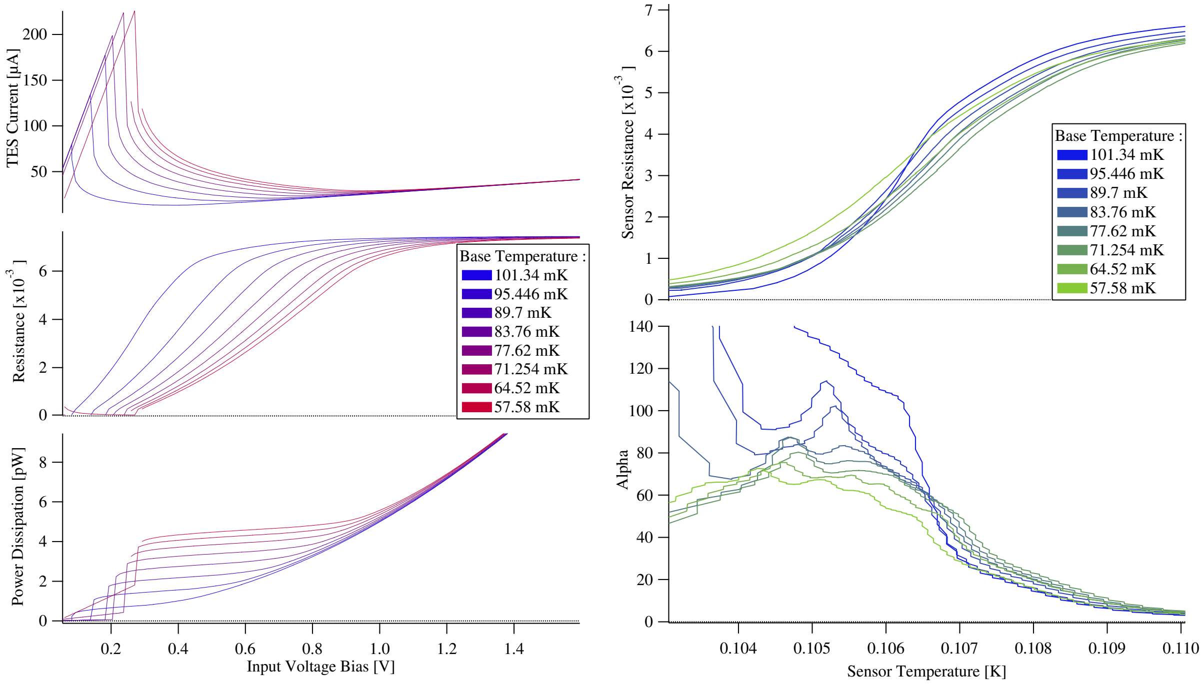

Figure 8.4: Pixel 63 (480 μm, 90.6% perforation). A voltage (V_{in}) is applied to the bias circuit through a large input resistor (R_{in} = 1.095 $k\Omega$), with a known shunt resistance ((R_{SH} = 0.2 mΩ)) Left: TES current (top), resistance (middle) and dissipated power (bottom) as a function of V_{in}. Right: TES resistance (top) and sensitivity α (bottom) as a function of TES temperature, determined using the measured thermal conductivity and power dissipation.

Measurements of the change in TES current as a function of applied magnetic field for pixels 63 and 65 are shown in Figure 8.6. The behavior is qualitatively more similar to devices the GSFC group has studied in the past (with a series of small oscillations near $B_{net} = 0$) than was observed in the MXW1j pixels.

An X-ray spectrum of the Mn Kα line was obtained for channel 65. Several features of the coplanar absorber design make the X-ray analysis process more complicated than the analysis for the suspended designs. For example, since the silicon substrate between pixels is left exposed in this design, X-rays absorbed in the substrate cause extra noise, which is easily visible at low frequencies (see Fig. 8.7). We can quantify this effect by collecting noise spectra with and without X-ray illumination, and comparing the energy resolution as

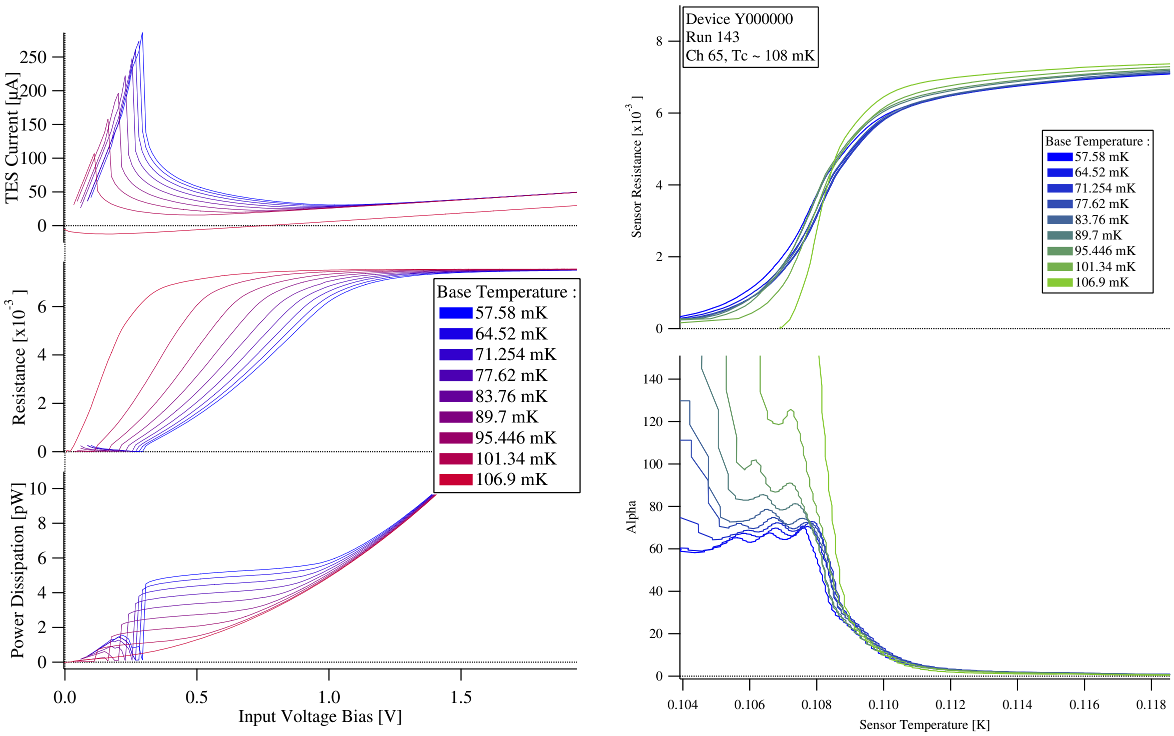

Figure 8.5: Pixel 65 (350 μm, 90.6% perforation) A voltage (V_{in}) is applied to the bias circuit through a large input resistor ($R_{in} = 1.095\ k\Omega$), with a known shunt resistance (($R_{SH} = 0.2$ mΩ)) Left: TES current (top), resistance (middle) and dissipated power (bottom) as a function of V_{in}. Right: TES resistance (top) and sensitivity α (bottom) as a function of TES temperature, determined using the measured thermal conductivity and power dissipation.

derived from the NEP. When the noise is measured without X-rays, $\Delta E_{NEP} = 3.47$ eV. With X-ray illumination, this increases to 3.55 eV. This degradation is both rate and energy-dependent, so lower energy X-rays will cause less noise. This effect could be mitigated in the future by adding a layer of gold on top of the silicon substrate between the pixels to increase the thermal conductivity of the substrate.

Figure 8.8 shows the optimally filtered spectrum of Mn Kα X-ray events plotted over the intrinsic profile of the Mn Kα1,2 line complex. The spectrum has several features that did not appear in the spectra from pixels with suspended absorbers. The prominent high energy shoulder is a typical sign of position dependent pulse shape. There is also

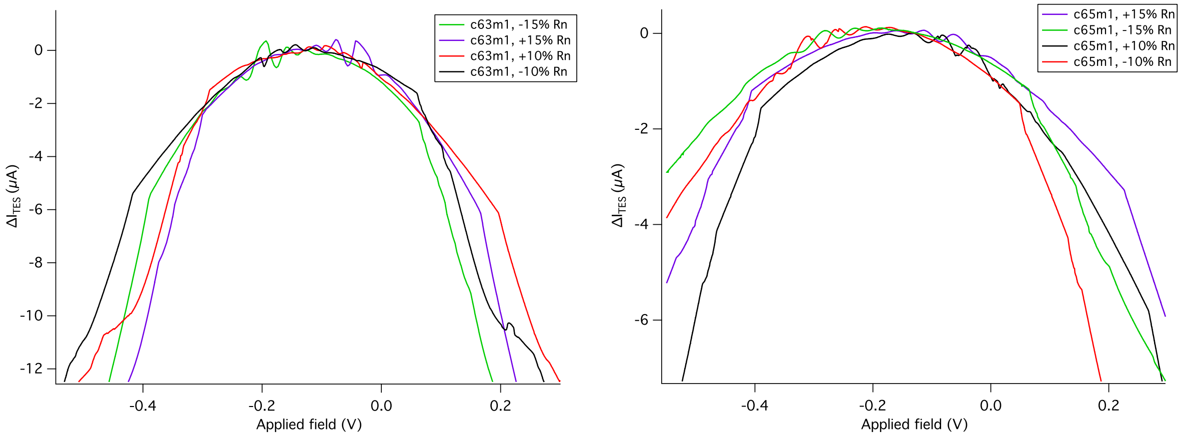

Figure 8.6: Change in TES current versus applied field at $T_b = 55$ mK for different voltage biases. Labels indicate bias point at $\Delta I_{TES} = 0$. Curves labeled with negative numbers (e.g. -15% Rn) indicate that the direction of the bias current is reversed. A geometry-based conversion from applied voltage to applied field is unavailable, so the applied voltage is reported. Left: Pixel 63 (480 μm, 90.6% perforation). Right: Pixel 65 (350 μm, 90.6% perforation).

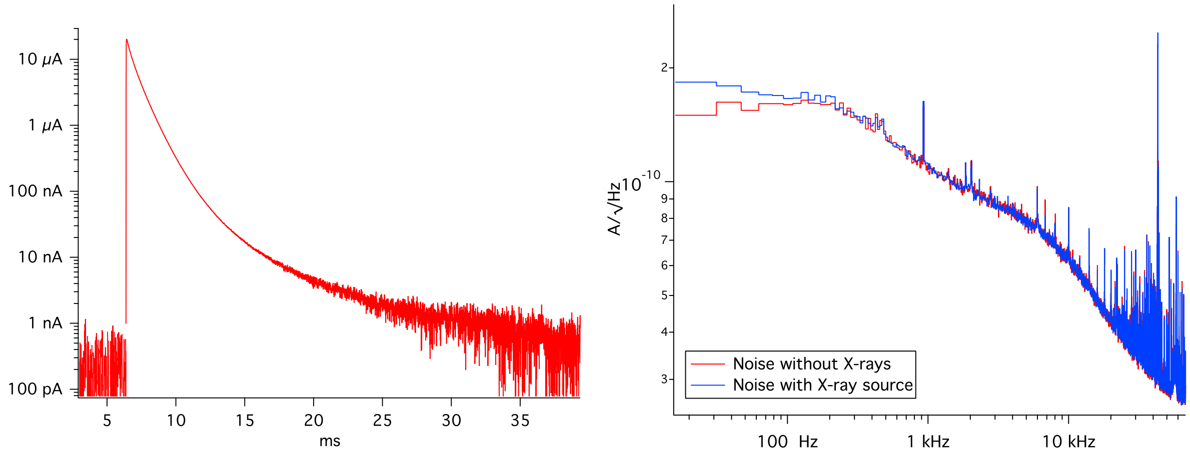

Figure 8.7: Pixel 65 (350 μm, 90.6% perforation) Mn Kα X-rays, biased at 15% R_n, with $T_b = 57.8$ mK. Left: Average pulse used to construct optimal filter Right: Average noise with and without X-ray illumination

a small population of events that are assigned a significantly higher energy. Looking at a plot of the rise time of the events versus the measured pulse height (Fig. 8.9) gives us a clue as to their origin: these events have a faster rise time, and are therefore likely due to X-rays that are absorbed directly in the TES. Unlike pixels where the absorber is suspended, the TES is not shielded by the absorber in this design, so we expect to see a much higher percentage of these type of events. Comparing the number of TES events ("fast" rise times $< 20\mu$s) to events which are assumed to be incident on the absorber (correcting for the relative areas and absorption efficiencies of the sensor and absorber) confirms this interpretation.

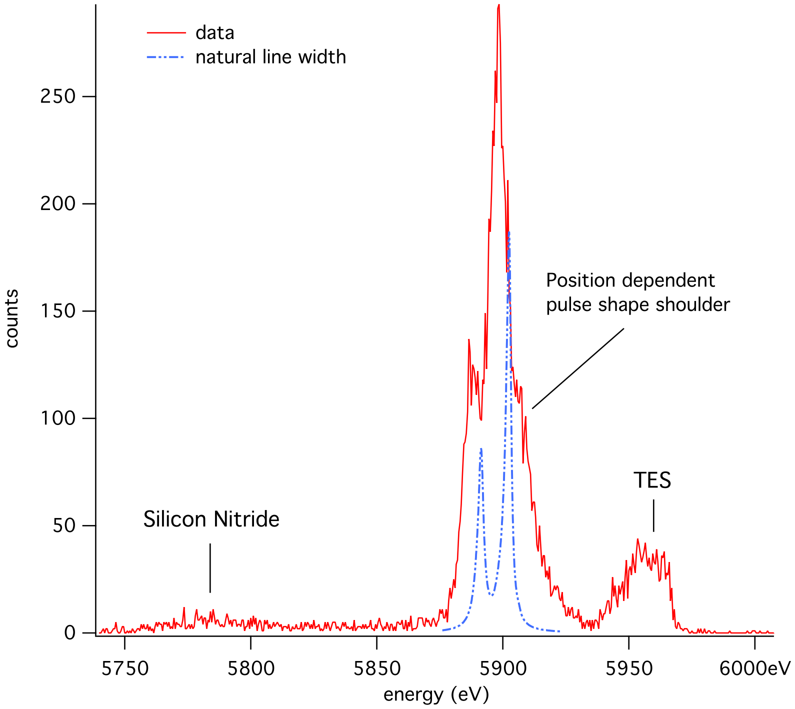

Figure 8.8: Pixel 65 (350 μm, 90.6% perforation) Mn Kα X-rays, biased at 15% R_n, with $T_b = 57.8$ mK. The intrinsic profile of the Mn Kα1,2 line complex is shown in blue. The high shoulder on the Mn Kα line is likely a result of position dependent pulse shape variation. The small cluster of events that are assigned a higher energy are due to X-rays absorbed directly in the TES. They are easily identified by their rise time (see Fig. 8.9). Events that are absorbed in the nitride membrane are apparent at slightly lower energy.

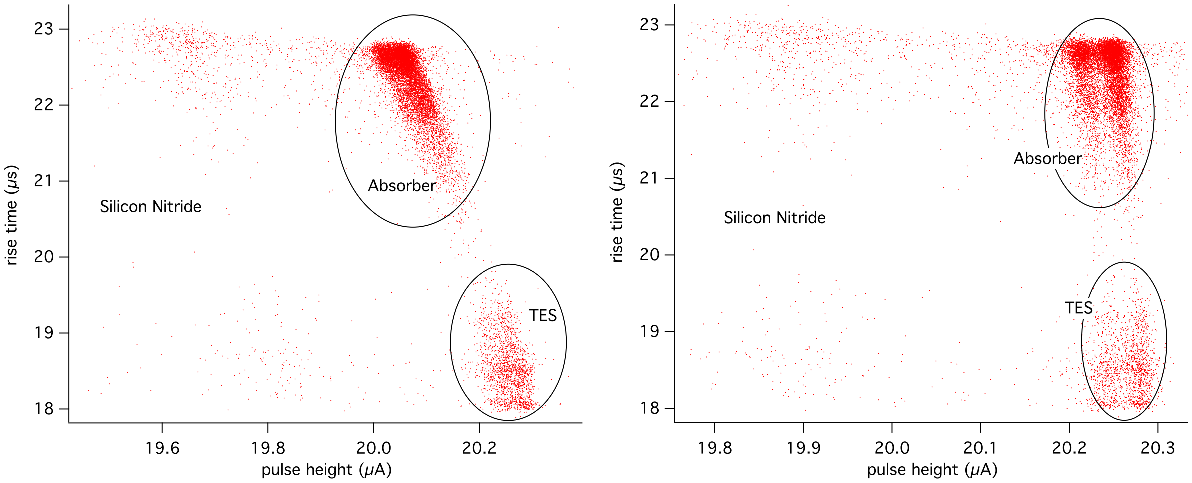

Figure 8.9: Pixel 65 (350 μm, 90.6% perforation) Mn Kα X-rays, biased at 15% R_n, with $T_b = 57.8$ mK. Plots show the pulse rise time as a function of the pulse height. Left: Prior to application of the optimal filter. The TES and absorber events are still easily identified by rise time. Right: Data after processing with a 1 kHz low pass filter applied to the optimal filter. The low pass filter reduces the rise time/pulse height slope of the absorber events, as expected in the case of position dependent pulse shape variation.

The TES events are easy to separate by making a selection based on rise time, as Fig. 8.9 shows. The high energy shoulder on the Mn Kα line is also apparent as a slope in the rise time/pulse height plot of the events incident in the absorber. From our experience with the minimally degraded resolution exhibited by the 890 μm × 890 μm suspended absorbers (MXW1d, see Section 7.1) this variation in the pulse shape may seem unexpected, since this absorber has the same gold thickness but approximately eight times less surface area. Therefore, in this case the position dependent pulse shape variation is probably not a direct result of the time constant for lateral heat transport in the gold absorber. Rather, it is likely due to the large area of the absorber that is in contact with the membrane in the coplanar geometry, resulting in increased loss of heat to the substrate before the absorber can thermalize. In the suspended absorber designs, we were able to mitigate this effect by minimizing the area of the support stems (the only part of the absorber in direct contact with the membrane).

The spectrum was analyzed by selecting the events by rise time (greater or less than 20 μs), which effectively separates the TES and absorber events. Each population is optimally filtered, then separate gain scales are applied to the events. The high energy shoulder on the line due to the pulse shape variation produces a very non-Gaussian line profile, so the natural line profile plus Gaussian broadening no longer produces a good fit to the data. We can apply a low pass filter to the optimal filter template to reduce the broadening at the expense of signal-to-noise ratio, as we saw in the previous chapter. With a 5 kHz single pole low pass filter, the ΔE_{NEP} is degraded from 3.55 eV to 3.90 eV. However, the high energy shoulder is eliminated and we find the resolution at Mn Kα is 7.00 ± 0.13 eV for the absorber events, and 6.22 ± 0.29 eV for the TES events. Reducing the cutoff frequency to 1 kHz, we find that the Mn Kα resolution improves to $\Delta E = 5.42 \pm 0.22$ eV for absorber events and 5.38 ± 0.26 eV for TES events, with $\Delta E_{NEP} = 4.85$ eV (see Fig. 8.10).

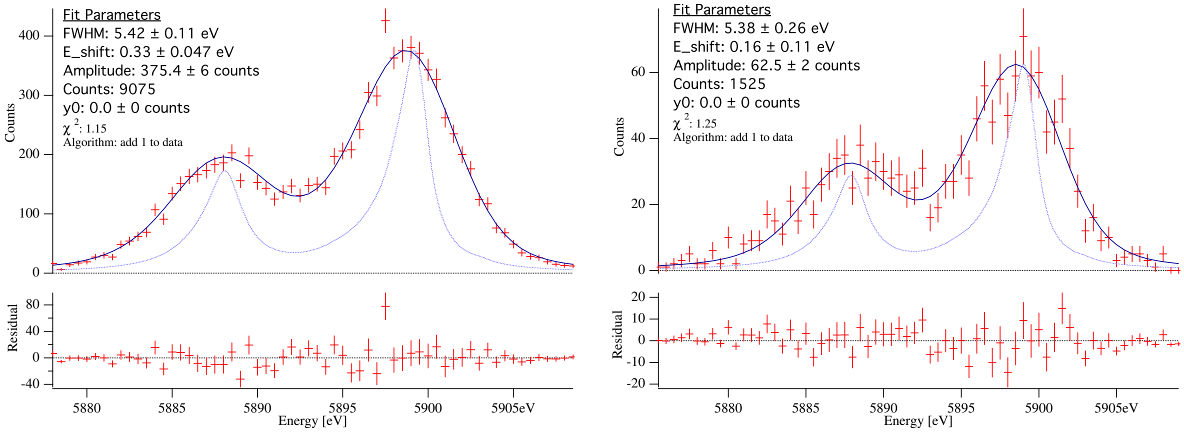

Figure 8.10: Pixel 65 (350 μm, 90.6% perforation) Mn Kα X-ray spectrum, biased at 15% R_n, with $T_b = 57.8$ mK. The data were processed with a 1 kHz low pass filter applied to the optimal filter. The intrinsic profile of the Mn Kα1,2 line complex is shown in blue. Left: Absorber events only, $\Delta E = 5.42 \pm 0.22$ eV. Right: TES events only, 5.38 ± 0.26 eV.

The measured ΔE_{NEP} of about 3.5 eV for this device is roughly consistent with predictions from the model, given the high transition temperature (108 mK) and absorber thickness (500 nm). The correlation of pulse height and rise time and the subsequent improvement in resolution with low pass filtering show that the degradation due to position-dependent pulse shape for this design is a significant concern. Although the degradation will be proportionally smaller at lower incident energies, this pixel is also several times smaller than the target for the final design, so it will be important to study larger devices and softer X-ray energies.

8.2 Pixel c66: 240 $\times$240 μm suspended absorber

Chip MXW1D was designed primarily for testing coplanar absorbers, but there were several pixels with small (240 μm $\times$ 240 μm) suspended absorbers. These designs were included as a sort of control, to facilitate comparison between arrays of coplanar and suspended designs. Two such pixels were wired during this run (c66 and c67), and we collected an Mn Kα X-ray spectrum (Fig. 8.12) and measurements of TES current as a function of applied field (Fig. 8.11) for c66. We expect c66 to behave in a similar fashion to the pixels from MXW1j (see Section 7.2) with the same size and T-stem design (pixels L1c2 and L1c3). Qualitatively, the TES current appears to vary with applied field in a similar fashion to MXW1j-L2c2 (see Figure 7.23); mostly varying smoothly with one prominent feature near $B_{net} = 0$.

Turning to the X-ray data, we find that $\Delta E_{NEP} = 2.28$ eV. We can compare this result to the expectation based on our model (see Appendix A.2). Scaling the modeled ΔE (which assumed $\alpha = 55$ and $\beta = 1.25$) to account for the high T_c (108.6) and the 500 nm thick absorber, we would expect 2.26 eV resolution, consistent with the measurement.

The fit to the Mn Kα line yields 2.80 ± 0.08 eV resolution (1.65 eV of broadening). Applying a 10 kHz low pass filter to the optimal filter template degrades ΔE_{NEP} slightly to 2.38 eV but improves the Mn Kα fit to match that resolution. Since broadening due to high frequency pulse shape variation scales linearly with incident energy, this degree of broadening would not be detectable in the energy range we are ultimately interested in (250 eV).

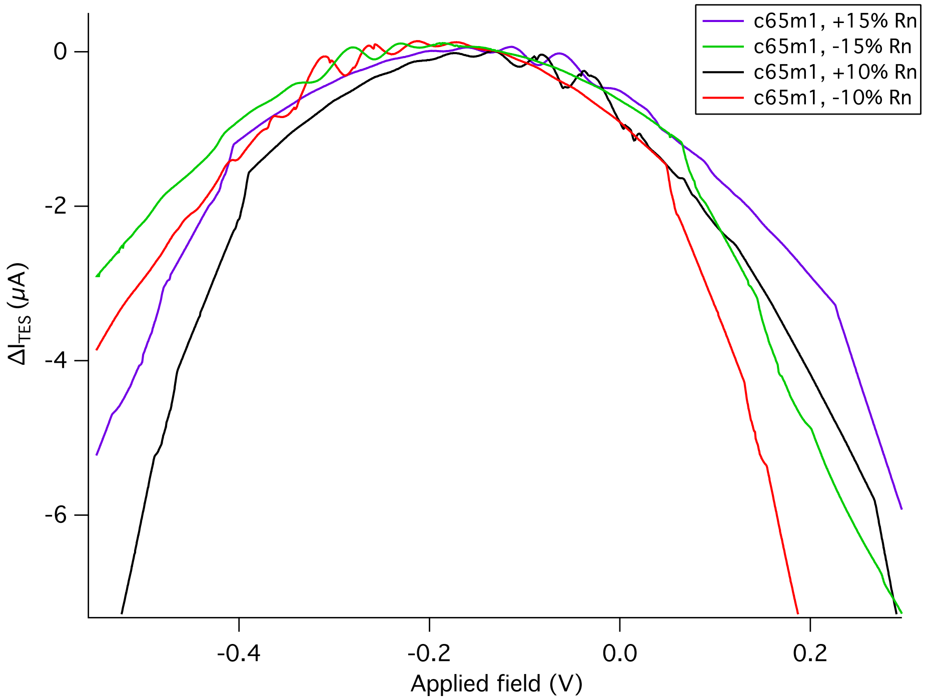

Figure 8.11: Pixel 66 (240 μm suspended, 89.9% perforation) Change in TES current versus applied field at $T_b = 55$ mK for different voltage biases. Labels indicate bias point at $\Delta I_{TES} = 0$. Curves labeled with negative numbers (e.g. -15% Rn) indicate that the direction of the bias current is reversed. A geometry-based conversion from applied voltage to applied field is unavailable, so the applied voltage is reported.

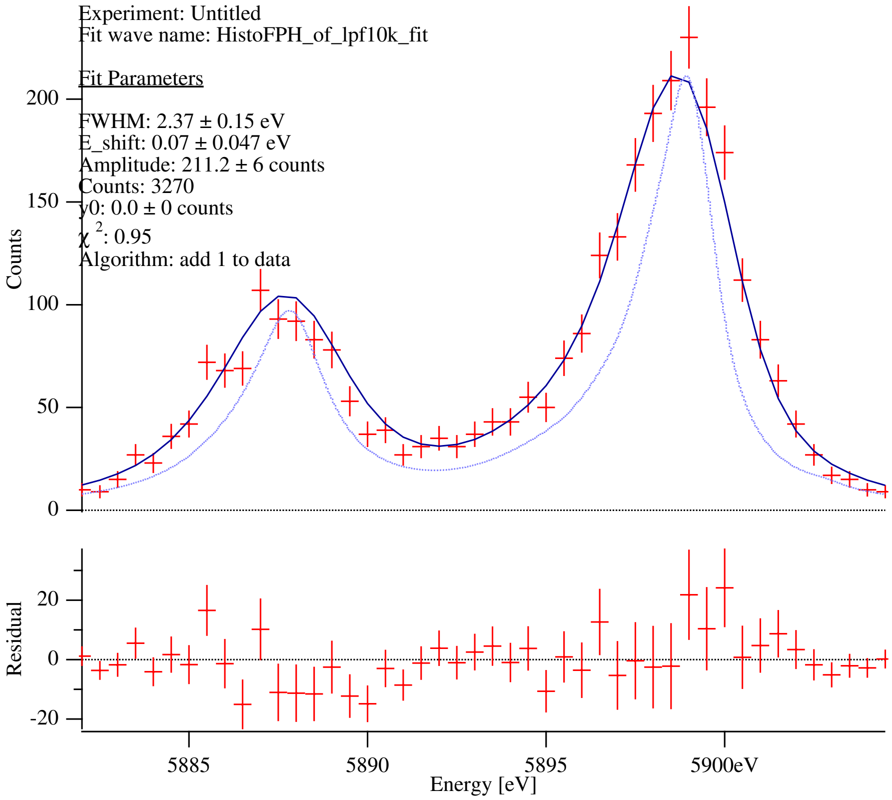

Figure 8.12: Pixel 66 (240 μm suspended, 89.9% perforation) Mn Kα X-ray spectrum, biased at 15% R_n, with $T_b = 57.8$ mK. A 10 kHz low pass filter has been applied to the optimal filter, so that $\Delta E_{NEP} = 2.38$ eV. The Mn Kα resolution is 2.37 ± 0.15 eV.

Chapter 9

MXW2 and the future

9.1 Results from MXW2

The product wafer from the second fabrication run ("MXW2") yielded in early February, 2015 (for details on the fabrication process changes, see 6.2). Since SEM imaging indicated that many of the larger suspended absorbers were probably touching the substrate in multiple places, we elected to test some of the coplanar pixels first. Visual inspection indicated near 100% yield on all the coplanar designs up to the 765 μm × 765 μm size. However, most of the coplanar pixels were affected by excess gold plated over the leads (see Section 6.2 and Figure 6.8). Although the leads were protected by photoresist during the electroplating and therefore were probably not shorted, we found that one chip of coplanar absorbers had no excess plating, so that chip was chosen for testing first. This chip (MXW2c) was a 4 × 5 array. Four of the devices had no absorber, four had 825 μm × 825 μm coplanar absorbers, and twelve had 765 μm × 765 μm coplanar absorbers. All of the absorbers had a grid of titanium dots adhering them to the nitride membrane. Half of the pixels had 91.7% perforated membranes, and half had long slots etched into the membrane, removing 97.5% of the perimeter (see Fig. 9.1). Eight of the pixels were given the gold “bridge” feature meant to improve the thermal connection between the absorber and TES. Two more pixels had a variation on this idea, where the bank of the TES was extended to overlap the absorber. Photos of these designs are shown in Fig. 9.2. Unfortunately, a scratch across the chip that occurred during fabrication severed the leads of the two pixels with the extended bank feature, so we were unable to test them during this run.

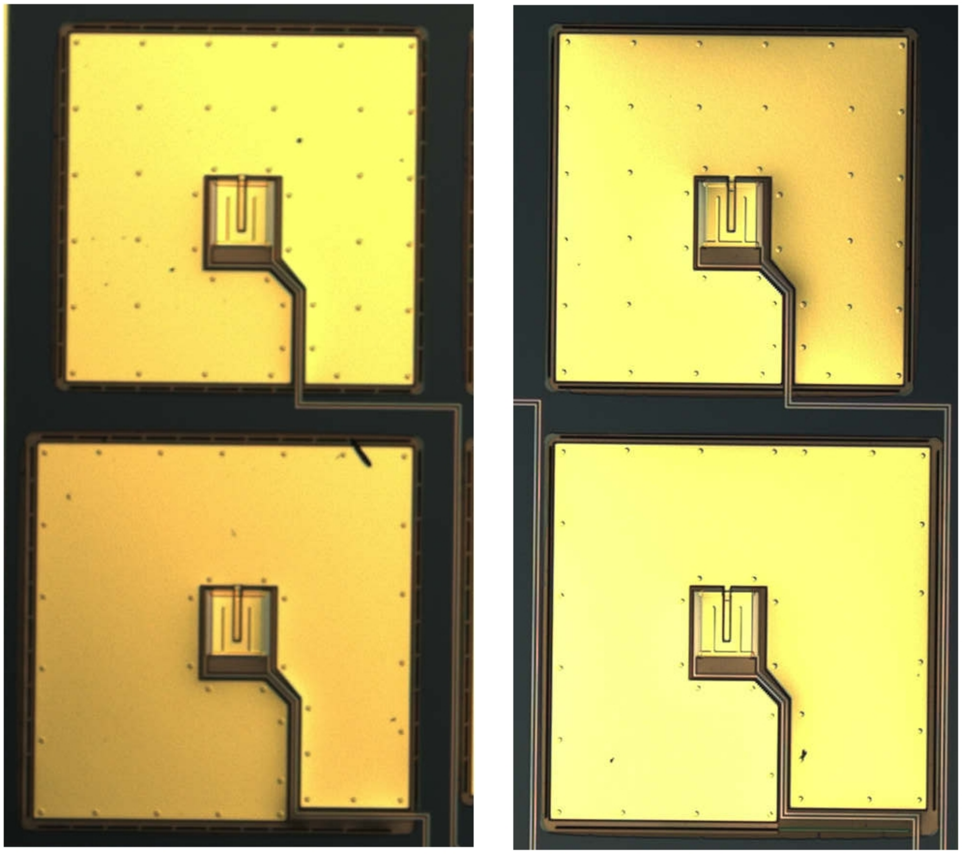

Figure 9.1: MXW2c optical microscope images. The locations of titanium dots used to adhere the absorber to the membrane are easily visible underneath the gold. Left: pixels with approximately 91.7% perforated membranes Right: long slots etched into the membrane, removing 97.5% of the perimeter

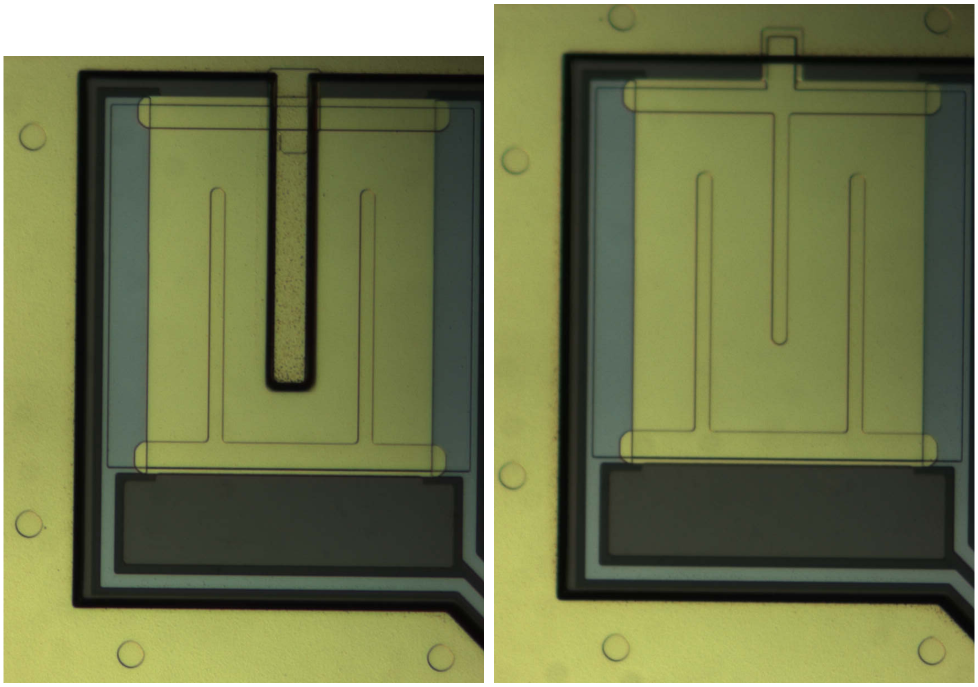

Figure 9.2: MXW2c TES optical microscope images Left: Added gold bridge runs underneath the normal metal bank between the TES and the absorber. Right: The normal metal bank is extended to make thermal contact to the absorber.

The TES bilayer was 50 nm of Mo and 240 nm of Au, with a target T_c of 70 mK. The measured transition temperatures ranged from 68 to 70 mK (see Table 9.1). The absorbers were made up of 200 nm of evaporated gold plus 100 nm of electroplated gold. None of the membranes showed signs of cracking after fabrication, however four out ten of the pixels with long slots in the membrane cracked in at least one corner during wirebonding. Of these pixels, one was found to be an open circuit upon cooldown, indicating that the leads had broken. Two of the long slot pixels that did not appear cracked after wirebonding were open after cooldown. Of the pixels with 91.7% perforated membranes, none showed signs of damage after wirebonding or cooldown. With the titanium dots and rounded front etch trenches, the 91.7% perforated designs now appear fairly robust, whereas most of the long slot pixels had failed by the time they had been cooled down. The chip was tested at GSFC in February 2015, in the same cryostat used to test MXW1D (see Chapter 8). Again, two SQUID arrays (indicated by "m1" and "m2" in Table 9.1) were used to address individual first stage SQUIDs, each coupled to a single TES.

Pix	size (μm)	perf	B_{app} (V)	T_c (mK)	T_c w/B	note
54m1	825	92.4%	0.206	67.7	68.35	TES-absorber bridge
57m1	765	91.7%	0.174	67.6	68.5	TES-absorber bridge
61m1	765	91.7%	0.165	67.6	68.4	
62m1	765	91.7%	0.163	67.7	68.5	
54m2	825	97.7%	0.237	66.9	68.45	crack post-wirebond
55m2	765	97.5%				open upon cooldown
57m2	N/A	97.5%	0.215	69.05	71.2	no absorber
61m2	N/A	97.5%	0.205	68.9	70.95	no absorber
62m2	765	97.5%	0.164	67.8	68.7	crack post-wirebond
63m2	765	97.5%	0.198	66.9	68.1	crack post-wirebond
64m2	765	97.5%	0.182	67.75	69.0	
65m2	765	97.5%				crack post-wirebond, open
66m2	825	97.7%				open upon cooldown
67m2	765	97.5%	0.200	67.25	68.6	

Table 9.1: MXW2c pixel geometries tested. Size is the lateral dimension of the absorber. The column labeled "perf." denotes the percentage of membrane perimeter remaining after etching. Applied field is the field that is observed to maximize T_c, and is assumed to be the field that nullifies the trapped flux. A geometry-based conversion from applied voltage to applied field is unavailable, so the applied voltage is reported. T_c values are given with zero field and with an applied field.

One of our primary concerns about changing the design from having a titanium layer under the entire area of the gold absorber to the grid of small titanium dots was how this would affect the detector to bath thermal conductivity. Since the purpose of the titanium is to adhere the gold to the nitride, it seemed likely that reducing the area of the titanium so drastically would reduce the thermal conductivity. This would be beneficial, as long as the conductivity scaled predictably as we changed the pattern of titanium. However, if the gold was making weak thermal contact to the nitride where there was no titanium underneath, this could introduce a source of large pixel-to-pixel variation. We collected IV curves as a function of bath temperature for three pixels to measure the detector to bath thermal conductivity. For pixel c62m1, a 765 μm pixel with 91.7% perforation, we would expect $G(0.1K) = 236$ pW/K, if the phonon emitting perimeter that contributes to the conductivity included the entire perimeter of the absorber plus the perimeter of the TES. We measured $G(0.1K) = 230 \pm 38$ pW/K (see Fig. 9.3 and 9.4).

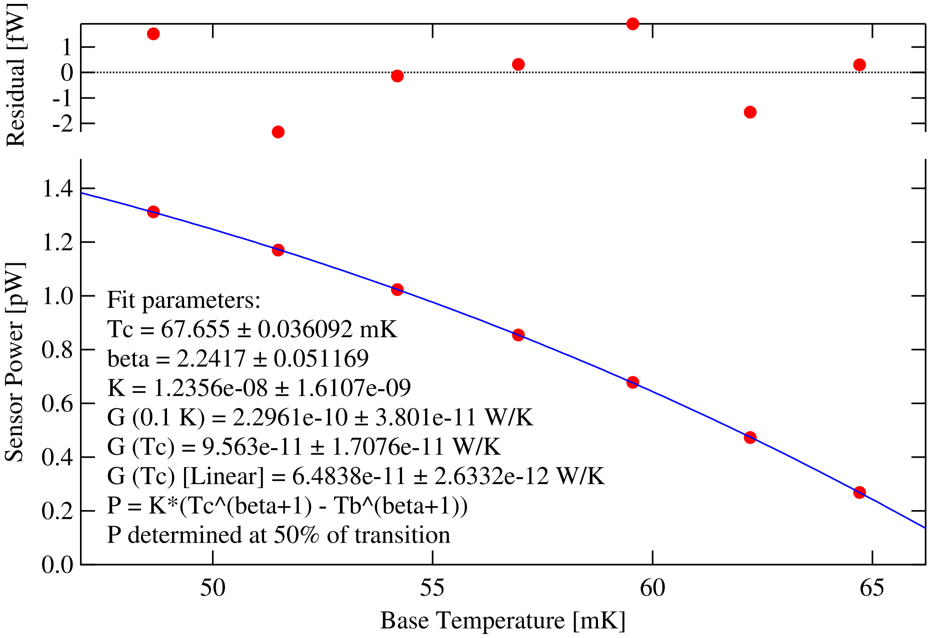

Figure 9.3: Pixel c62m1 (coplanar absorber, 91.7% perforated membrane) dissipated power at 50% R_n as a function of bath temperature. Derived thermal conductivity between the sensor and the bath is $G_0 = G(0.1K) = 230 \pm 38$ pW/K, with $n = 3.24 \pm 0.05$.

For pixel c67m2, a 765 μm pixel with 97.5% perforation, we expect 77 pW/K and measure 106 ± 29 pW/K. Since we expect the gold not to adhere to the nitride unless there is titanium underneath, we might have expected that the conductivity of these pixels would be much smaller. However, if we compute G assuming that the phonon emitting perimeter includes the circumference of the titanium dots plus the perimeter of the TES, we would predict Gs that were 35% smaller than the figures quoted above. This is clearly

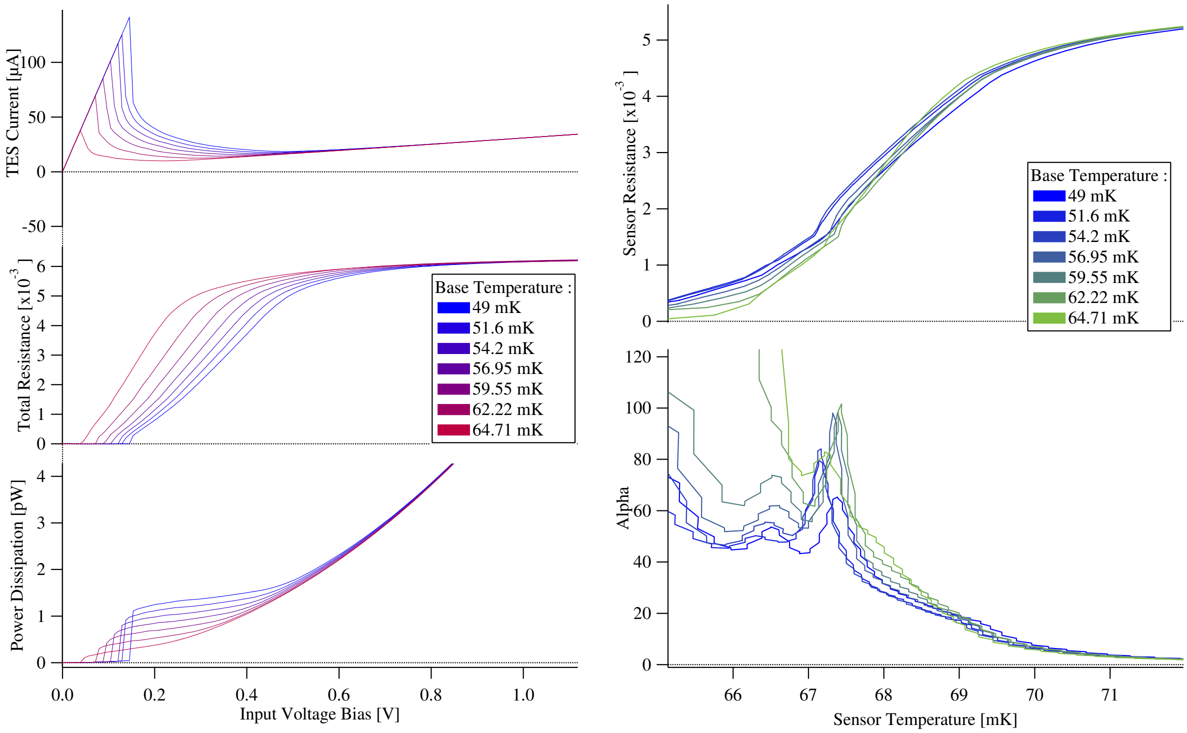

Figure 9.4: Pixel c62m1 (coplanar, 91.7% perforated membrane) Left: TES current (top), resistance (middle) and dissipated power (bottom) as a function of input bias voltage. Right: TES resistance (top) and sensitivity α (bottom) as a function of temperature.

not consistent with the measurements, but it is surprising that the change from a sheet of titanium to the grid of dots appears to have no affect on the conductivity.

We collected Al Kα spectra for pixels c57m1 and c67m2, which are shown in Figure 9.5. In both cases, the pixels were partially vignetted by the field coil, but at least 50% of the surface area of the pixel was exposed, including the TES. For pixel c57m1, a 765 μm pixel with 91.7% perforation, $\Delta E_{NEP} = 3.21$ eV. Fitting the Al Kα line, we find that $\Delta E = 6.34 \pm 0.12$ eV. This significant broadening is due to position dependent pulse shape, most likely loss from the coplanar absorber to the heat bath (similar behavior was observed in the MXW1 coplanar pixels, see Section 8.1). As expected, applying a low pass filter to the optimal filter template (effectively discarding high frequency signal to noise bins) improves the result significantly. By applying a 3 kHz low pass filter and excluding the events directly absorbed in the TES with a cut on the pulse rise time, we find $\Delta E = 3.79 \pm 0.08$ eV with $\Delta E_{NEP} = 3.49$ eV (Fig. 9.5, left). Reducing the low pass filter cutoff further does not produce significant improvement. Pixel c67m2 is also 765 μm, but has long slots etched into the membrane, giving it approximately 2.5 times lower conductivity to the bath. This should reduce the amount of heat lost to the bath before the absorber thermalizes, and consequently we should observe less broadening. For this pixel, we find $\Delta E_{NEP} = 2.99$ eV, and the fitted Al Kα resolution with no filtering is 4.15 ± 0.07 eV. Applying a 2 kHz low pass filter to the optimal filter improves the Al Kα resolution to 3.51 ± 0.06 eV with $\Delta E_{NEP} = 3.25$ eV (Fig. 9.5, right).

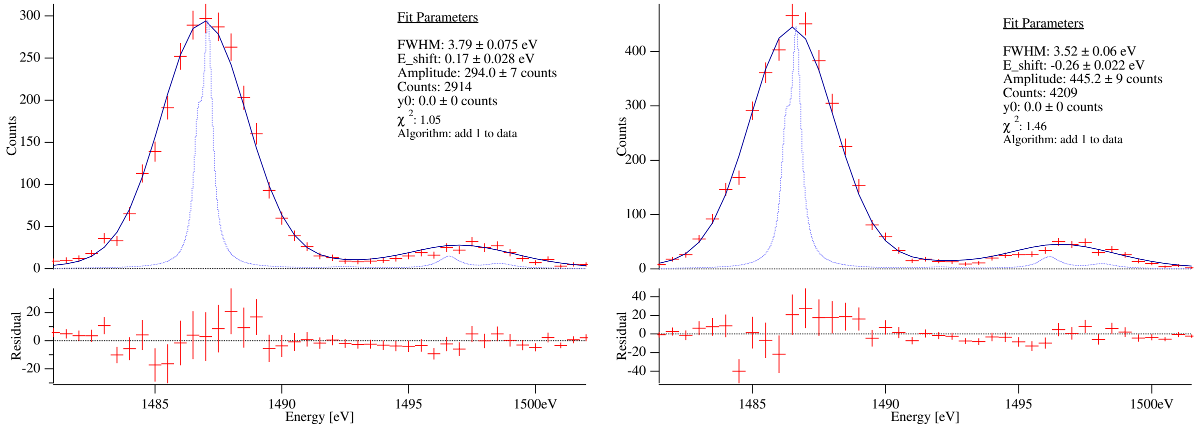

Figure 9.5: Al Kα X-ray spectra. Left: Pixel c57m1 (91.7% perforated membrane). With a 1 kHz low pass filter applied, $\Delta E = 3.79 \pm 0.08$ eV with $\Delta E_{NEP} = 3.49$ eV. Right: Pixel c67m2 (97.5% perforation). With a 2 kHz low pass filter applied, $\Delta E = 3.51 \pm 0.06$ eV with $\Delta E_{NEP} = 3.25$ eV

For this run we wanted to make a measurement of both α and β for our detectors, both to inform future designs and to improve our ability to model the devices. To determine β and to make another measurement of α (independent of the method used to determine α_{IV}), we can measure the complex impedance of the TES. The total impedance is given by $Z(\omega) = R_{SH} + i\omega L + Z_{TES}(\omega)$, with Z_{TES} given by:

$$Z_{TES}(\omega) = R_{TES}\left(\frac{(1+i\omega\tau)(1+\beta)+L}{(1+i\omega\tau)-L}\right) \tag{9.1}$$

where $L \equiv P\alpha/GT$. We determine the impedance by measuring the TES current (I_{TES}) as a function of a small AC modulation ($I_{bias} \times R_{SH}$, where $R_{SH} \ll R_{TES}$). This is measured for a particular bias point and magnetic field as a function of the frequency of the small modulation. Then, we can fit the data to Equation 9.1 to find R_{TES}, α, and β. To do this, it is helpful to have a good estimate for the heat capacity and thermal conductivity.

We measured the total heat capacity for pixel c57m1 by collecting X-ray pulse data at $T_b \approx T_c$, where the effect of electrothermal feedback is negligible and $\tau_{eff} \approx \tau_0 \equiv C/G$. The average pulse shape shows more than one time constant, and we find $\tau = 12.8$ ms for the longest part of the pulse. Since c57m1 is the same size as c62m1 and also has a 91.7% perforated membrane, we adopt $G(0.1K) = 230$ pW/K to calculate that the total heat capacity $C(T_c) = 1.28$ pJ/K, an excess of about 63% over the expected 0.784 pJ/K. Using the measured G, we can fit the complex impedance of the device. We collected impedance data at constant magnetic field (B = 0.165 V, the same field applied to collect the X-ray spectrum seen in Figure 9.5) for a variety of bias points. The best fit value for $C(T_c) = 1.12$ pJ/K, similar to what we measured. The data and fits to the model are shown in Figure 9.6, along with a plot of the derived α and β as a function of bias point. The data shows that β is significantly larger than zero through most of the transition, and that α and β are strongly correlated. For comparison, a we acquired IV curve data for c57m1 at $T_b = 55$ mK and a variety of applied magnetic fields. We find that α as derived from complex impedance roughly agrees with α_{IV} in magnitude, and qualitatively both

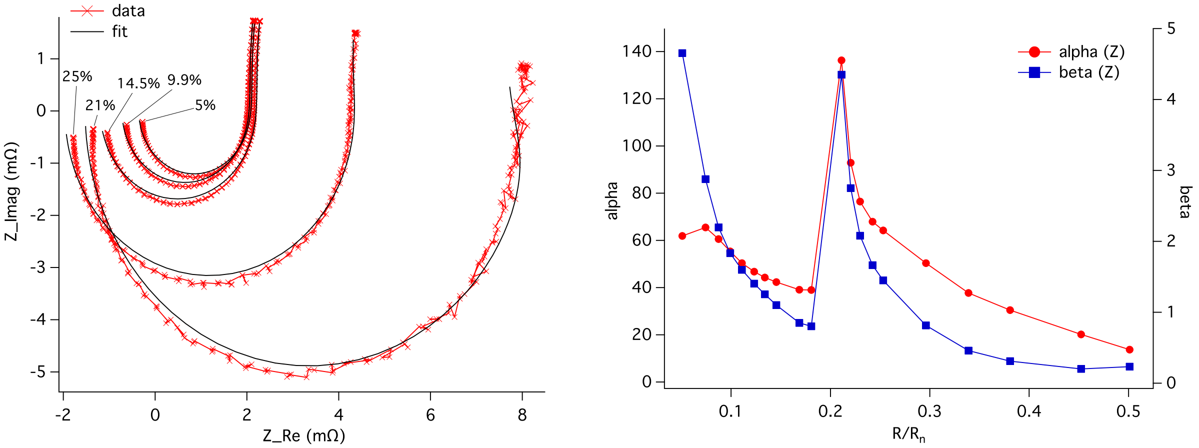

Figure 9.6: Pixel c57m1 (91.7% perforated membrane) measurements of complex impedance as a function of bias point for $T_b = 55$ mK and applied $B = 0.165$ V. Left: Imaginary vs. Real impedance with fits for α and β (only selected bias points are shown) Right: α and β as a function of bias point, as derived from fits to complex impedance

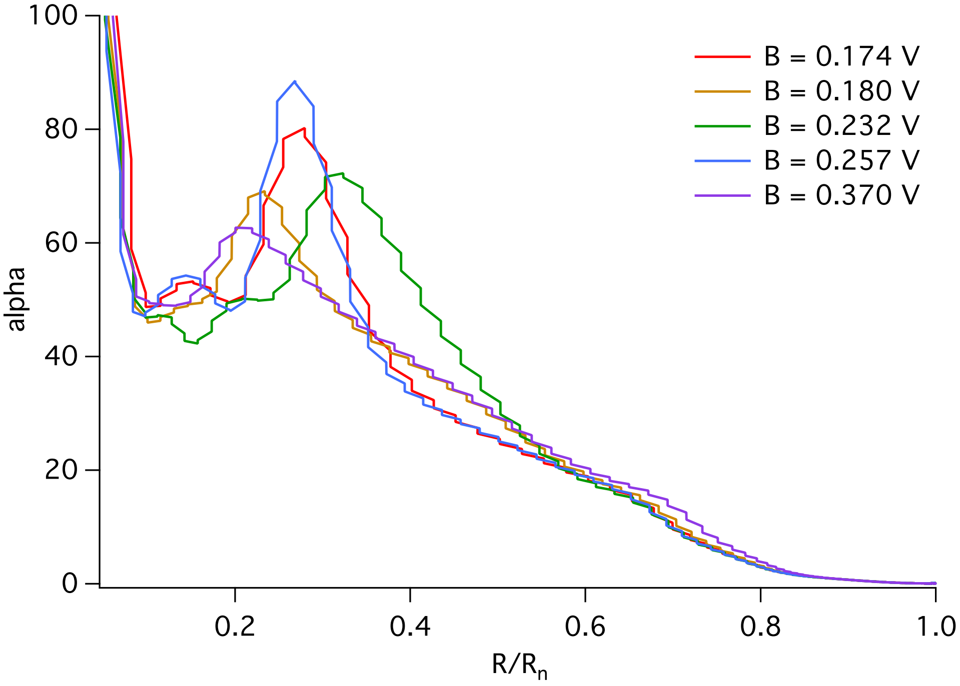

Figure 9.7: Pixel c57m1 (91.7% perforation) α_{IV} plotted versus bias point for varying applied magnetic field.

methods reveal a large peak in α around 20% R_n. The location and size of the peak in α change with applied magnetic field, suggesting that for optimal performance the detector must be operated at both a favorable bias point and applied field.

9.2 Lessons and open questions

One of our goals for MXW1 and 2 was to assess our ability to control the thermal conductivity between the TES and the bath. When position dependent pulse shape is a problem, as it often is in large devices, the effects can be mitigated by reducing $G_{tes-bath}$. We assumed, based on previous experience with thin nitride membranes, that the thermal conductivity would scale with the percentage of membrane perimeter remaining times the total phonon emitting perimeter (including the TES and parts of the absorber that were in contact with the membrane). It was not obvious this would remain true over a fairly large range of absorber and stem designs: from very large, highly perforated membranes with many small stems to the large coplanar absorbers where the entire absorber is deposited directly onto the membrane. However, for the most part we found very close agreement between the expected thermal conductivity on all of the designs, both suspended and coplanar. All of the thermal conductivity measurements we made, along with the predictions based on pixel geometry, are shown in Table 9.2 and plotted in Figure 9.8.

There were a couple of notable outliers. One such pixel was a large coplanar pixel from MXW1D with a 91.7% perforated membrane. This pixel had a much smaller conductivity than was predicted (it appears at the bottom right of the plot Fig. 9.8). This pixel had several cracks in the membrane prior to cooling. In fact, the measured conductivity is almost exactly 25% of the predicted value, indicating that three out of the four corners were probably broken. The other case is at the opposite extreme: a 91.7% perforated

890 μm × 890 μm suspended absorber with very small support stems. The measured conductivity was approximately a factor of three higher than expected. The reason for this is currently unknown, but it may indicate a thermal touch between the absorber and the substrate.

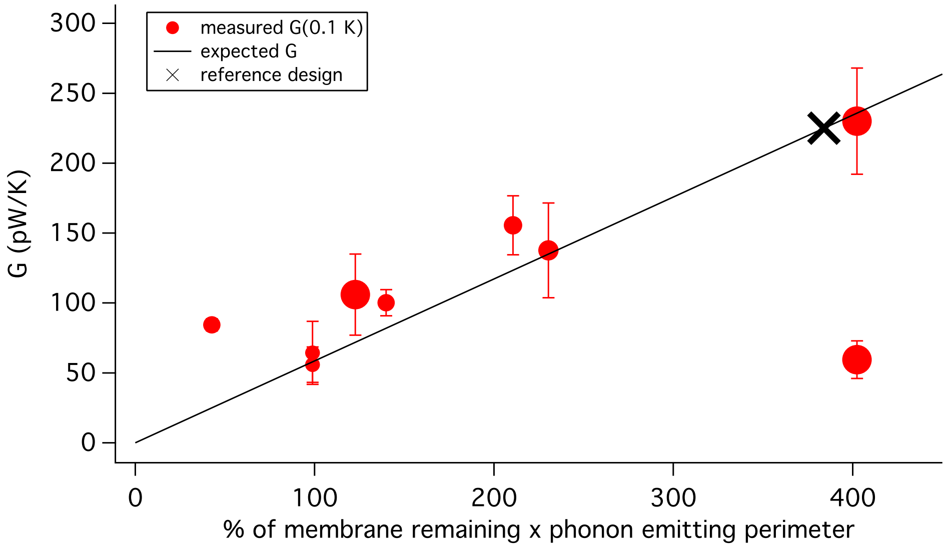

Figure 9.8: Thermal conductivity scales with the product of the perforation percentage and phonon emitting perimeter. Measured conductivities are given by red points. Point size is scaled based on the amount of phonon emitting perimeter. The scaling relation is illustrated by a black line, and the reference design used for scaling is marked with a black X.

Another common feature of all the devices tested was evidence for excess heat capacity on the order of 40-50% more than calculations would suggest. This heat capacity does not appear to be a single lumped element, rather most of the pixels appear to have more than one decay time constant, indicating that the excess heat capacity is “hanging” and couples to the device via an unknown additional thermal conductivity. The presence of excess heat capacity is a major concern, since energy resolution scales as $\sqrt{C}$. It is unlikely that this heat capacity is associated with the TES, as the TES is expected to contribute less than 5% of the total heat capacity of the largest pixels we tested.

Pixel	% membrane	perim. (μm)	G (predicted)	G (measured)
MXW1dL1c1	8.2	1706	82	100.2 ± 9.2
MXW1dL2c2	2.5	1706	25	84.4 ± 4.3
MXW1jL1c2	10.1	978	58	55.9 ± 12.6
MXW1jL1c3	10.1	978	58	64.3 ± 22.6
MXW1Dc55	8.2	4907	236	59.5 ± 13.5
MXW1Dc63	9.4	2450	134	137.7 ± 33.9
MXW1Dc65	10.8	1950	123	155.4 ± 21.1
MXW2c62m1	8.2	4907	236	230 ± 38
MXW2c67m2	2.5	4907	77	106 ± 29

Table 9.2: Summary of detector-bath thermal conductivity measurements. The column "% membrane" indicates the percentage of the membrane perimeter that is left intact after perforation. The scaling parameter is the product of the percentage of remaining membrane multiplied by the total phonon emitting perimeter (column "perim."), including the TES and the absorber support stems (or the perimeter of the absorber, in the case of the coplanar designs). The measured conductivity of a reference design (a device developed for the Micro-X mission) is then used to predict G(0.1 K) for the new designs, given in the column "G (predicted)" in units of pW/K. Finally, the measured conductivity at 0.1 K is given, also in units of pW/K.

One possible culprit is the nitride membrane. This speculation has some precedent, as groups have reported large excess heat capacities associated with thin nitride membranes in the past (for example, Goldie et al. (2009) and Kinnunen et al. (2012)). If this proves to be the case, the only possible way to reduce this heat capacity is to reduce the volume of the membrane. In the case of the coplanar designs, it is only possible to thin the membrane. This may prove difficult, since these devices are already susceptible to breaking when the membrane is stressed. For suspended designs, it may be possible to isolate small areas immediately surrounding the support stems and TES, thereby reducing the surface area of the membrane. Another possible source of excess heat capacity is the gold absorber. GSFC has seen excess heat capacity in gold devices in the past, which they were able to identify as magnetic contamination introduced during an ion mill. If this is the source of the excess, then it should be possible to identify the processing step where it is introduced and eliminate it. Further steps can be taken to identify the the excess. Modeling that includes a hanging heat capacity could determine the nature of the thermal conductance that couples the excess heat capacity to the device and may provide clues as to its origin. And measurements of the heat capacity of the nitride membrane would reveal whether or not this is a viable explanation.

9.3 Conclusions

Despite the open questions, we have learned a great deal about these devices and the goal of 2 eV energy resolution seems within reach. Our investigation has shown that between the suspended and coplanar absorber designs, the suspended absorber is clearly more desirable. The results from the 890 μm pixels tested in MXW1d showed high lateral thermal conductivity, suggesting that position dependent pulse shape would not degrade the resolution at X-ray energies below 1.5 keV. Being able to make the conductivity to the bath very small simplifies the analysis: there is no need to correct for rise time/pulse height dependence, or to throw away signal to noise ratio by using a low pass filter. The absorber shields the TES, so the number of direct absorption events is small. And, having the suspended absorber increases the focal plane filling factor, allowing the full array to be smaller and reduces thermal crosstalk from events that are absorbed in the silicon frame.

However, it is clear that yielding the 200 nm thick suspended absorbers will be a major fabrication challenge. In the event that we are unable to make them, the coplanar design has proven to be a viable option. We can now yield the coplanar pixels with a high success rate, thanks to the reduction of the titanium sticking layer to a grid of small dots, and rounded the slots that perforate the nitride membrane. Position dependent pulse shape in these devices is a problem, thanks to the large phonon emitting perimeter of the absorber that lies directly on the membrane. It is therefore desirable to have a very low conductivity to the bath. However, the extremely perforated membranes still break at a fairly high rate. So, we will need to find a compromise between structural integrity and low bath conductivity. It seems likely that we can meet somewhere in the middle of the 90% perforated design and the long slot design (which is effectively 97.5% perforated) where the pixels will survive but we can still improve the resolution.

Finally, we still have work to do on understanding how to make a better TES. In particular, we've seen device to device and chip to chip variation on MXW1 and MXW2 that we don't fully understand. Most devices seemed to have α on the order of 50-60. However, one chip (MXW1j) seemed to have come out even lower, for reasons that have yet to be understood. On the other hand, chip MXW1d, with 890 μm × 890 μm suspended absorbers, appeared to have larger α, on the order of 80-100. This enabled us to achieve 6 eV energy resolution despite finding that the pixels had 60-70% excess heat capacity. These devices had 500 nm thick absorbers and $T_c \approx 105$ mK. If we can replicate the sensitivity of these devices with 200 nm thick absorbers at $T_c = 70$ mK, we would expect 2.2 eV resolution.

Ultimately, we need to build a 256 pixel, 2 cm^2, 2 eV array. The first step is to continue to push the resolution down. This means yet thinner absorbers (remember that MXW2 absorbers were 300 nm, and we can go to 200 nm before the efficiency begins to suffer). Process development to yield the thin suspended absorbers is ongoing, and will determine whether we need to use the coplanar design. In the meantime, more work can be done to understand the sources of excess heat capacity, and to improve the analysis techniques for correcting for position dependent pulse shape in the coplanar absorbers. And finally, better understanding of variation in sensitivity observed between the MXW designs will help us make the jump to 2 eV.

Appendix A

Modeling for MXW wafer

A.1 Input parameters for μCal models

The following tables list the input parameters for the μCal model for an all-gold suspended absorber that is 890 μm × 890 μm × 0.2 μm, as described in Chapter 4. One T-stem thermally connects the absorber and TES, and 24 additional round absorber support stems (20 μm diameter) sit on the membrane and provide additional mechanical support to the absorber. Their effect is included in the model insofar as they affect the total detector-to-bath thermal conductivity. The membrane is 91.7% perforated. The TES is a 140 μm × 140 μm bilayer with 40 nm Mo/250 nm Au. Note that according to BCS theory, the TES may have up to 2.43 times higher heat capacity at T_c. Since the TES operates at a slightly higher temperature than T_c, the heat capacity is likely to be between 1-2.43 times the normal heat capacity. Since the TES heat capacity is small compared to the absorber, this effect is small and has been neglected in this calculation. For each parameter, the table gives the μCal name of each parameter, the value used in simulation, and a description of the parameter (from the "parwave_help" wave in μCal).

Non-Linear Parameters

μCal name	Value	Description
C01_a [J/K]	1.1e-12	Absorber heat capacity at 100 mK
C01_e [J/K]	5.08e-14	Electron heat capacity at 100 mK
C01_p [J/K]	1e-15	Phonon heat capacity at 100 mK
gamma_a	1	C_a = C01_a*(T/0.1)**gamma_a
gamma_e	1	C_e = C01_e*(T/0.1)**gamma_e
gamma_p;	0	C_p = C01_p*(T/0.1)**gamma_p
Gae01 [W/K]	1e-06	Absorber-Electron thermal conductance
Gap01 [W/K]	0	Absorber-Phonon thermal conductance
Gep01 [W/K]	1e-08	Electron-Phonon thermal conductance
Gpb01 [W/K]	110e-12	Phonon-Bath thermal conductance
Bae	1	Pae=(Gae01/(0.1**Bae*(Bae+1))*(Ta**(Bae+1)-Te**(Bae+1))
Bap	3	Pap=(Gap01/(0.1**Bap*(Bap+1))*(Ta**(Bap+1)-Tp**(Bap+1))
Bep	3	Pep=(Gep01/(0.1**Bep*(Bep+1))*(Te**(Bep+1)-Tp**(Bep+1))
Bpb;	2.5	Ppb=(Gpb01/(0.1**Bpb*(Bpb+1))*(Tp**(Bpb+1)-Tb**(Bpb+1))
Tb [K]	0.05	Base temperature of refrigerator

Table A.1: μCal model non-linear parameters

Circuit Parameters

μCal name	Value	Description
R [Ohm]		TES resistance R(T,I)=Rp+Ro+alpha0*Ro/Tc*(T-Tc)+beta_i*Ro/Io*(I-Io)
Rn [Ohm]	0.008	Normal Resistance (Rn)
R/Rn [%];	15	Operating point for detector (% Rn)
Rp [Ohm];	1e-06	Parasitic resistance inside TES (for parasitics outside tes add to shunt resistor value)
Tc [K]	0.07	Critical Temperature (transition temperature)
alpha0	55	Alpha in the middle of the transition
Ce/C_betai [n/a]	1.25	Beta_i (current sensitivity)

Table A.2: μCal model circuit parameters

Common Parameters

μCal name	Value	Description
RL [Ohm];	0.00025	Load (Shunt) Resistor + parasitic outside TES
L [H]	2e-08	Inductance
Lp [H]	1e-09	Parasitic Inductance on Load (Shunt) resistor side
Ccap [F]	5e-12	Electrical Capacitance
PhononNoise_type	1	0 = diffusive link, 1 = specular link
ampnoise [AorV/rtHz]	10e-12	Non-filtered noise, used for squid or electronics noise.
excess_J noise	1.58	Excess Johnson noise will be Johnson noise level times this number
excess_P noise	0.8	Excess Phonon noise will be Phonon noise level times this number
1/f noise [AorV/rtHz];	0	1/f noise value at 1 Hz

Table A.3: μCal model common parameters

A.2 MXW Wafer designs and modeling

Table A.4 lists predicted C, G, τ_{eff}, and ΔE for the MXW1 detector designs. The decay time and energy resolution are calculated using the μCal model, using the parameters given in Section A.1 and varying the TES-to-bath thermal conductivity and the absorber heat capacity (G and C in Table A.4, respectively) according to the pixel geometry. The heat capacity is calculated from literature values. The thermal conductivity is assumed to depend on the product of the phonon emitting perimeter and the percentage of un-etched membrane perimeter (see Section 4.2). This is scaled relative to a reference design from Micro-X, which had $G(0.1K) = 225$ pW/K for a 84% perforated membrane with 2400 μm of phonon emitting perimeter, including the TES plus all absorber support stems. For all designs, it is assumed that $\alpha = 55$ and $\beta = 1.25$.

All absorbers are assumed to be 200 nm thick. “Absorb.” refers to the size of a side of the absorber. For the suspended designs, the absorber is square in all cases. For the coplanar designs, the absorber is square, but has an area of approximately 150 μm × 150 μm removed to accommodate the TES. “Perf.” refers the the percentage of the perimeter of the membrane that is etched through (“perforated”). “Perim.” is the total phonon emitting perimeter in μm. For the suspended designs, this includes the TES and absorber support stems. For coplanar designs, this includes the TES and the perimeter of the absorber. The absorber support stems and the membrane perforations determine the thermal conductivity (G) between the detector and the bath. The G given below is the thermal conductivity at 100 mK. Likewise, the heat capacity is C(100 mK), and is given for the absorber only. The μCal modeling package is used to compute the expected decay time and energy resolution. The decay time (τ_{eff}) includes the effect of electrothermal feedback.

Absorb. (μm)	Perf.	Perim. (μm)	stem pattern	G (pW/K)	C (pJ/K)	τ_{eff} (ms)	ΔE (eV)
240	89.9%	894	3 sq, 1 Tt	53	0.088	1.17	0.74
240	89.9%	978	6 sq, 1 Tt	58	0.088	1.07	0.74
240	92.1	978	6 sq, 1 Tt	45	0.088	1.37	0.74
350	89.2%	1950	coplanar	123	0.14	0.67	0.85
350	94.6%	1950	coplanar	62	0.14	1.33	0.86
440	89.2%	1482	24 sq, 1 Tt	94	0.272	1.41	1.09
440	94.6%	1482	24 sq, 1 Tt	47	0.272	2.81	1.10
440	89.2%	2540	5 sq, 3 T, 1 Tt	160	0.272	1.66	1.09
440	94.6%	2540	5 sq, 3 T, 1 Tt	80	0.272	0.835	1.08
480	84%	2450	coplanar	230	0.293	0.62	1.11
480	90.6%	2450	coplanar	134	0.293	1.05	1.11
480	95.8%	2450	coplanar	60	0.293	2.34	1.13
590	90.6%	2042	44 sq, 1 Tt	112	0.49	1.93	1.39
590	95.8%	2042	44 sq, 1 Tt	50	0.49	4.30	1.41
590	84%	2317	24 circ, 1 Tt	217	0.49	1.01	1.37
590	90.6%	2317	24 circ, 1 Tt	127	0.49	1.71	1.39
590	95.8%	2317	24 circ, 1 Tt	56	0.49	3.84	1.41
590	90.6%	1500	11 circ, 1 Tt	82	0.49	2.63	1.40
590	95.8%	1500	11 circ, 1 Tt	37	0.49	5.81	1.43
590	84%	2960	3 T, 1 Tt, 1x	278	0.49	0.79	1.36
590	90.6%	2960	3 T, 1 Tt, 1x	162	0.49	1.34	1.38
590	95.8%	2960	3 T, 1 Tt, 1x	72	0.49	3.00	1.40
765	91.7%	4907	coplanar	236	0.764	0.95	1.68
765	97.5%	4907	coplanar	73	0.764	2.98	1.71
825	92.3%	5230	coplanar	251	0.896	1.03	1.81
825	97.7%	5230	coplanar	77	0.896	3.24	1.84
890	91.7%	2317	24 circ, 1 Tt	111	1.10	2.75	2.01
890	91.7%	1706	32 sq, 1 Tt	82	1.10	5.48	2.06
890	97.5%	1706	32 sq, 1 Tt	25	1.10	12.1	2.16
890	91.7%	3218	86 sq, 1 Tt	155	1.10	2.92	2.02

Table A.4: Predicted C, G, τ_{eff}, and ΔE for MXW1 designs. The decay time and energy resolution are calculated using the μCal model, using the parameters given in Section A.1, except $G_{tes-bath}$ and C_{abs}, which are varied according to the values reported above. Abbreviations for support stems: “Tt” refers to a T-stem that overlaps the TES, “T” is a T-stem that lies entirely on the membrane, “x” is a plus shaped stem on the membrane, “sq” is a 7 μm square post on the membrane, and “circ” is a 20 μm diameter circular post on the membrane.

References

Ambegaokar, V., & Halperin, B. I. 1969, Physical Review Letters, 22, 1364

Andrews, D. H., Jr, W. F. B., Ziegler, W. T., & Blanchard, E. R. 1942, Review of Scientific Instruments, 13, 281

Arnaud, K. A. 1996, in Astronomical Data Analysis Software and Systems V, Vol. 101, 17

Aslamazov, L. G., & Larkin, A. I. 1968, Soviet Physics - Solid State, 10, 1104, iNSPEC:1968B20494

Bandler, S. R., Brekosky, R. P., Brown, A.-D., et al. 2008, Journal of Low Temperature Physics, 151, 400

Bandler, S. R., Adams, J. S., Bailey, C. N., et al. 2013, IEEE Transactions on Applied Superconductivity, 23, 2100705

Bautz, M. W., Kissel, S. E., Prigozhin, G. Y., et al. 2004, in , 111–122

Bellm, E. C., & Vaillancourt, J. E. 2005, The Astrophysical Journal, 622, 959

Bennett, D. A., Swetz, D. S., Horansky, R. D., Schmidt, D. R., & Ullom, J. N. 2012, Journal of Low Temperature Physics, 167, 102

Bennett, D. A., Swetz, D. S., Schmidt, D. R., & Ullom, J. N. 2013, Physical Review B, 87, 020508

Bowyer, C. S., Field, G. B., & Mack, J. E. 1968, Nature, 217, 32

Boyle, W. S., & Rodgers, K. F., J. 1959, Journal of the Optical Society of America, 49, 66

Brandt, W. N., Alexander, D. M., Hornschemeier, A. E., et al. 2001, The Astronomical Journal, 122, 2810

Brown, A.-D., Bandler, S. R., Brekosky, R., et al. 2008, Journal of Low Temperature Physics, 151, 413

Bunner, A. N., Coleman, P. L., Kraushaar, W. L., & McCammon, D. 1971, The Astrophysical Journal Letters, 167, L3

Burrows, D. N., & Mendenhall, J. A. 1991, Nature, 351, 629

Buzdin, A. I. 2005, Reviews of Modern Physics, 77, 935

Canizares, C. R., Davis, J. E., Dewey, D., et al. 2005, Publications of the Astronomical Society of the Pacific, 117, 1144, arXiv: astro-ph/0507035

Chen, T. C., Finkbeiner, F. M., Bier, A., & DiCamillo, B. 1999, Superconductor Science & Technology, 12, 840, wOS:000083948400044

Cochran, J. F., & Mapother, D. E. 1958, Physical Review, 111, 132, iNSPEC:1958A05928

Cowie, L. L., Garmire, G. P., Bautz, M. W., et al. 2002, The Astrophysical Journal Letters, 566, L5

Cox, D. P. 1998, in Lecture Notes in Physics, Vol. 506, IAU Colloq. 166: The Local Bubble and Beyond (Springer-Verlag), 121–131

Cravens, T. E. 1997, Geophysical Research Letters, 24, 105

Cravens, T. E., Robertson, I. P., & Snowden, S. L. 2001, Journal of Geophysical Research, 106, 24883

Dennerl, K. 2010, Space Science Reviews, 157, 57

Dorman, B., & Arnaud, K. A. 2001, in , 415

Eckart, M., Adams, J., Bandler, S., et al. 2013, IEEE Transactions on Applied Superconductivity, 23, 2101705

Eckart, M. E., Adams, J. S., Bandler, S. R., et al. 2009, in Low Temperature Detectors Ltd 13, ed. B. Cabrera, A. Miller, & B. Young, Vol. 1185 (Melville: Amer Inst Physics), 699–702, wOS:000281588500156

Fano, U. 1947, Physical Review, 72, 26

Figueroa-Feliciano, E. 2001, PhD thesis

Figueroa-Feliciano, E., Saab, T., Rivera-Ortiz, P. M., et al. 2008, Journal of Low Temperature Physics, 151, 424, wOS:000253697900069

Finkbeiner, F. M., Chen, T. C., Aslam, S., et al. 1999, Ieee Transactions on Applied Superconductivity, 9, 2940, wOS:000081964500026

Fraser, G. 2004, Nuclear Instruments and Methods in Physics Research Section A: Accelerators, Spectrometers, Detectors and Associated Equipment, 523, 234

Galeazzi, M. 2011, Ieee Transactions on Applied Superconductivity, 21, 267, wOS:000291050500040

Galeazzi, M., Bogorin, D., & Chen, C. 2006, Nuclear Instruments and Methods in Physics Research Section A: Accelerators, Spectrometers, Detectors and Associated Equipment, 559, 453

Galeazzi, M., & McCammon, D. 2003, Journal of Applied Physics, 93, 4856

Galeazzi, M., Chiao, M., Collier, M. R., et al. 2014, Nature, 512, 171

Garmire, G. P., Bautz, M. W., Ford, P. G., Nousek, J. A., & Ricker, Jr., G. R. 2003, 28–44

Giacconi, R., Gursky, H., Paolini, F. R., & Rossi, B. B. 1962, Physical Review Letters, 9, 439

Gildemeister, J. M., Lee, A. T., & Richards, P. L. 1999, Applied Physics Letters, 74, 868

Goldie, D. J., Audley, M. D., Glowacka, D. M., Tsaneva, V. N., & Withington, S. 2009, Journal of Applied Physics, 105, 074512, wOS:000266633500098

Gould, R. J., & Burbidge, G. R. 1963, The Astrophysical Journal, 138, 969

Hatakeyama, S., Ohno, M., Damayanthi, R. M. T., et al. 2013, Ieee Transactions on Applied Superconductivity, 23, 2100804, wOS:000318867100046

Hein, R. A., Gibson, J. W., Matthias, B. T., Geballe, T. H., & Conrenzwit, E. 1962, Physical Review Letters, 8, 408, iNSPEC:1962A17727

Henke, B. L., Gullikson, E. M., & Davis, J. C. 1993, Atomic Data and Nuclear Data Tables, 54, 181

Hickox, R. C., & Markevitch, M. 2006, The Astrophysical Journal, 645, 95

Hoevers, H. F. C. 2006, Nuclear Instruments & Methods in Physics Research Section a-Accelerators Spectrometers Detectors and Associated Equipment, 559, 702, wOS:000236974700118

Hoevers, H. F. C., Bento, A. C., Bruijn, M. P., et al. 2000a, Nuclear Instruments & Methods in Physics Research Section a-Accelerators Spectrometers Detectors and Associated Equipment, 444, 192, wOS:000086823400043

—. 2000b, Applied Physics Letters, 77, 4422

Holmes, W., Gildemeister, J. M., Richards, P. L., & Kotsubo, V. 1998, Applied Physics Letters, 72, 2250

Horansky, R. D., Beall, J. A., Irwin, K. D., & Ullom, J. N. 2009, in Low Temperature Detectors Ltd 13, ed. B. Cabrera, A. Miller, & B. Young, Vol. 1185 (Melville: Amer Inst Physics), 733–736, wOS:000281588500163

Horansky, R. D., Ullom, J. N., Beall, J. A., et al. 2007, Nuclear Instruments and Methods in Physics Research Section A: Accelerators, Spectrometers, Detectors and Associated Equipment, 579, 169

Irwin, K. D. 2006, Nuclear Instruments & Methods in Physics Research Section a-Accelerators Spectrometers Detectors and Associated Equipment, 559, 718, wOS:000236974700123

Irwin, K. D., & Hilton, G. C. 2005, in Cryogenic particle detection (Berlin: Springer)

Irwin, K. D., Hilton, G. C., Martinis, J. M., & Cabrera, B. 1996, Nuclear Instruments & Methods in Physics Research Section a-Accelerators Spectrometers Detectors and Associated Equipment, 370, 177, wOS:A1996UA32400059

Irwin, K. D., Hilton, G. C., Wollman, D. A., & Martinis, J. M. 1998, Journal of Applied Physics, 83, 3978

Ishisaki, Y., Morita, U., Koga, T., et al. 2004, Nuclear Instruments and Methods in Physics Research Section A: Accelerators, Spectrometers, Detectors and Associated Equipment, 520, 452

Jahoda, K., & Mccammon, D. 1988, Nuclear Instruments & Methods in Physics Research Section a-Accelerators Spectrometers Detectors and Associated Equipment, 272, 800, wOS:A1988Q774000022

Janesick, J., Elliott, T., Bredthauer, R., Chandler, C., & Burke, B. 1988, in , 70–95

Jethava, N., Ullom, J. N., Irwin, K. D., et al. 2009, in Low Temperature Detectors Ltd 13, ed. B. Cabrera, A. Miller, & B. Young, Vol. 1185 (Melville: Amer Inst Physics), 31–33, wOS:000281588500005

Kinnunen, K. M., Nuottajarvi, A. K., & Maasilta, I. J. 2008, Journal of Low Temperature Physics, 151, 144, wOS:000253697900021

Kinnunen, K. M., Palosaari, M. R. J., & Maasilta, I. J. 2012, Journal of Applied Physics, 112, 034515, wOS:000308335400133

Kittel, C. 1996, Introduction to solid state physics, 7th edn. (New York: Wiley)

Knoedler, C. M. 1983, Journal of Applied Physics, 54, 2773

Koutroumpa, D., Lallement, R., Raymond, J. C., & Kharchenko, V. 2009, The Astrophysical Journal, 696, 1517

Kozorezov, A., Golubov, A., Martin, D., et al. 2011, Applied Physics Letters, 99, 063503

Kozorezov, A., Golubov, A. A., Martin, D. D. E., et al. 2012, Journal of Low Temperature Physics, 167, 108, wOS:000302093500004

Kraushaar, W., Clark, G. W., Garmire, G., et al. 1965, The Astrophysical Journal, 141, 845

Leivo, M., & Pekola, J. 1998, Applied Physics Letters, 72, 1305

Lindeman, M., Anderson, M., Bandler, S., et al. 2006, Nuclear Instruments and Methods in Physics Research Section A: Accelerators, Spectrometers, Detectors and Associated Equipment, 559, 715

Lindeman, M. A., Barger, K. A., Brandl, D. E., et al. 2008, Journal of Low Temperature Physics, 151, 190

Lindeman, M. A., Brekosky, R. P., Figueroa-Feliciano, E., et al. 2002, in Low Temperature Detectors, ed. F. S. Porter, D. McCammon, M. Galeazzi, & C. K. Stahle, Vol. 605 (Melville: Amer Inst Physics), 203–206, wOS:000176260300047

Lindeman, M. A., Bandler, S., Brekosky, R. P., et al. 2004, Nuclear Instruments and Methods in Physics Research Section A: Accelerators, Spectrometers, Detectors and Associated Equipment, 520, 411

Lisse, C. M., Dennerl, K., Englhauser, J., et al. 1996, Science, 274, 205

Luukanen, A., Kinnunen, K. M., Nuottajarvi, A. K., et al. 2003, Physical Review Letters, 90, 238306, wOS:000183483500058

Maasilta, I. J. 2012, Aip Advances, 2, 042110, wOS:000312828700023

Marshall, F. J., & Clark, G. W. 1984, The Astrophysical Journal, 287, 633

Martinis, J. M., Hilton, G. C., Irwin, K. D., & Wollman, D. A. 2000, Nuclear Instruments & Methods in Physics Research Section a-Accelerators Spectrometers Detectors and Associated Equipment, 444, 23, wOS:000086823400007

Mather, J. C. 1982, Applied Optics, 21, 1125

Matthias, B. T., Geballe, T. H., & Compton, V. B. 1963, Reviews of Modern Physics, 35, 1, iNSPEC:1963A14438

Mauskopf, P. D., Bock, J. J., Del Castillo, H., Holzapfel, W. L., & Lange, A. E. 1997, Applied Optics, 36, 765

McCammon, D. 2005, in Cryogenic particle detection (Berlin: Springer)

McCammon, D., Bunner, A. N., Coleman, P. L., & Kraushaar, W. L. 1971, The Astrophysical Journal Letters, 168, L33

McCammon, D., Burrows, D. N., Sanders, W. T., & Kraushaar, W. L. 1983, The Astrophysical Journal, 269, 107

McCammon, D., Almy, R., Apodaca, E., et al. 2002, Astrophysical Journal, 576, 188, wOS:000177589100018

Mendenhall, J. A., Burrows, D. N., Cawley, L. J., et al. 1996, in , 34–47

Metzger, A. E. 1964, Nature, 204, 766

Moseley, S. H., Mather, J. C., & McCammon, D. 1984, Journal of Applied Physics, 56, 1257

Nagaev, K. 1991, Physica C, 184, 149, wOS:A1991GX03100020

Nagel, U., Nowak, A., Gebauer, H., et al. 1994, Journal of Applied Physics, 76, 4262, wOS:A1994PK45800045

Robertson, I. P., Cravens, T. E., Snowden, S., & Linde, T. 2001, Space Science Reviews, 97, 401

Rothenflug, R., Rocchia, R., & Koch, L. 1965, International Cosmic Ray Conference, 1, 446

Saab, T., Figueroa-Feliciano, E., Iyomoto, N., et al. 2007, Journal of Applied Physics, 102, 104502

Sadleir, J. E., Smith, S. J., Bandler, S. R., Chervenak, J. A., & Clem, J. R. 2010, Physical Review Letters, 104, 047003, wOS:000274336600045

Sadleir, J. E., Smith, S. J., Robinson, I. K., et al. 2011, Physical Review B, 84, 184502, wOS:000296861800005

Sadleir, J. E., Bandler, S. R., Brekosky, R. P., et al. 2006, Nuclear Instruments & Methods in Physics Research Section a-Accelerators Spectrometers Detectors and Associated Equipment, 559, 447, wOS:000236974700037

Sanders, W. T., Edgar, R. J., Kraushaar, W. L., McCammon, D., & Morgenthaler, J. P. 2001, The Astrophysical Journal, 554, 694

Sanders, W. T., Kraushaar, W. L., Nousek, J. A., & Fried, P. M. 1977, The Astrophysical Journal Letters, 217, L87

Seidel, G. M., & Beloborodov, I. S. 2004, Nuclear Instruments & Methods in Physics Research Section a-Accelerators Spectrometers Detectors and Associated Equipment, 520, 325, wOS:000220606900086

Skocpol, W. J., Beasley, M. R., & Tinkham, M. 1974, Journal of Low Temperature Physics, 16, 145

Smith, S. J., Bandler, S. R., Brown, A.-D., et al. 2008, Journal of Low Temperature Physics, 151, 195, wOS:000253697900030

Smith, S. J., Adams, J. S., Bailey, C. N., et al. 2013, Journal of Applied Physics, 114, 074513, wOS:000323510900083

Smith, S. J., Adams, J. S., Bandler, S. R., et al. 2014, Journal of Low Temperature Physics, 176, 356, wOS:000338210800036

Snowden, S. L., Egger, R., Finkbeiner, D. P., Freyberg, M. J., & Plucinsky, P. P. 1998, The Astrophysical Journal, 493, 715

Snowden, S. L., McCammon, D., Burrows, D. N., & Mendenhall, J. A. 1994, The Astrophysical Journal, 424, 714

Snowden, S. L., McCammon, D., & Verter, F. 1993, The Astrophysical Journal Letters, 409, L21

Snowden, S. L., Mebold, U., Hirth, W., Herbstmeier, U., & Schmitt, J. H. M. 1991, Science, 252, 1529

Snowden, S. L., Egger, R., Freyberg, M. J., et al. 1997, The Astrophysical Journal, 485, 125

Spitzer, Jr., L. 1956, The Astrophysical Journal, 124, 20

Staguhn, J. G., Moseley, S. H., Benford, B. J., et al. 2004, Nuclear Instruments & Methods in Physics Research Section a-Accelerators Spectrometers Detectors and Associated Equipment, 520, 336, wOS:000220606900089

Stahle, C. K., Lindeman, M. A., Figueroa-Feliciano, E., et al. 2002, AIP Conference Proceedings, 223, iNSPEC:7295240

Szymkowiak, A. E., Kelley, R. L., Moseley, S. H., & Stahle, C. K. 1993, Journal of Low Temperature Physics, 93, 281

Tanaka, Y., & Bleeker, J. A. M. 1977, Space Science Reviews, 20, 815

Tiest, W. M. B., Hoevers, H. F. C., Mels, W. A., et al. 2002, in Low Temperature Detectors, ed. F. S. Porter, D. McCammon, M. Galeazzi, & C. K. Stahle, Vol. 605 (Melville: Amer Inst Physics), 199–202, wOS:000176260300046

Ullom, J. N., Doriese, W. B., Hilton, G. C., et al. 2004, Applied Physics Letters, 84, 4206, wOS:000221404700023

Usadel, K. 1970, Physical Review Letters, 25, 507, wOS:A1970H065400006

Vaillancourt, J. E., Allen, C. A., Brekosky, R., et al. 2004, Nuclear Instruments & Methods in Physics Research Section a-Accelerators Spectrometers Detectors and Associated Equipment, 520, 212, wOS:000220606900055

Voss, R., Knoedler, C., & Horn, P. 1980, Physical Review Letters, 45, 1523, wOS:A1980KN33000017

Wikus, P., Doriese, W. B., Eckart, M. E., et al. 2009, in AIP Conference Proceedings, Vol. 1185 (AIP Publishing), 434–437

Yoshino, T., Yoshida, K., Hagihara, T., et al. 2006, Nuclear Instruments & Methods in Physics Research Section a-Accelerators Spectrometers Detectors and Associated Equipment, 559, 432, wOS:000236974700033